MBE-grown wide bandgap II-VI materials for novel devices based on intersubband transitions

By

Hong Lu

A dissertation submitted to the Graduate Faculty in Chemistry in partial fulfillment of the requirements for the degree of Doctor of Philosophy, The City University of New York

2007

ProQuest Information and Learning Company
300 North Zeeb Road
P.O. Box 1346
Ann Arbor, MI 48106-1346

Approval Page

This manuscript has been read and accepted for the Graduate Faculty in Chemistry in satisfaction of the dissertation requirement for the degree of Doctor of Philosophy.

Jan. 2007	Maria C. Tamargo
----------	----------
Date	Dr. Maria C. Tamargo
	Chair of Examining Committee
Jan. 2007	Gerald Koeppl
----------	----------
Date	Dr. Gerald Koeppl
	Executive Officer

Dr. Maria C. Tamargo

Dr. Harry Gafney

Dr. John Lombardi

Supervisory Committee

THE CITY UNIVERSITY OF NEW YORK

Abstract

MBE-grown wide bandgap II-VI materials for novel devices based on intersubband transitions

By: Hong Lu

Mentor: Maria C. Tamargo

Molecular Beam Epitaxy (MBE) is a versatile thin film growth technique with the ability to control the growth with atomic layer accuracy. Novel devices with complex structures can be prepared by MBE to meet specific needs. Intersubband (ISB) devices, such as quantum cascade lasers (QCLs) and quantum well infrared photodetectors (QWIPs) operating in the mid-infrared range, have potential advantages over conventional interband devices due to the increased ability to engineer the devices, as well as their intrinsic faster relaxation time and higher quantum efficiencies.

The shortest wavelength that can be obtained is limited by the band offset in the conduction band of the heterostructures currently used for these devices. Semiconductors of the II-VI family have shown potential in fabricating this kind of devices due to their widely adjustable bandgaps. In particular, the $Zn_xCd_{1-x}Se/Zn_{x'}Cd_{y'}Mg_{1-x'-y'}Se$ QW structure is a II-VI semiconductor system recently investigated in our lab, whose emission can cover the entire visible wavelength range by simply changing the QW width. A modulation technique, contactless

electroreflectance (CER), has been used to determine the conduction band offset (CBO) of the system. For the limit composition of this lattice-matched system, $Zn_{0.5}Cd_{0.5}Se/Zn_{0.13}Mg_{0.87}Se$, the CBO has been estimated to be as large as 1.12 eV.

In this work, the growth of these materials is optimized, and methods to study the ISB transitions in the material system, including theoretical prediction by the envelope function approximation, CBO determination and ISB transition energy estimation by CER, and ISB absorption measurement by Fourier transform infrared (FTIR) spectroscopy, are investigated systematically. A series of high quality $Zn_xCd_{1-x}Se/Zn_{x'}Cd_{y'}Mg_{1-x'-y'}Se$ single QW and multiple QW structures with different QW thicknesses and composition (and thus, strain) have been grown on InP substrates by MBE. The samples were characterized by X-ray diffraction (XRD), Photoluminescence (PL), time-resolved PL, CER and FTIR measurements, etc. All the data indicate excellent material properties which meet the requirements of device design and demonstrated the potential of this II-VI material system for ISB device applications.

To my family

Acknowledgments

This thesis would have never been completed without the guidance of my mentor Professor Maria C. Tamargo. Her continuous encouragement and inspiration along with instructive scientific discussions have allowed me to explore both the research field and my abilities. I would like to thank her for the opportunities she gave me to train myself how to work on a project independently and collaboratively. If I want to say something to her, I will say “You are a great mentor, thank you very much.”

During my Ph. D studies, I have been working with a lot of wonderful people. I am especially indebted to Professor Aidong Shen, Professor Martin Muñoz and Dr. Shengkun Zhang, my friends and my teachers, from whom I have learned many experimental skills on the growth and characterization of semiconductor materials and gained a lot of knowledge from their valuable comments, constant support and the discussions I had with them.

Thanks to Professor Tamargo again for gathering together an exceptionally bright and talented group of students and researchers who have helped me in countless ways and who made my experience in the group unforgettable. I would like to thank all the current and former group members who I have interacted with: Dr. M. Noemi Perez-Paz, Dr. Mohammad Sohel, Dr. Xuecong Zhou, William Charles, Ikue Yokomizo, Qiang Zhang, Dr. Francisco Fernandez, Dr. Oleg Maksimov and Dr. Shiping Guo, for their support, inspiration, helpful discussion as well as their friendship.

Many thanks to Professor John R. Lombardi, Professor Harry D. Gafney for kindly serving on my thesis committee. Thanks are also due to, Dr. H. C. Liu and Dr. C. Y. Song at NRC Canada, Professor Claire Gmachl at Princeton University for performing some of the experimental studies and for valuable discussions; Yinyan Gong at Columbia University for obtaining the HRXRD data at Brookhaven National Lab; Dr. Jorge Morales at City College for help with the SEM images, and John Machintoch and Dr. Kalid Eid in the Nanofabrication Lab at Pennsylvania State University for helping me with the device fabrication and performance studies. A lot of kind advice and helpful discussions from Professor Glen Kowach, Professor David Crouse, and Professor Vinod Menon are also greatly appreciated. Many thanks also to the friends I have in City College, especially Li Zhang for her assistance in finishing my thesis.

The financial support from the Ph. D program of Chemistry, and the Graduate Student Research Grant from CUNY are gratefully acknowledged. Support from Professor R. R. Alfano and the NASA Center for Optical Sensing and Imaging is also recognized.

I would like to thank, expressly, my parents who have taught me the principles I should embrace in my life: love of family, hard work, and integrity.

Finally, my deepest appreciation is for my husband Zelin without his love, understanding and support during these years, nothing would have been possible.

Table of contents

List of Tables

Chapter 4

Chapter 5

Chapter 6

Chapter 7

List of illustrations

Chapter 1

Chapter 2

Chapter 3

Chapter 4

Chapter 5

Chapter 6

Chapter 7

Chapter 8

Chapter 1

Introduction

Devices based on intersubband (ISB) transitions, such as quantum cascade lasers (QCLs) and quantum-well infrared photodetectors (QWIPs), are being extensively studied due largely to their potential applications.[1] Band structure engineering has made it possible to achieve ISB devices operating over a wide spectrum range without the need to change the material system. Advanced crystal growth techniques, such as molecular beam epitaxy (MBE), have made this kind of devices, usually based on complex multi-layer structures, possible due to the accurate control (atomic layer or mono-layer) of the growth.

In this work, we explored the potential of using a wide bandgap II-VI material system, $Zn_xCd_{1-x}Se/Zn_{x'}Cd_{y'}Mg_{1-x'-y'}Se$, which has a large CBO with a type-I band alignment and can be grown lattice-matched on InP substrates, to realize shorter wavelength ISB devices operating at RT. The Riber 2300P MBE system in our lab, shown in Fig. 1.1, was used for all the materials and structures growth.

By simply changing the composition, the bandgap of the barrier layer, $Zn_{x'}Cd_{y'}Mg_{1-x'-y'}Se$, can be tuned continuously from 2.1 eV to 3.6 eV. R-G-B full color light emitting diodes and photo-pumped lasers have been previously demonstrated by using this material system. Contactless electroreflectance (CER)

measurements reveal that the CBO of this material system is as large as 1.12eV. Based on these qualities, we proposed that the wide bandgap material system $Zn_xCd_{1-x}Se/Zn_{x'}Cd_{y'}Mg_{1-x'-y'}Se$ may be used to design entirely lattice matched structures that also meet the band structure requirements of these complex ISB devices.

Figure 1.1 Picture of the Riber 2300P MBE system in our lab.

The work in this thesis involves the design, growth, and characterization of $Zn_xCd_{1-x}Se/Zn_{x'}Cd_{y'}Mg_{1-x'-y'}Se$ based heterostructures and device structures that can be used to fabricate devices that are based on intersubband transitions.

In the following chapters, I will discuss the results in detail.

In chapter 2, the properties of the $Zn_xCd_{1-x}Se/Zn_{x'}Cd_{y'}Mg_{1-x'-y'}Se$ material system and the basics of MBE growth are presented first. Then, an introduction

to intersubband devices, such as quantum well infrared photodetectors and quantum cascade lasers, is given.

Chapter 3 focuses on the methods used to characterize the samples made from this material system.

Chapter 4 presents the theoretical background of calculating energy levels within a quantum well structure by the envelope function approximation and the experimental methods used to determine the band offsets.

Chapter 5 contains work on ZnCdSe/ZnCdMgSe QWIP structures. From the growth of these structures by MBE, the material and structural qualities of the materials are discussed in detail. Also, a physical evaluation of the competition between radiative and non-radiative recombination process is given based on experimental results.

Chapter 6 describes the CER studies on $Zn_xCd_{1-x}Se$/ $Zn_{x'}Cd_{y'}Mg_{1-x'-y'}Se$ multiple quantum well structures. This method was proven to be a useful technique for determining intersubband transitions.

Chapter 7 gives the intersubband absorption measurements made by FTIR on $Zn_xCd_{1-x}Se$/ $Zn_{x'}Cd_{y'}Mg_{1-x'-y'}Se$ multiple quantum well structures. Different ISB transition mechanisms are discussed.

Finally, all the results and contributions of this work are summarized in Chapter 8. Future directions of this project are given including both the device structure design and device fabrication.

Chapter 2

Background

In this chapter, an introduction to the material system that we employ, which is the wide bandgap $Zn_{x'}Cd_{y'}Mg_{1-x'-y'}Se$ alloy, the material growth technique, which is molecular beam epitaxy (MBE), and the type of devices of interest, which are the mid-infrared intersubband (ISB) devices, is given from both the fundamental and applications points of view. From this background we have derived the motivation of this thesis. The proposed work is given at the end of the chapter.

2.1 II-VI wide bandgap $Zn_{x'}Cd_{y'}Mg_{1-x'-y'}Se$ alloy

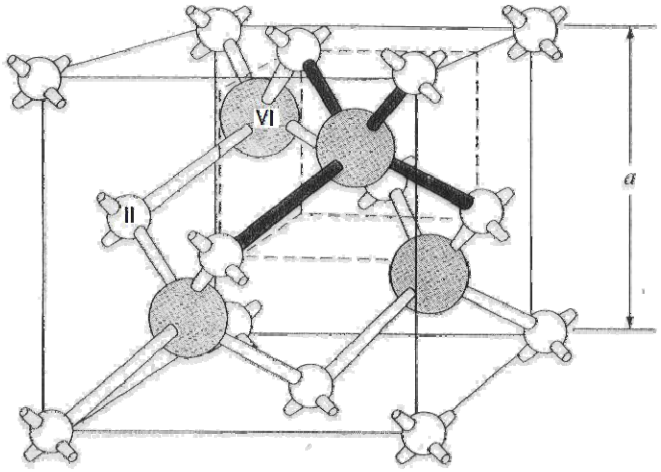

Figure 2.1 Zincblende II-VI semiconductor unit cell structure.

II element: Zn, Cd, Mg; VI element: Se.

The wide bandgap $Zn_{x'}Cd_{y'}Mg_{1-x'-y'}Se$ alloy is a quaternary material system that has the zincblende crystal structure. It can be seen clearly in Fig. 2.1, which shows the unit cell for a zincblende structure, that group II atoms form a face-centered cubic lattice while group VI atoms form tetrahedral bonds with the group II atoms and occupy one half of all the possible sites. Since most available substrates, in particular GaAs or InP, are of zincblende structures, it is possible to grow the II-VI materials epitaxially on these substrates. In the actual $Zn_{x'}Cd_{y'}Mg_{1-x'-y'}Se$ quaternary crystal, which is an alloy of ZnSe, CdSe and MgSe, the sites of group-II atoms can be occupied by Zn, Cd or Mg atoms while only Se atoms occupy the sites of group-VI atoms. By changing the composition (i.e., the relative quantities of ZnSe, CdSe, and MgSe), the lattice parameters, bandgaps and other properties of this II-VI material system can be tuned over a very broad range.

Figure 2.2 shows the relationship between the bandgap of $Zn_{x'}Cd_{y'}Mg_{1-x'-y'}Se$ at 77K and the lattice-mismatch of a relaxed layer of this alloy to InP. We choose to plot it this way because InP is our most commonly used substrate material. The zero-mismatch position is indicated by a vertical dashed-line. The three solid squares represent the position of the binary materials ZnSe, CdSe and MgSe. The solid line represents the empirical fit to the ternary $Zn_xCd_{1-x}Se$ data reported in the literature.[2] The two dashed-lines representing $Zn_{x'}Mg_{1-x'}Se$ and $Cd_{y'}Mg_{1-y'}Se$ are the other ternary boundaries of the $Zn_{x'}Cd_{y'}Mg_{1-x'-y'}Se$

quaternary material. The lattice-matched ZnCdSe material has a 77K bandgap of about 2.18 eV. By adding Mg into the $Zn_xCd_{1-x}Se$ ternary, and adjusting the ZnSe/CdSe ratio, the bandgap of the $Zn_{x'}Cd_{y'}Mg_{1-x'-y'}Se$ quaternary material can be varied from 2.18 eV to about 3.6 eV, while maintaining lattice-matching conditions to InP. In our lab, by using different bandgap $Zn_{x'}Cd_{y'}Mg_{1-x'-y'}Se$ layers as the barrier layers and lattice-matched $Zn_xCd_{1-x}Se$ layers as the well layer, lattice matched quantum well (QW) structures with the emission covering almost the entire visible wavelength range have been demonstrated and used in the design and fabrication of red, green and blue (R-G-B) lasers and LEDs.[3,4,5,6]

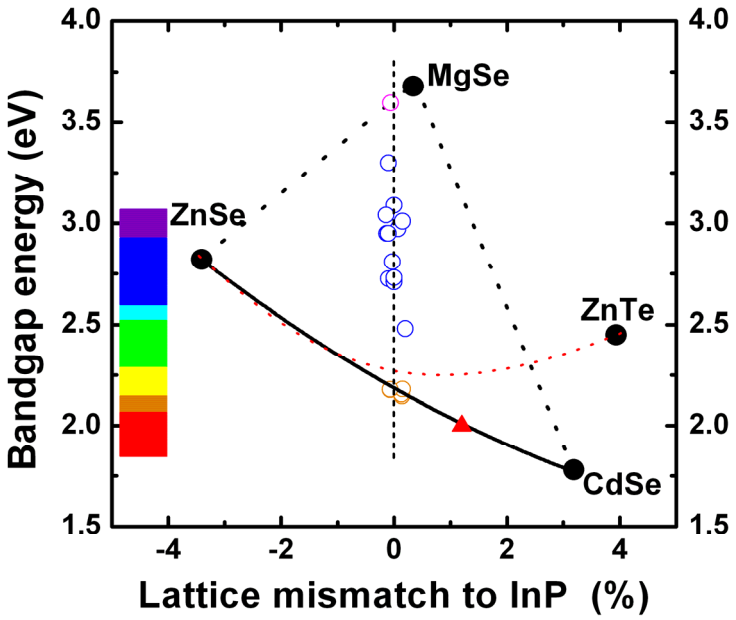

Figure 2.2 Bandgap as a function of lattice mismatch to InP for $Zn_{x'}Cd_{y'}Mg_{1-x'-y'}Se$ material system.

According to our recent research findings, the conduction band offset (CBO) of this system has been determined[7] and a large tunable CBO as large as 1.12 eV[8] has been demonstrated. For ISB devices operating in the near–infrared and mid-infrared ranges, a large band discontinuity is desired, making this II-VI material system a very good candidate.

2.2 Molecular beam epitaxy technique

2.2.1 MBE process

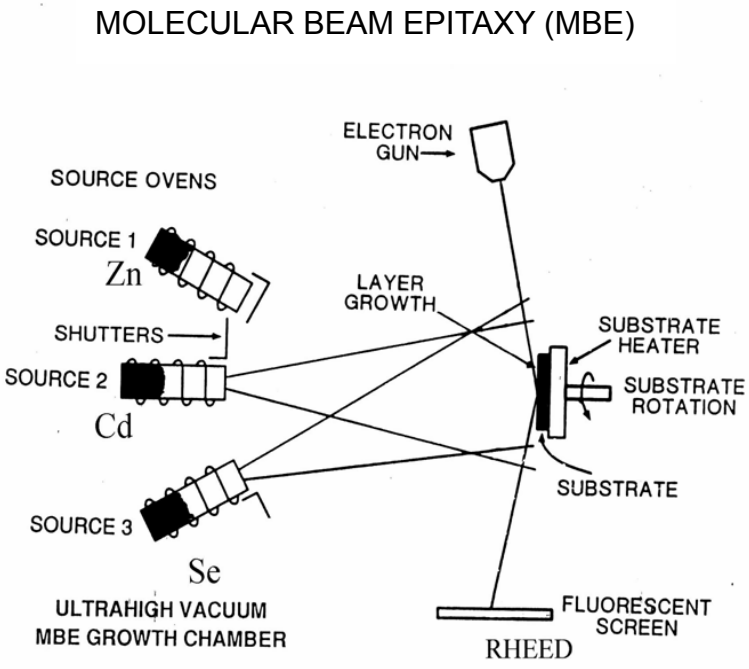

Figure 2.3 Schematic diagram of MBE process.

Molecular beam epitaxy (MBE) is used as the growth technique to achieve multi-layered structures with high material quality and complex device structures.

The MBE process achieves epitaxial growth in an ultra-high vacuum (UHV) environment through the chemical reaction of one or more thermal molecular beams with a crystalline surface of the substrate. This process is illustrated schematically in Fig. 2.3 which shows the essential components for MBE growth of ZnCdSe. All the components are in an UHV environment. The substrate, which is mounted on a substrate manipulator, can be rotated while maintaining an accurate substrate temperature for a uniform epitaxial growth. Molecular beams are provided by thermal Knudsen effusion cells which contain a crucible with one of the material sources for the desired epilayer. The temperature of each cell is chosen so that the vapor pressures of the materials are sufficiently high for generation of thermal energy molecular beams by free evaporation. The cells are arranged so that the central portion of the beam flux distribution from each cell intersects the substrate. Each cell has a shutter between the cell and the substrate. By choosing the appropriate cell, through the opening of its shutter, and the appropriate substrate temperature, epitaxial layers of precise compositions and complex multi-layered device structures can be obtained. The extremely high precision in the beam flux control allows the growth of very thin layers, even single atomic layers or mono-layers. This distinguishing characteristic has enabled MBE to become one of the principal growth techniques for low dimensional heterostructures including quantum wells and superlattices.

2.2.2 In-situ monitoring of the growth

Because of the ultra-high vacuum environment, MBE is compatible with in-situ electron diffraction techniques to monitor the surface during the growth and to establish pre-growth treatments such as substrate deoxidization. In Fig. 2.4, the in-situ reflection high energy electron diffraction (RHEED) technique is illustrated.

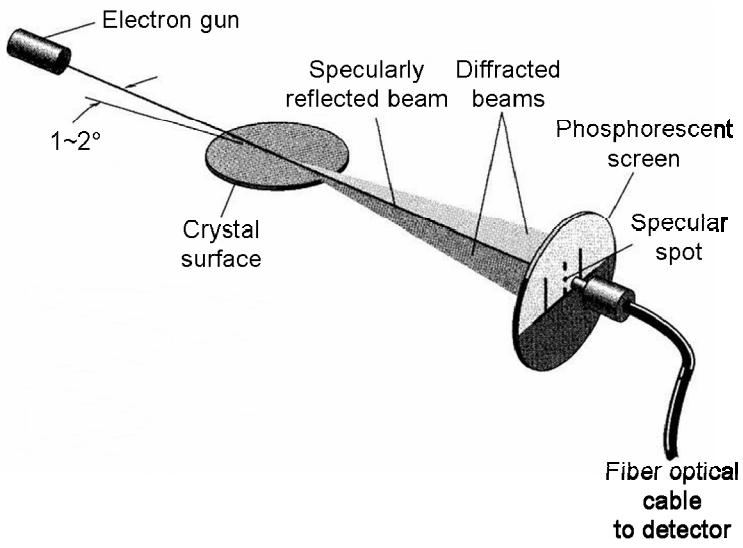

Figure 2.4 Schematic of a RHEED system.

RHEED uses very high energy electrons and glancing incidence. This geometry allows the diffraction pattern produced by the crystalline surface to be observed while the growth is going on, as the molecular beams are directed normal to the surface. The glancing incidence also ensures that the high energy electrons only penetrate to a very thin layer on the surface. This is true because the penetration depth of the incident electron beam depends on the energy

component normal to the surface. This normal component is very small (~ 150 eV) in RHEED even though the electrons have an energy of ~10 keV and the diffraction gives information about a very thin layer near the surface. Therefore RHEED is very sensitive to the surface properties, and is an ideal method to monitor the surface in-situ.

The RHEED pattern depends on the atomic arrangement, flatness of the surface and the crystalline direction of the growth surface. The typical RHEED pattern for a disordered surface (for example before the deoxidization) is a diffuse pattern or rings due to the thin amorphous oxide layer on the surface. For a clean surface after thermal deoxidization, the pattern is streaky lines or ordered spots.[9] For three dimensional growth, where significant surface roughness exists, it is ordered spots such as a bulk crystal pattern; for two dimensional (atomically smooth) growth, it is in the form of rods (“streaky”), and exhibits a surface reconstruction. The (001) place of the substrate is usually used as the growth plane. For the II-VI material, the crystal structure can be illustrated as layers of alternating II and VI layers along the [001] direction. The reconstruction of the surface, which refers to the formation of surface dimers by the atoms in the last layers, with dangling bonds, will introduce changes of RHEED patterns. The typical surface reconstructions for an As-rich (001) InGaAs surface is a (2×4) reconstruction, while for a Se-rich (001) ZnSe the typical pattern shows a (2×1) surface reconstruction. Thus, from the RHEED pattern we can know whether the

deoxidization is finished, whether growth is two dimensional, and which element terminates the surface.

2.2.3 MBE system

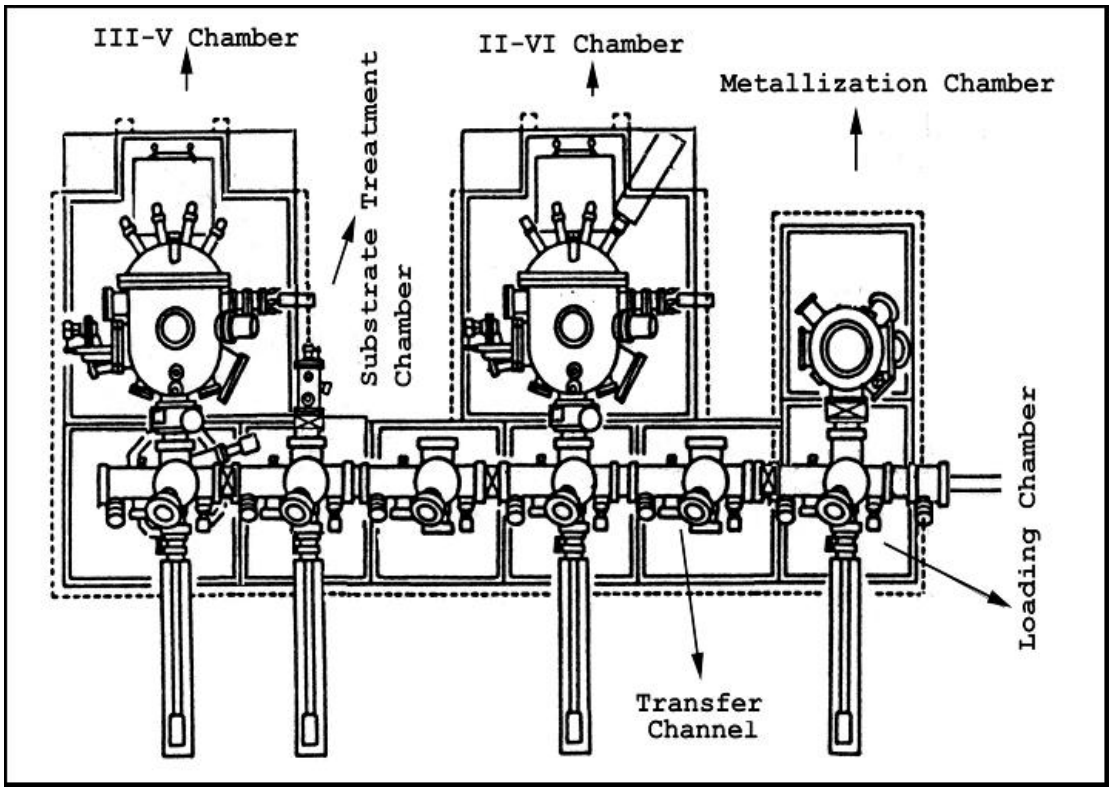

Figure 2.5 Illustration of Riber 2300P MBE system.

The experiments in this dissertation were done in a Riber 2300P MBE system. Figure 2.5 shows a schematic of the top-view of the system. The system includes 6 chambers: loading chamber, transfer channel, substrate treatment chamber, metallization chamber, and two growth chambers, one dedicated to III-V materials and the other one dedicated to II-VI materials growth. To achieve an

ultra-high vacuum, all the chambers are equipped with high vacuum pumps, including ion pumps, cryo-pumps, turbo pumps, etc. These pumps usually can maintain the vacuum of the system in the range of 10^{-9} ~ 10^{-10} Torr. The loading chamber is used for introducing the substrates into the vacuum system. There is a gate valve between the loading chamber and the other chambers which allows us to vent the loading chamber without breaking the vacuum of the other chambers. The substrates or samples can be transferred within the system through the transfer channel.

The chambers for the growth of III-V and II-VI semiconductor materials are similar. Each is equipped with a substrate manipulator (holder, rotator, heater and temperature sensor of the substrates), cells, RHEED, quadrupole mass spectrometer, and cryo-shrouds around the manipulator and the cells. These cryo-shrouds will have a flow of liquid nitrogen (LN) through them during growth to prevent the thermal interference between the sources and also trap the residual molecules inside the chamber to maintain UHV conditions. There are 8 cells with the desired material sources available in each chamber.

2.2.4 MBE growth of lattice-matched $Zn_{x'}Cd_{y'}Mg_{1-x'-y'}Se$ alloy and $Zn_xCd_{1-x}Se/Zn_{x'}Cd_{y'}Mg_{1-x'-y'}Se$ quantum well structures on InP substrates

Growing a II-VI material on III-VI substrate surface is a challenge. In previous studies, our group has been able to optimize the growth conditions and

demonstrate excellent material quality of $Zn_{x'}Cd_{y'}Mg_{1-x'-y'}Se$ alloy and other related II-VI structures. The growth consists of four parts: pre-growth substrate treatment, III-V buffer layer growth, II-VI/III-VI interface treatment, and II-VI structure growth.

Prior to use, the substrates (primarily InP in this thesis) were degreased by using trichloroethylene (TCE), acetone and methanol and etched in H_2SO_4:H_2O_2:H_2O (4:1:1) for 1 minute to remove the residual polishing damage. Then an oxide layer was formed on the surface by flushing the wafers with deionized water to protect the fresh InP surface from contamination of carbon. The substrates were then bonded onto a Molybdenum block using Indium and introduced into the MBE system through the loading chamber. The oxide desorption of the substrate was performed in the III-V chamber by heating the substrate with an As flux impingent on the InP surface. This is done to prevent the loss of P atoms during the heating and formation of an In-rich surface on the InP substrate.[10] This procedure can be done by carefully heating the substrate until the 2-fold structure of the RHEED pattern changes to 4-fold structure (indicating an In rich surface), which confirms the the loss of the entire oxide layer. At this point, the temperature is quickly lowered to regain the 2-fold (As rich) pattern. In an ambient of As, the P lost by thermal desorption is replaced by the impinging flux and a thin InAs layer is formed on the surface.[11] To further improve

the substrate surface, in particular to improve its smoothness, a lattice matched III-V buffer layer, usually InGaAs is grown. After the growth of the III-V buffer layer, the substrate was transferred quickly, in vacuum, to the II-VI chamber.

Due to the difference in the electronic structure of the two materials, the preparation of the II-VI/III-V interface is very critical to the growth of II-VI material on III-V surface. The treatments used to adjust quality of the interface are: 1) Zn irradiation of the As-rich III-V surface before the initial growth of II-VI material,[12] that is, exposure of the III-V surface to Zn before the II-VI growth. This is done to avoid the interaction of Se with the III-V surface. In our case, it is known that an interfacial compound of In_2Se_3 and/or Ga_2Se_3 can form at the II-VI/III-V interface. This results in defects that limit the quality of the II-VI layer. 2) A ZnCdSe buffer layer grown at low temperature (~170 ^oC). It has been shown that by incorporating a thin ZnCdSe buffer layer grown at low temperature on the III-V buffer layer, the probability of intermixing of II-VI and III-V materials is reduced, and the quality of $Zn_{x'}Cd_{y'}Mg_{1-x'-y'}Se$ epilayers is greatly improved.

The substrate temperature is then increased to 270 ^oC, which has been proven to be the optimum growth temperature for $Zn_{x'}Cd_{y'}Mg_{1-x'-y'}Se$ based II-VI materials, to grow the desired II-VI epilayers or structures. The excellent material and structural quality of these samples will be demonstrated by many characterization methods later on in this work.

2.3 Mid-infrared intersubband devices

Intersubband devices, such as quantum well infrared photodetectors (QWIPs) and quantum cascade lasers (QCLs) operating in the mid-infrared (mid-IR) range, have potential advantages over conventional interband devices due to the increased ability to engineer the devices, as well as their intrinsic faster lifetimes and higher quantum efficiencies. Most of the ISB devices demonstrated so far have been fabricated with III-V compound semiconductors.[13,18] Band structure engineering has made it possible to achieve ISB devices operating over a wide spectrum range without the need to change the material system. For example, QCLs that emit in a very wide wavelength range (~3.4 to 24 μm) have been realized with InP-based InGaAs/InAlAs material system[14,15] after the first demonstration by Faist et al in 1994.[16] Intersubband devices are usually made from multiple quantum well (MQW) structures and need a large band discontinuity to achieve operation at shorter wavelength and higher temperatures.

2.3.1 Why mid-IR?

The mid-infrared (mid-IR) range usually referring to the wavelength range between 3-30 μm, is of great interest from both scientific and technological points of view. Often called the “molecular-fingerprint” region, mid-IR is the part of the spectrum where gases and vapors have evident absorption features associated

with vibrational and rotational transitions. These features can be observed by a number of spectroscopic techniques for a wide range of industrial, military, and scientific applications.[17] The two wavelength regions (3-5 μm and 8-13 μm) in which the atmosphere is relatively transparent due to lack of water-vapor absorption are particularly important for chemical-sensing applications. These windows allow the measurement of traces of environmental and toxic gases or vapors that would otherwise be masked by a large atmospheric water-vapor background.

2.3.2 Intersubband transitions

Within a bulk semiconductor crystal, electrons may occupy states in one of two continuous energy bands - the valence band (VB), which is heavily populated with low energy electrons and the conduction band (CB), which is sparsely populated with high energy electrons. The two energy bands are separated by an energy bandgap in which there are no permitted states for electrons to occupy. When the electrons in the CB combine with the holes (or vacant states) in the VB, an interband transition occurs.

A quantum well (QW) structure is formed, as shown in Fig. 2.6, by sandwiching a layer of material with lower bandgap between two barrier layers of another material with higher bandgap. When the QW is sufficiently deep and

narrow, its energy states are quantized (discrete). Depending on the dimensions of the QW and the materials from which they are formed, there can be several discrtete states within a QW. In that case, intersubband (ISB) transitions can occur between these discrete energy levels, within a band (either the CB or the VB). In contrast to interband transitions, ISB transitions are unipolar (involving either electrons or holes, but not both) with faster relaxation times.

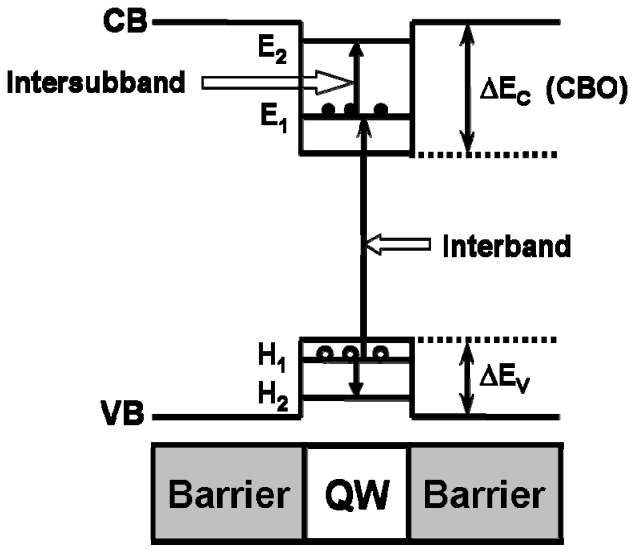

Figure 2.6 Schematic illustration of interband and ISB transitions occur in a single quantum well structure.

2.3.3 Quantum well infrared photodetectors (QWIPs)

A quantum well structure designed to detect infrared (IR) light involving ISB transitions is called a quantum well infrared photodetector (QWIP).[18] The QWs in a QWIP structure have to be doped to exhibit ISB absorption by the

excitation of an electron (or hole) from the doped QW ground state in the CB (or VB) to an unoccupied excited state in the same band. An elegant model for a QWIP is based on the square QW of basic quantum mechanics. The potential depth and width of the well can be adjusted so that it holds only two energy states: a ground state near the well bottom, and the first excited state near the well top. A photon striking the well will excite an electron in the ground state to the first excited state, and then an externally-applied voltage sweeps it out to the continuum, producing a photocurrent (Fig. 2.7).

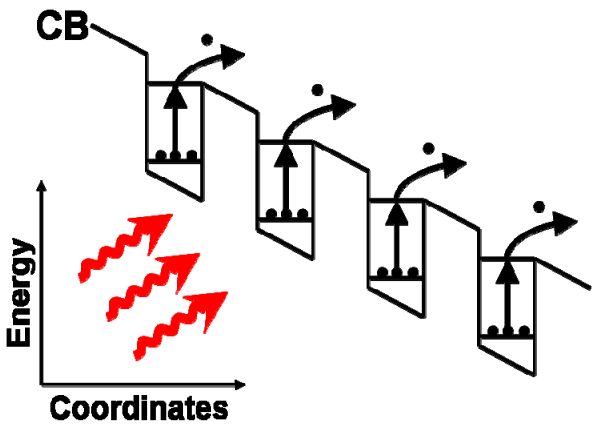

Figure 2.7 Schematic illustration of the conduction band of a QWIP active region.

Due to the unipolar transport property (only one band is involved), only the conduction band is shown in Fig. 2.7. The MQW band structure tilts because of the application of external electric field. Only photons having energies

corresponding to the energy separation between the two states are absorbed, resulting in detection with a sharp absorption spectrum. Designing a QW to detect light of a particular wavelength becomes a simple matter of tailoring the potential depth and width of the well to produce two states separated by the desired photon energy. The presence of many equivalent wells ensures that high quantum efficiencies can be achieved.

2.3.4 Quantum cascade lasers (QCLs)

Conventional semiconductor lasers rely on a single photon of light being emitted when a high energy electron from the conduction band combines with an unoccupied hole in the valence band. The wavelength of light emitted is therefore strongly dependent upon the energy bandgap of the laser material. The quantum cascade laser (QCL) however does not use bulk semiconductor materials in its optically active region. Instead, it consists of a periodic series of thin layers of varying material composition. The varying composition introduces a varying electric potential across the length of the device, meaning that there is a varying probability of electrons occupying different positions over the length of the device. This is referred to as one-dimensional multiple quantum well confinement and leads to the splitting of the band of permitted energies into a number of electronic subbands.

By careful selection of material composition and thickness of each layer in the device, and the applied external electric field, an electric subband minimum in a given period of the device may be aligned with a higher energy subband minimum in the adjacent period. Therefore, an electron may take part in an optical transition between electronic subbands in a given period before tunneling into the next period of the structure and performing another optical transition.

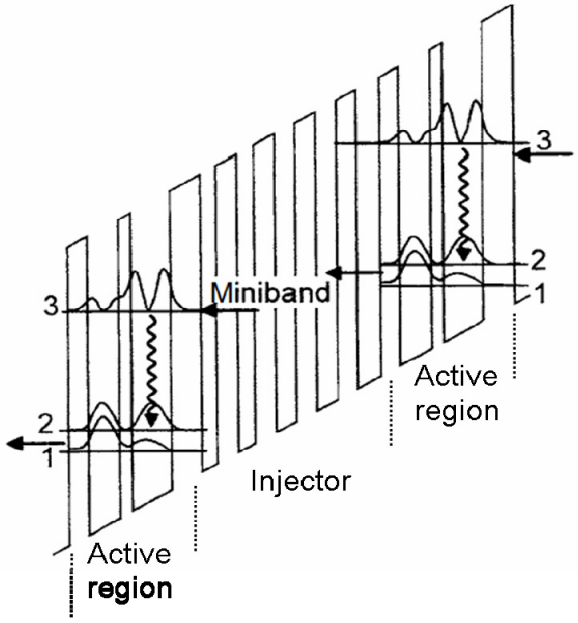

Figure 2.8 Schematic CB energy diagram of two QCL active regions with the intermediate injector region based on a three-well vertical transition mechanism. The laser transition is indicated by the wavy arrows and the electron flow by the straight arrows.

Shown in Fig. 2.8 is the illustration of a QCL active region design, based on the so-called “double-QW vertical” transition design. The coupling of the two QWs (with difference QW width) produces three energy levels. The lasing will be due to the transition from “3” to “2” and the additional third level “1” which is close in energy to level “2” will be the means to empty level “2” by phonon scattering. The depopulation process will ensure population inversion, as needed for lasing, and the electrons will keep moving through the device, giving high optical power output (high quantum efficiency).

Quantum cascade lasers (QCLs) have a wide range of applications, such as trace-gas analysis and chemical sensing with the ability to detect minute amounts of chemicals found in the environment or atmosphere, emitted from spills, combustion, or natural sources, or exhaled in human breath. Laser-based optical methods in trace-gas analysis and chemical sensing have a number of advantages, including their noninvasive nature, high sensitivity and selectivity, and real-time detection. A variety of spectroscopic methods can determine the local concentration of a species with parts per million in volume (ppbv) sensitivity. Most of them require tunable single-mode mid-IR lasers with power levels sufficient to obtain a good signal-to-noise ratio. Some commercial devices such as field point sensors also need to be portable, so they require compact, room-temperature battery-operated light sources. However, existing mid-IR sources

rarely meet these requirements, while QCLs readily satisfy them and have already been used in many trace-gas analyses.[19,20,21,22]

2.4 Proposed work

Despite the tremendous progress that has been made in ISB devices, there are still some limitations. For example, most of the QCLs can only perform at cryogenic temperature, with pulsed operation mode and relatively low power outputs. So far, the shortest wavelength that has been achieved for a QCL operating at room temperature (RT) is ~4 μm with a strain-compensated InGaAs/InAlAs heterostructure.[7] One of the reasons that it is difficult to achieve RT short wavelength operation is the small conduction band offset (CBO) of the heterostructures used. For some applications such as trace gas sensing, infrared lasers with wavelength shorter than 4 μm operating at RT are required. [2, 8] To achieve QCLs operating at high temperature with a shorter emission wavelength, materials with larger CBO must be used. One approach to achieve the larger CBO is to use the type-II band alignment in InAs/AlSb, InGaAs/AlAsSb [9, 10, 11] and (CdS/ZnSe)/BeTe [12, 13]. However, the growth of these materials is more difficult, due to the lack of common ions, and the type II structure may introduce additional complications in the operation of the device. The only effort for achieving shorter wavelength devices with a material having a type-I band alignment has been with the wide band gap GaN/AlGaN system. [14, 15, 16 , 17

Although ISB absorption in QWs at wavelength as short as 1.08 μm has been observed, [18] the poor material quality (high defect density and poor interfacial quality due to the lack of lattice-matched substrate) makes it very difficult to realize a practical working device, which typically consists of hundreds of layers. Both direct and indirect semiconductors are good light absorbers for energies above the bandgap and have been widely employed for photodetector applications. However, bandgap light emission from indirect semiconductors is a low efficiency process because of the need of the participation of phonons in order to satisfy wave-vector conservation. Thus, for the case of efficient light emitters, direct bandgap materials are preferred. The II-VI wide bandgap materials $Zn_{x'}Cd_{y'}Mg_{1-x'-y'}Se$ alloys are direct semiconductors, the heterostructures are type-I, and, as the work to be presented in this thesis shows, the materials can be grown with extremely high crystalline quality.

We propose that a wide bandgap II-VI material system, $Zn_xCd_{1-x}Se/Zn_{x'}Cd_{y'}Mg_{1-x'-y'}Se$, which has a large CBO with a type-I band alignment and which can be grown lattice-matched on InP substrates, is a very promising candidate for realizing shorter wavelength ISB devices operating at RT. By simply changing the composition, the bandgap of the barrier layer, $Zn_{x'}Cd_{y'}Mg_{1-x'-y'}Se$, can be tuned continuously from 2.1 eV to 3.6 eV.[23] Contactless electroreflectance (CER) measurements have revealed that a CBO as large as 1.12eV can be achieved in the heterostructures of this material system.[8]

Furthermore, the widely accepted limitations of II-VI materials, namely the lack of high enough p-type doping and their degradation due to p-type doping related defect propagation during operation, do not apply to these types of ISB devices, which are unipolar, low energy devices.

Chapter 3

Characterization techniques

In this chapter, characterization methods including Photoluminescence (PL) spectroscopy, X-ray diffraction (XRD), Hall Effect measurements, electrochemical capacitance-voltage (ECV) profiling, Scanning electron microscope (SEM), Time-resolved photoluminescence, Contactless electroreflectance (CER), and Fourier transform infrared (FTIR) spectroscopy, all used for evaluating the material quality are described in detail.

3.1 X-ray diffraction

X-ray diffraction (XRD) is one of the most powerful and widely used techniques for accurate characterization of the lattice parameters, mismatch, alloy composition, and thickness of epitaxial materials. In this section, we use a series of advanced X-ray diffraction techniques, including single and double-axis diffraction, and high resolution triple-axis diffraction to characterize samples from single epitaxial layers to complex superlattice structures.

3.1.1 Bragg's law

The principle of the XRD is based on Bragg's law shown schematically in Fig. 3.1:

$$2d_{hkl}\sin\theta = n\lambda, \qquad n = 1, 2, 3\ldots \tag{3.1}$$

where $d_{hkl} = \frac{a}{\sqrt{h^2 + k^2 + l^2}}$ (a is the lattice constant) is the spacing of lattice planes with Miller indices (hkl) and θ is the corresponding Bragg angle. The lattice constant (a) of an unknown layer can be calculated if the Bragg angle is known. Usually the epilayers are grown on the (001) plane of the substrate, therefore, an XRD measurement can be performed on a symmetry lattice plane (the (hkl) planes indicated in Fig. 3.1). Among them, the (004) plane is mostly used in our experiments.

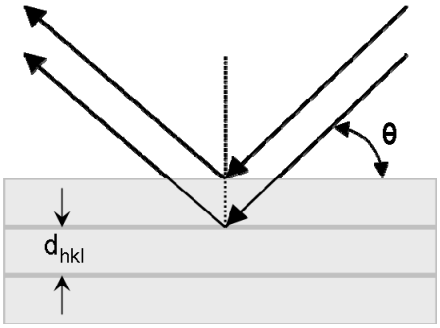

Figure 3.1 Principle of X-ray diffraction. θ is the Bragg angle and d_{hkl} is the distance between (hkl) planes.

3.1.2 Analysis of thin films and multiple layers

a) Lattice mismatch and strain

The mismatch (Δa) of an epitaxial layer grown on a given substrate is defined by:

$$\Delta a = \frac{a_L - a_S}{a_S} \tag{3.2}$$

where a_L and a_S are the bulk lattice parameters of the epitaxial layer and

substrate, respectively, and where the two unit cells are assumed to be in the same direction. It is assumed that a_L is the value of the layer in its cubic form, not the elastically distorted parameters if the layer is strained.

The strain state of the epitaxial layer is an important parameter. With the same thickness and lattice-mismatch, the layer that is pseudomorphic has better quality than a relaxed or partially relaxed layer. In the calculation of composition, we need to know the strain state in the epilayer. When the epilayer is pseudomorphic or fully strained, the structure will be tetragonally distorted. The lateral lattice constant ($a_{//}$) of the epilayer in the plane is equal to the lattice constant of the substrate. The perpendicular lattice constant ($a_{\perp}$) in the growth direction could be obtained from the XRD data. The lattice constant of the epilayer is given by:

$$a_L = \frac{1-\upsilon}{1+\upsilon} a_{\perp} + \frac{2\upsilon}{1+\upsilon} a_{//}, \tag{3.3}$$

where υ is the Poisson constant, which is 0.28 for the $Zn_{x'}Cd_{y'}Mg_{1-x'-y'}Se$ material system. The lattice mismatch, in this case, can be expressed as

$$\Delta a = \frac{a_L - a_S}{a_S} = \frac{1-\upsilon}{1+\upsilon} \Delta a_{\perp}, \qquad a_{//} = a_S \tag{3.4}$$

When the epilayer is fully relaxed (broadened peak), $a_{//}$ and $a_{\perp}$ will be the same and $\Delta a = \Delta a_{//} = \Delta a_{\perp}$. In the case of a partially relaxed epilayer, it is more complicated and additional XRD measurements on asymmetric planes (i.e. (115) plane) will be needed to calculate the actual strain.

b) Periodicity of multiple layers

For our multiple quantum well (MQW) structures with periodic sequences of layers of alternating composition, a sequence of equally-spaced satellite peaks associated with the superlattice structure will show up in the XRD spectrum. The separation of the satellite peaks depends on the periodicity of the repeating layers. Let m and n be two diffraction orders due to the same periodicity (p), and θ_m and θ_n the corresponding Bragg angles, Bragg's law can be written by

$$2p \cdot \sin\theta_m = m\lambda, \qquad m = 1, 2, 3\ldots$$

$$2p \cdot \sin\theta_n = n\lambda, \qquad n = 1, 2, 3\ldots$$

Therefore, the periodicity is given by

$$p = \frac{(m-n)\lambda}{2(\sin\theta_m - \sin\theta_n)}. \tag{3.5}$$

If we assume $m - n = 1$, and if $\Delta\theta = \theta_m - \theta_n$ is small enough compared with θ_n, Eq. (3.5) may be simplified to

$$p = \frac{\lambda}{2\cos\theta_n \cdot \Delta\theta}. \tag{3.6}$$

3.1.3 Single and double crystal X-ray diffraction

Figure 3.2 shows the schematic diagram of our XRD setup, which consists of an X-ray source, a single crystal X-ray diffraction (SCXRD) system shown on the right manufactured by RIGAKU and a double crystal X-ray diffraction (DCXRD) system shown on the left manufactured by Blake Industries, Inc. The X-ray is generated by a Cu X-ray source and the two lines of Cu $K_{\alpha 1}$ (λ = 1.54056

Å) and Cu $K_{\alpha 2}$ (λ = 1.54439 Å) are the ones usually used. In both cases, the incident angle ω will change due to the rotation of the sample holder while the rotation of the goniometer (where the detector is mounted) will change the angle 2θ.

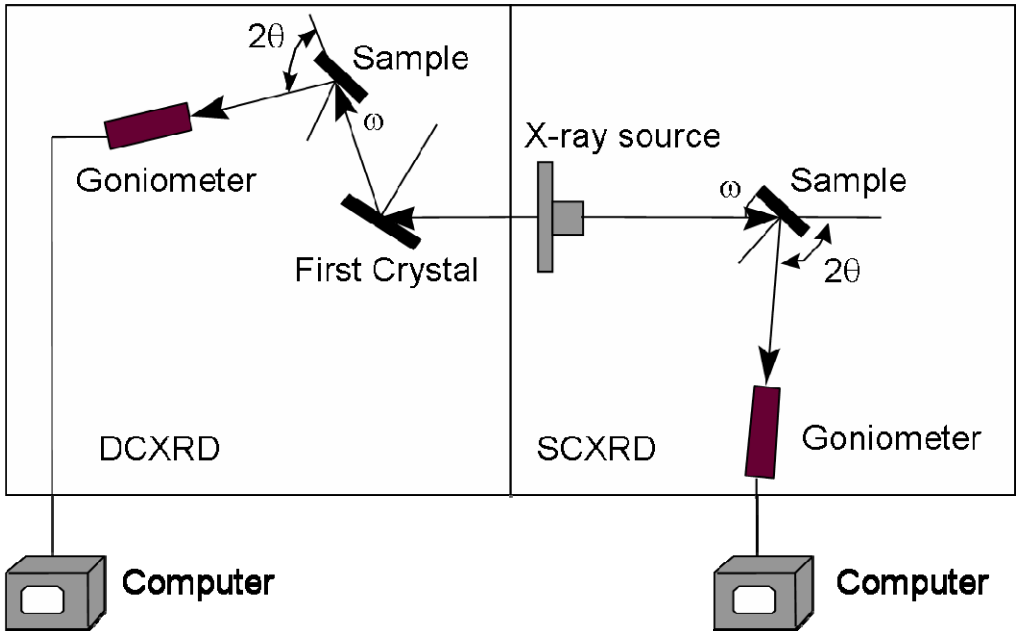

Figure 3.2 Illustration of single and double crystal X-ray diffraction system.

In SCXRD, only one crystal (the sample) is used, so the incident X-ray here is not monochromatic, and does not separate the Cu $K_{\alpha 1}$ and Cu $K_{\alpha 2}$ lines. Therefore, the diffraction spectrum for each layer (lattice constant) will typically show two peaks corresponding to diffraction from the Cu $K_{\alpha 1}$ and Cu $K_{\alpha 2}$ lines. Usually the intensity of the peak corresponding to Cu $K_{\alpha 1}$ is double that of the peak corresponding to Cu $K_{\alpha 2}$, which gives us a clue to identify diffraction peaks. In SCXRD, we usually use the θ-2θ coupled mode, which means that the angle ω

and 2θ are moving simultaneously and ω is always half of 2θ. In the practical measurement, to make sure ω and 2θ are coupled, we fix the 2θ and rotate the ω only (usually called a rocking curve) to find the ω value corresponding to the peak and adjust it to the value of θ. The θ-2θ coupled mode makes SCXRD useful to measure large lattice-mismatch and to find the structure of the materials. However, because the beam has a broad band of wavelengths, the diffraction peaks are usually broad. For a more accurate determination of lattice parameters of materials, a DCXRD rocking curve is necessary.

Double crystal XRD is a very direct and useful way to evaluate the quality of the epitaxial layer and the lattice mismatch between the epitaxial layers and the substrate. The setup (as shown in Fig. 3.2) consists of the monochromator crystal (first crystal) and the sample crystal from which the diffracted intensity signal is registered depending on the angle of rotation of the sample. In our system a (100) Ge crystal is used as the monochromator to separate the various wavelengths of the incident X-ray beam in order to narrow the X-ray band of wavelengths before it reaches the sample. So the Cu $K_{\alpha 2}$ line can be filtered and only the Cu $K_{\alpha 1}$ line with a narrow spread of wavelengths will reach the sample crystal. In DCXRD, a rocking curve is usually measured, that is, we rotate the sample (ω) while the goniometer (2θ) and the first crystal are fixed. The linewidth of the X-ray line reflected from the sample depends strongly on the crystalline quality of the sample. Thus, this technique is particularly useful for epitaxial

layers grown on a thick substrate. In general, for such cases, two diffraction peaks are observed, one from the substrate and one from the epilayer. From the linewidth, we can evaluate the material quality. From the peak separation, we can obtain the lattice-mismatch.

For MQW structures, the observation of many satellite peaks will be a strong evidence of excellent material and structural quality. In our DCXRD system, the detector (on the goniometer) with an open slit is fixed which integrates the intensity scattered by the sample over its acceptance angle (in our system it is about one degree around the center peak). A XRD system with high resolution is needed. In the next section, a high resolution (HR) triple axis XRD system using highly intense synchrotron radiation (National Synchrotron Light Source in Brookhaven National Lab) will be discussed. HRXRD spectra on our II-VI MQW structures were obtained with this system.

3.1.4 High resolution triple-axis X-ray diffraction

Figure 3.3 is the schematic illustration of HR triple-axis diffractometry.[24] The addition of a further crystal (placed before the detector) to DCXRD scheme, a so called analyzer crystal, makes it possible to resolve with high resolution the angular distribution of the beam diffracted by the sample. It provides the possibility to distinguish the coherent and diffuse components of the total scattering signal.[25,26] In addition, from the analysis of the diffuse scattering distribution it is possible to get information about different types of defects in

crystals (point defects, clusters etc.).[27] An analyzer crystal enables also to distinguish between mosaic spread (multi-grains in the crystal) and strain (i.e. a gradient of a lattice parameter variation $\Delta d/d$) contributions in the diffracted intensity distribution.

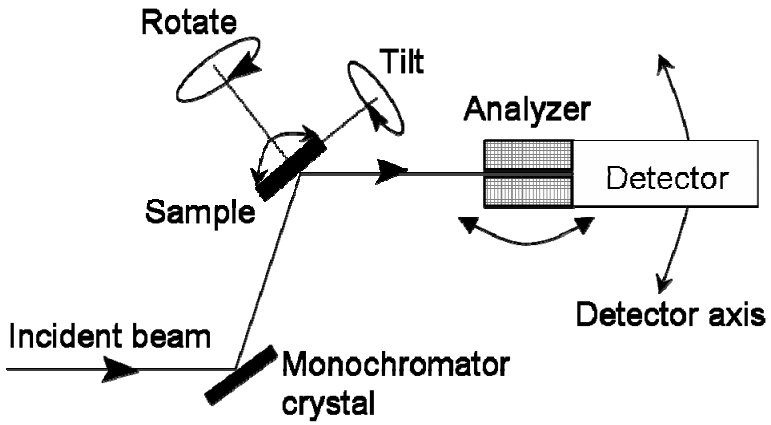

Figure 3.3 Schematic of HR triple-axis diffractometry.

By using highly intense synchrotron radiation it is possible to achieve a very high degree of collimation (sub-arcsec) and monochromatization of the X-ray beam by the use of multiple reflection monochromators and analyzer crystals. In our experiments, the X-ray line (λ = 1.54092 Å) of the synchrotron radiation source is used.

3.2 Photoluminescence spectroscopy

When the sample is irradiated with a photon beam with energy higher than the bandgap of the material, the absorbed photons bring electrons to the

conduction band (CB) leaving behind holes in the valence band (VB); that is, electron hole pairs are produced by the optical excitation. Photoluminescence (PL) occurs when the excited electron returns to its initial state and the return process emits a photon, whose energy gives the difference between the excited and the initial state energies. Therefore, PL spectroscopy is a very useful optical technique that, in the case of materials of good crystalline quality, can give direct information on the material's bandgap E_g. It can also give us information about bound states within the bandgap, such as bound excitons, donor or acceptor-bound excitons, and donor-acceptor pairs, etc. In addition, the PL spectrum can give us the information about the quality and band structure of the semiconductors of interest.

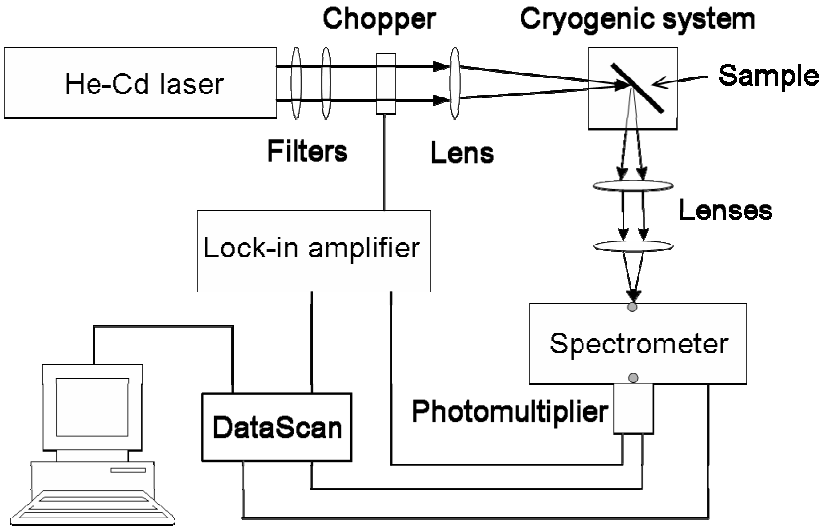

Figure 3.4 Experimental setup of photoluminescence.

The PL experiment consists of the measurement of the emitted light as a

function of wavelength. The schematic of the PL system used in this work is shown in Fig. 3.4. The samples are mounted on the cold finger of a Janis cryogenic system. The system can be pumped up to ~10^{-5} torr to maintain the low temperature. The cold finger can be cooled down to 5.8 K using liquid helium and 78 K using liquid nitrogen. Using a heater installed on the back of the cold finger, the temperature of the cold finger can be controlled from 5.8 K to 300 K. The 325 nm UV light from a He-Cd laser is picked up by an interference filter (λ = 325 nm) and used as the excitation source. A variable neutral density filter is used to adjust the power intensity of the laser beam. The laser beam passes through a chopper which changes the laser beam to a periodic signal (*ac*), then is focused to a small spot on the sample by a cylindrical converging lens. The luminescence from the sample is collected by two lenses and converted to a collimated beam. The collimated beam is focused to a spot on the first slit of the spectrometer (SPEX 1680-B double spectrometer). After passing through the spectrometer, the beam is detected by a photomultiplier and converted to an electrical signal. The ac signal is then fed to a lock-in amplifier to be amplified. Finally the amplified signal is feed into a data box (DataScan) connected to the computer to be collected and analyzed. The data box also connects the spectrometer to the computer so that the spectrometer can be controlled during the scan.

3.3 Time-resolved Photoluminescence

Time-resolved spectroscopy techniques are a powerful means of studying

materials, giving information about the nature of the excitations, energy transfer, molecular motion, and molecular environment, information that is not available from steady-state measurements. It is a rapidly advancing field with applications in many areas of science and technology. The dynamics of photo-excited carriers in a semiconductor can be probed by monitoring its time resolved PL. The most widely accepted technique for monitoring luminescence with ultra-fast resolution is the excite-and-probe method. In this technique the laser pulse itself acts as a switching gate and relates the PL signal with the time domain.

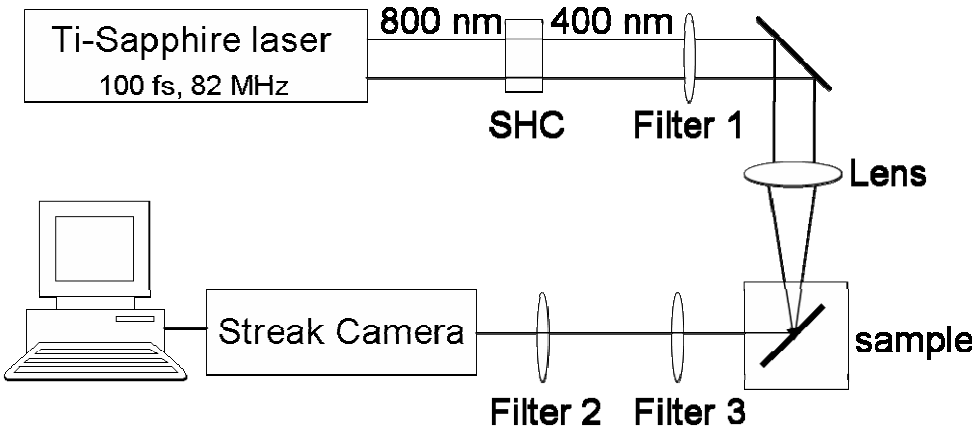

Figure 3.5 Schematic illustration of the time-resolved PL experimental setup.

In the time-resolved PL measurement, the PL intensity is observed as it decays as a function of time. From fitting of the decay curves, the value of the carrier recombination lifetime τ can be obtained and evaluated. The diagram of a time-resolved PL experimental setup is shown in Fig. 3.5. The sample is mounted

in a low temperature cryostat with a temperature control unit. The temperature dependent measurements can be performed from 78 K to 300K. The excitation source is the second harmonic radiation at 400 nm obtained from a mode-locked tunable Ti-sapphire laser (Spectra Physics Tsunami) by a second harmonic crystal (SHC). The laser pulses have a pulse width of 100 fs and a repetition rate of 82 MHz. The PL signal from the sample is focused and collected by a streak camera (Hamamatsu Model C5680) with a typical temporal resolution of 10 ps. A short-wavelength pass filter (filter 1) is used after the SHC to block the 800 nm laser beam and a long-wavelength pass filter (filter 2) is used in the front of the streak camera to block the 400 nm laser beam reflected by the samples. A band-pass filter (filter 3), with a FWHM of 10 nm, can be added to select the PL wavelength range of interest and follow the PL peak signal at various temperatures. The data is recorded by a computer which is connected to the streak camera.

3.4 Hall Effect measurement

For intersubband absorption studies, all the QW layers need to be doped n-type with a certain carrier concentration. The doping level is an important parameter for the design of the active region of ISB devices. Hall Effect is the most common method to measure the resistivity, mobility, carrier concentration and the carrier type in a doped sample.

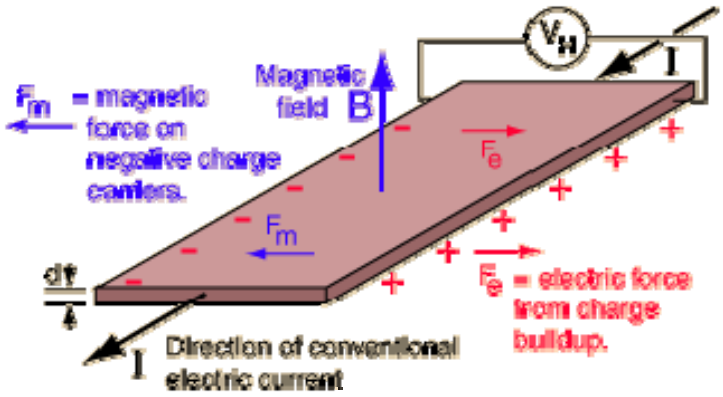

Figure 3.6 Schematic illustration of Hall Effect measurement.

If an electric current flows through a conductor in a magnetic field, the magnetic field exerts a transverse force (F_m), the Lorentz force $e v$ x B, on the moving charge carriers which tends to push them to one side of the conductor. This is most evident in a thin flat conductor as illustrated in Fig. 3. 6. A buildup of charge at the sides of the conductors will balance this magnetic influence, producing a measurable voltage, V_H, between the two sides of the conductor. The presence of this measurable transverse voltage is called the Hall Effect after E. H. Hall who discovered it in 1879.

The Hall voltage has a different polarity for positive and negative charge carriers, and it has been used to study the details of conduction in semiconductors and other materials which show a combination of negative and positive charge carriers. In this study, the samples were only doped n-type,

therefore the movement of negative charge carriers which are electrons will be discussed. In Fig. 3.6, the Lorentz force exerts an average leftward force on the electrons, and the leftward-directed movement causes a piling up of electrons on the left side of the sample, which in turn gives rise to an electric field F_e. Since there is no net current along this direction in the steady state, the electric field (Hall field) exactly balances the Lorentz force.

The relation between the Hall voltage (V_H) and applied current density (J) and magnetic field (B) can be expressed by[28]

$$V_H = R_H JB \tag{3.7}$$

where R_H is the Hall coefficient, which can be obtained from the given J and B and the measured V_H via Eq. (3.7).

When both holes and electrons are present in compensated samples, the expression that relates the free carriers and the Hall coefficient is given by[29]

$$R_H = r\frac{1}{q}\frac{(p-b^2n)+(\mu_n B)^2(p-n)}{(p+bn)^2+(\mu_n B)^2(p-n)}, \qquad b \equiv \mu_n / \mu_p \tag{3.8}$$

$$r \equiv \langle \tau^2 \rangle / \langle \tau \rangle^2 \tag{3.9}$$

where b is the mobility ratio, q is the elementary charge, and μ_n and μ_p are electron and hole mobilities, respectively. The parameter τ is the mean free time

between carrier collisions, which depends on the carrier energy, and r is the scattering factor that lies between 1 and 2, depending on the scattering mechanisms in the semiconductor. This expression reveals that the Hall coefficient varies with applied magnetic field. For samples with modest mobility in the 100 to 1000 cm^2/Vs and with mobility ratios of b ~ 3 to 10, R_H is generally found to vary little with magnetic field. [29] For the case of $\mu_n B$ << 1, Eq. (3.8) can be simplified to:

$$R_H = r\frac{1}{q}\frac{p - b^2 n}{(p + bn)^2}, \tag{3.10}$$

For highly doped samples without significant compensation effect (i.e. n >> p for n-type) and with modest mobility ratios, Eq. (3.8) can be simplified to:

$$R_H = r(\frac{-1}{qn}) \tag{3.11}$$

Usually, r is assumed to be unity and this assumption generally introduces an error of less than 30%.[29] Thus, the carrier concentration can be determined via Eq. (3.10). The carrier type in the sample can be determined from the sign of Hall coefficient; i. e. n-type if R_H is negative and p-type if R_H is positive.

Moreover, the Hall mobility μ_H can also be obtained by

$$\mu_H = |R_H| / \rho \tag{3.12}$$

where ρ is the resistivity of the sample which can be expressed by

$$\rho = \frac{1}{\sigma} = \frac{1}{q(\mu_n n + \mu_p p)}, \tag{3.13}$$

where σ is the conductivity. If n >> p, as in n-type semiconductors,

$$\rho \cong \frac{1}{q\mu_n n}. \tag{3.14}$$

The magnetic field (B) used for Hall Effect measurements in our laboratory is fixed at 2.5 kG (=0.25 T) and the samples studied have relatively low electron mobilities μ_n in the range of 100 cm^2/Vs. This results in $\mu_n B \sim 10^{-3} - 10^{-2} << 1$ and for highly n-type doped $Zn_xCd_{1-x}Se$ where n >> p, Eq. (3.11) can be used to determine the free carrier concentration (n).

In the following studies, Hall Effect measurements were used to measure the doping level in the reference samples, which were grown separately from the MQW structures. To measure the doping level within a complex structure, electrochemical capacitance-voltage measurements were performed, which gave the net (N_D-N_A) carrier concentration.

3.5 Electrochemical Capacitance-Voltage profiling

Electrochemical capacitance-voltage (ECV) profiling is a widespread metrology technique that offers a versatile and powerful approach to determining doping levels at various depths within a semiconductor structure. This technique, combining C-V and depth (etch) profiling, is based on making a liquid electrolyte-semiconductor Schottky contact and measuring the capacitance at a constant *dc* voltage. It has the capability to characterize the capacitance as a function of

depth into the sample structure in steps as small as 0.005 μm, that is, useful for the study of multiple layer structures. The etching profiling is achieved by electrolytically etching the semiconductor between C-V measurements.

3.6 Scanning Electron Microscopy

Electron microscopes (EM), which use beams of electrons instead of light, are designed for very high magnification usage. Based on DeBroglie hypothesis, electrons, which have a much smaller wavelength than visible light, allow a much higher resolution. After the first EM prototype was built in 1931 by the German engineers Ernst Ruska and Max Knoll, modern EMs can magnify objects up to millions of times, making them widely used in a wide range of research on examining biological materials, medical samples, metals and crystalline structures, and the characteristics of various surfaces. The main limitation of the electron beam is that it must pass through a vacuum as air molecules would otherwise scatter the beam. Scanning electron microscope (SEM) is a type of EM producing images by detecting secondary electrons which are emitted from the surface due to excitation by the primary electron beam. In the SEM, the electron beam is rastered across the sample, with detectors building up an image by mapping the detected signals with beam position. Because the SEM image relies on surface processes rather than transmission it is able to image bulk samples and has a much greater depth of view, and so can produce images that are a good representation of the 3D structure of the sample.

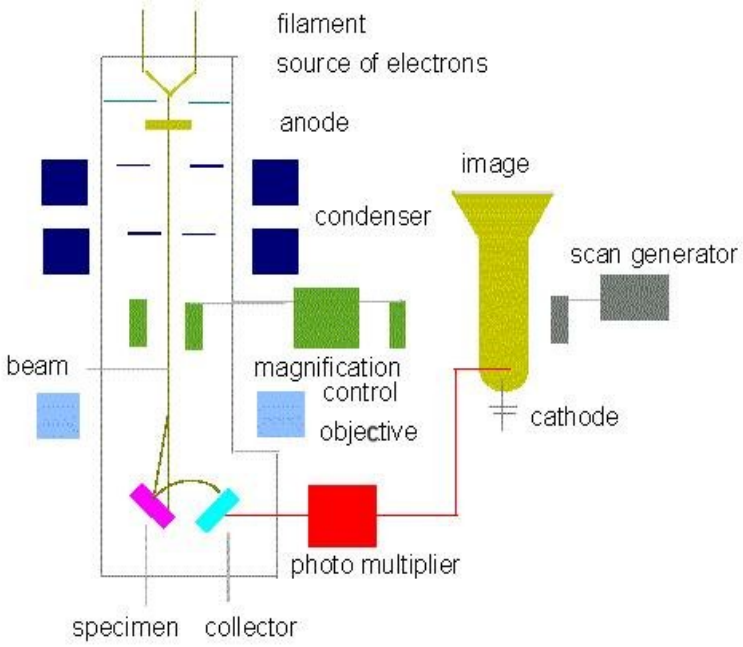

Figure 3.7 Schematic illustration of a SEM.

As shown in Fig. 3.7, in a typical SEM electrons are thermionically emitted from a tungsten or lanthanum hexaboride (LaB_6) cathode and are accelerated towards an anode; alternatively electrons can be emitted via field emission. Tungsten is used because it has the highest melting point and lowest vapor pressure of all metals, thereby allowing it to be heated for electron emission. The electron beam, which typically has an energy ranging from a few hundreds to 50 keV, is focused by one or two condenser lenses into a beam with a very fine focal spot sized 1 nm to 5 nm. The beam passes through pairs of scanning coils in the objective lens, which deflect the beam in a raster fashion over a rectangular area of the sample surface. Through these scattering events, the primary electron beam effectively spreads and fills a teardrop-shaped volume, known as the

interaction volume, extending from less than 100 nm to around 5 μm into the surface. Interactions in this region lead to the subsequent emission of electrons which are then detected to produce an image. X-rays, which are also produced by the interaction of electrons with the sample, may also be detected in an SEM equipped for energy-dispersive X-ray spectroscopy or wavelength dispersive X-ray spectroscopy.

In this work, SEM will be used to produce images on cross-sectional edges of the MQWs region for studying the structural and interfacial properties.

3.7 Contactless Electroreflectance

In order to investigate the quantum well transitions we have used contactless electroreflectance (CER) spectroscopy. This technique, which is similar to photoreflectance (PR) spectroscopy, is an excellent tool to investigate both the fundamental and higher order QW transitions. Moreover, CER has a number of advantages over PR for the study of QW structures. CER does not require a laser as the pump beam and avoids the photoluminescence background due to this pump beam. Also, CER spectra are free of below band gap oscillation features, which are often observed in PR spectra, especially for GaAs-based structures grown on n-type GaAs substrates. The analysis of CER data together with theoretical calculations makes it possible to determine material parameters such as the band gap discontinuity. Such procedures have been often applied in studies for different semiconductor structures.

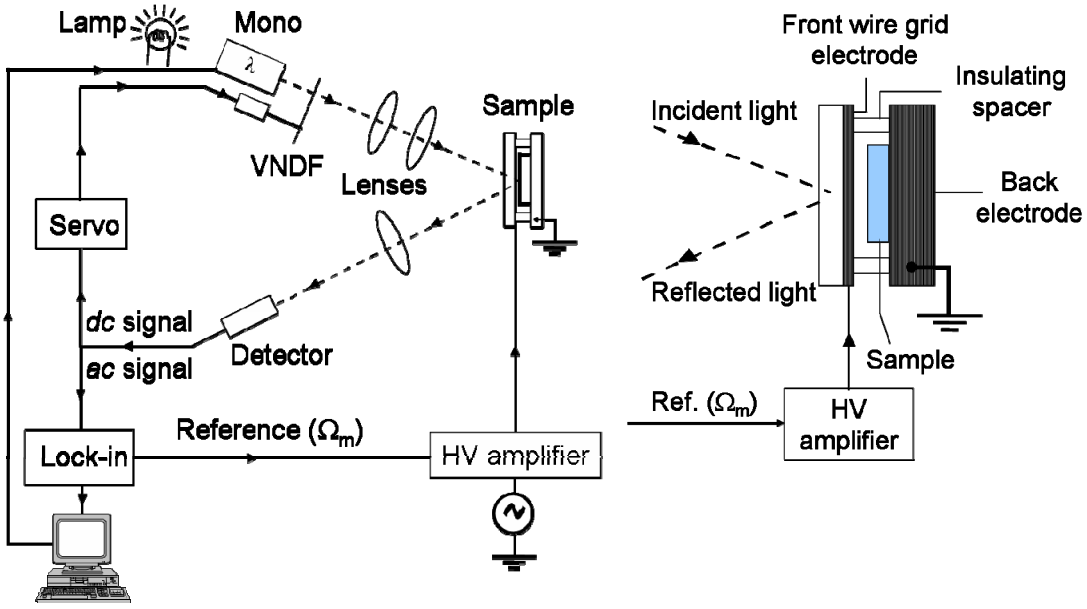

Figure 3.8 (a) Schematic illustration of CER setup and (b) the details of the sample holder showing the contactless mechanism.

Shown in Fig. 3.8 (a) is a schematic drawing of the experimental arrangement for a CER experiment in our lab. Light from an appropriate source, a 150 W Xenon-arc or tungsten-halogen lamp, passes through a monochromator. The exit intensity at wavelength λ, $I_0(\lambda)$, is adjusted by a variable neutral density filter (VNDF) then focused onto the sample by means of a set of lenses. The sample is mounted on a condenser-like system (see Fig. 3.8 (b)) consisting of a front wire grid electrode with a second metal electrode separated from the first electrode by insulating spacers. The dimensions of the spacer are such that there is a very thin layer (~0.1 mm) of air between the front surface of the sample and

the wire grid of the first electrode. Electromodulation is a particularly useful form of modulation spectroscopy since it often yields the sharpest structure and is sensitive to surface or interface electric fields. In the experiment, the electric field modulation, an *ac* voltage (~1 kV peak to peak) is generated by a Trek 609E-6 HV amplifier and applied between the two electrodes at frequency Ω_m. The reflected light from the sample is collected by another lens and is focused onto a Si photodetector. An oscilloscope is used to monitor the performance of the high voltage during the measurement.

The light striking the detector contains both *dc* and *ac* signals: the *dc* signals given by $I_0(\lambda)R(\lambda)$, where $R(\lambda)$ is the *dc* reflectance of the material while the modulated (*ac*) signal (at frequency Ω_m) is $I_0(\lambda)\Delta R(\lambda)$, where $\Delta R(\lambda)$ is the change in reflectance produced by the modulation source. The *ac* signal from the detector, proportional to $I_0(\lambda)\Delta R(\lambda)$, is measured by a lock-in amplifier. Typically $I_0\Delta R$ is 10^{-4} to 10^{-6} of I_0R. In order to evaluate the quantity of interest, i.e., the relative change in reflectance $\Delta R/R$, a normalization procedure must be used to eliminate the uninteresting common feature $I_0(\lambda)$. In Fig. 3.8 (a) the normalization is performed by the VNDF connected to a servo mechanism. The *dc* signal from the detector, which is proportional to $I_0(\lambda)R(\lambda)$, is fed into the servo which moves the VNDF in such a manner as to maintain a constant $I_0(\lambda)R(\lambda)$, i. e., $I_0(\lambda)R(\lambda) = C$. Under these conditions the *ac* signal $I_0(\lambda)\Delta R(\lambda) = C\Delta R(\lambda)/R(\lambda)$. Subsequently, the signal to the lock-in amplifier is proportional to the quantity of interest, i.e.,

$\Delta R(\lambda)/R(\lambda)$. Thus, the CER spectrum gives very sharp derivative-like features corresponding to specific transitions, while typical reflectivity is characterized by broad features.

3.8 Fourier Transform Infrared Spectroscopy

Since our interest of study is infrared devices, Fourier transform infrared (FTIR) spectroscopy is employed to characterize the sample's properties in the mid-IR range. Fourier transform (FT) spectroscopy is a measurement technique whereby spectra are collected based on measurements of the temporal coherence of a radiative source. It can be applied to variety of types of spectroscopy including optical spectroscopy, infrared spectroscopy (FTIR), nuclear magnetic resonance, and electron spin resonance spectroscopy.

Unlike most of the spectroscopy techniques, FT-IR uses a Michelson interferometer replacing the dispersive grating spectrometer, as the wavelength selector. This gives the Fourier transform of the desired spectrum, known as the "interferogram", which requires extensive computer manipulation to yield the desired intensity versus wave-number spectrum. Figure 3.9 illustrates how Michelson interferometer works. When the radiation leaves the source and reaches the beam splitter (BS), part of the beam passes through the BS and is reflected from the stationary mirror (M1), whereas another part is reflected from the BS and then from a moving mirror (M2). As M2 moves, it changes the difference in length Δ between the paths the two light beams traverse. When the

beams recombine they produce an intensity which depends on Δ, called the interferogram $I(\Delta)$. Except for a constant multiplicative factor, the interferogram is given by:[30]

$$I(\Delta) = \int_{-\infty}^{\infty} S(f)[1 + \cos(2\pi \cdot f\Delta)]df = \frac{1}{2} I(0) + \int_{-\infty}^{\infty} S(f)\cos(2\pi \cdot f\Delta)df \qquad (3.15)$$

where $S(f)$ is the intensity spectrum of the source, f is the optical frequency in wave-numbers, and $I(0)$ is the intensity at zero path difference. The integral in Eq. (3.15) is the cosine Fourier transform of $S(f)$, which can be recovered by carrying out the inverse Fourier transform (also to within a constant factor):

$$S(f) = \int_{-\infty}^{\infty} [I(\Delta) - \frac{1}{2} I(0)]\cos(2\pi \cdot f\Delta)d\Delta \qquad (3.16)$$

This is implemented by measuring the interference signal $I(\Delta)$ with a detector, whose output is then processed by a computer.

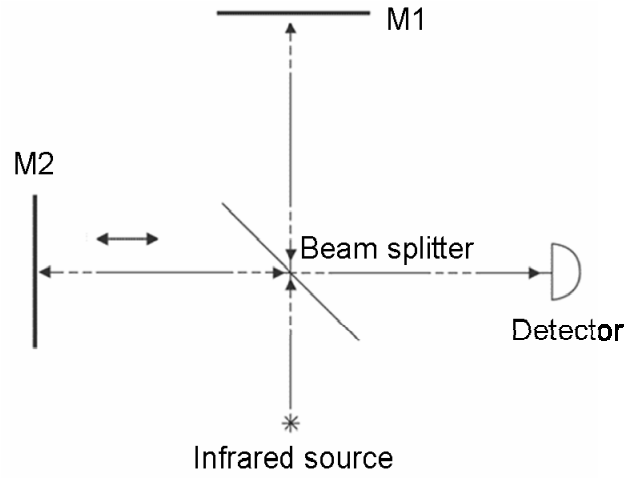

Figure 3.9 Schematic diagram of a Michelson interferometer.

As shown in Fig. 3.9, a FTIR spectrometer obtains infrared spectra by first collecting an interferogram of a sample signal with an interferometer, which measures all of infrared frequencies simultaneously. An FTIR spectrometer

acquires and digitizes the interferogram, performs the FT function (by computation), and outputs the spectrum. Consequently, a transmittance spectrum is obtained as follows.

$$T\% = \frac{I}{I_0} \tag{3.17}$$

where $T\%$ is transmittance; I is the intensity measured with a sample in the beam (from the sample single beam spectrum); I_0 is the intensity measured from the back ground spectrum. The absorbance spectrum can be calculated from the transmittance spectrum using the following equation.

$$A = -\log_{10} T \tag{3.18}$$

where A is the absorbance.

The Fourier method gives a much higher signal-to-noise ratio than does grating spectroscopy. One reason is that many wavelengths are measured simultaneously in Fourier spectroscopy, while in dispersive spectroscopy, there is only one wavelength measured at a time. The other reason is that high resolution can be attained in FTIR spectroscopy without using narrow slits, whereas in conventional spectroscopy there is always a trade-off between resolution and the amount of light reaching the samples.

Even with the signal-to-noise advantages of FTIR spectroscopy, sensitive

detectors are important. In the mid-IR, mercury cadmium telluride (MCT) photovoltaic or photoconductive detectors give good sensitivity when operated at liquid nitrogen (LN_2) temperatures.

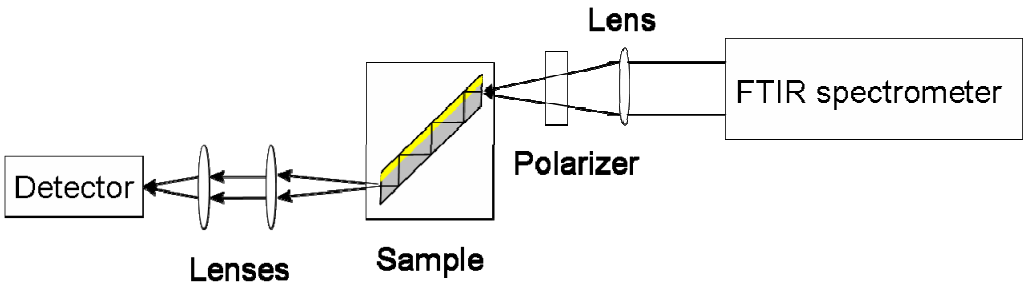

Figure 3.10 Schematic diagram of the FTIR system used for our intersubband absorption measurement. The sample size is enlarged for a clear view of the light traveling inside the sample.

Although there is a variety of commercial FTIR instruments available, users may need to add or fabricate additional optical elements depending on the wavelength range to be covered and different studies purpose. For our ISB absorption studies, the geometry of modified FTIR system is shown in Fig. 3.10. In the system, all the optical parts, including the lens and the widows on the cryostat where the sample is mounted, are made of zinc selenide (ZnSe) with a remarkable wide transmission wavelength range from 0.6 to 20 μm.

Chapter 4

Band offset determination of the $Zn_xCd_{1-x}Se/Zn_{x'}Cd_{y'}Mg_{1-x'-y'}Se$ material system

The growing interest in quantum cascade lasers[31] (QCLs) and other devices based on intersubband (ISB) transitions, emphasizes the need to research relevant fundamental parameters of heterostructures such as the band offsets. Considerable advances have been achieved in the development of the QCLs, however, there are still many limitations, one of which is the absence of QCLs operating at short wavelengths, such as λ = 3 μm, a useful light source for trace-gas detection in the environment or atmosphere. The limitation is related to the relative small conduction band discontinuity present in the most frequently used heterostructure systems based on GaAs and InP. In order to overcome these limitations, the study of ISB transitions has been recently extended to other systems with larger band discontinuity such as GaN[32,33], and II-VI compounds[34-37]. Other than offering a shorter wavelength operation of ISB devices, the large CBO also improves the thermal performance of ISB devices operating at other current wavelengths (i.e. a higher temperature can be achieved for continuous wave operation). Among the most relevant parameters for the ISB devices are the band offsets. As we mentioned before, the wide bandgap II-VI alloy system $Zn_xCd_{1-x}Se/Zn_{x'}Cd_{y'}Mg_{1-x'-y'}Se$ that is lattice-matched to InP possesses a range of

bandgaps between 2.1 and 3.3 eV, thus, due to the common anion ion rule, large conduction band offsets (CBO) are expected. In this chapter, we measured the band-to-band transitions of a representative $Zn_{0.53}Cd_{0.47}Se/Zn_{0.27}Cd_{0.23}Mg_{0.50}Se$ single quantum well (QW) structure using contactless electroreflectance (CER) at RT. By comparison with the predicted values from the theoretical calculation based on the envelope function approximation (EPA) [38,39], we determined the CBO of this structure. The result suggests a potential interest of this system for ISB devices and is very useful in guiding the device structure design.

4.1 Theoretical background

Due to the increasing interest in quantum electronic devices based on semiconductor nanostructures, a theoretical method to understand and to predict the physical properties of such devices, providing efficient and reliable computations of their electronic states is required. The envelope function approximation (EFA) is a valuable tool for calculating and understanding the electronic energy levels in semiconductor heterostructures because it provides a high degree of physical insight at a low computational cost. It has been used widely in different semiconductor heterostructures[40,41,42] and has been proven efficient compared with more sophisticated approaches.[43,44]

The II-VI heterostructure $Zn_xCd_{1-x}Se/Zn_{x'}Cd_{y'}Mg_{1-x'-y'}Se$ can be grown lattice-matched to InP substrates with a type-I alignment. Only the simplest

structure, a rectangular single QW (see Fig. 4.1), will be studied and discussed. The materials labeled A and B represent the QW layer and barrier layers in the semiconductor heterostructures, with ϵ_A and ϵ_B denoting their bandgap energies, respectively. The growth direction will be taken as the *z* axis. To simplify the calculation, in the following discussion we assume it is a strain-free structure that does not contain free carriers. As we will discuss later, the strain only affects significantly the transitions related to light holes, while it affects only slightly the transitions related to heavy holes.

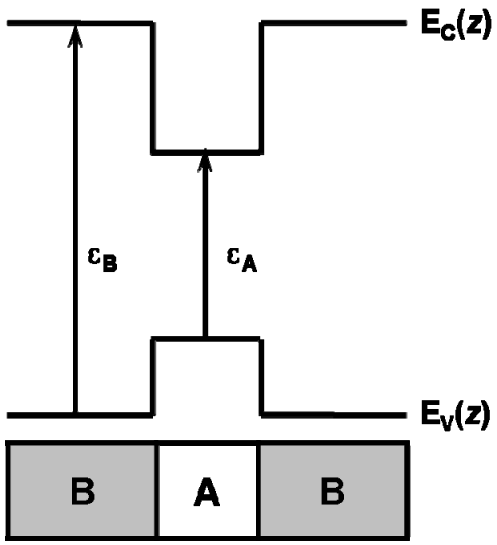

Figure 4.1 Illustration of the band structure and layer structure of a rectangular QW well that consists of two semiconductors A and B with ϵ_A and ϵ_B as the bandgap energy, respectively. Both electrons and holes are essentially confined in A layer (type I alignment). The growth direction is indicated by the *z* axis.

4.1.1 Envelope function approximation

In the semiconductor heterostructure, each material has its own lattice constant, and band structure characterized by dispersion relations $\varepsilon_n^{(A)}(\vec{k}_A)$, $\varepsilon_n^{(B)}(\vec{k}_B)$ and Bloch functions $\psi_{n\vec{k}_A}^{(A)}(\vec{r})$, $\psi_{n\vec{k}_B}^{(B)}(\vec{r})$. For allowed energies, $\varepsilon_{n\vec{k}_A}^{(A)}(\vec{r})$ the wave functions $\psi_{n\vec{k}_A}^{(A)}(\vec{r})$, $\psi_{n\vec{k}_B}^{(B)}(\vec{r})$ display the familiar form

$$\psi_{n\vec{k}_A}^{(A)}(\vec{r}) = \Omega^{-1/2} u_{n\vec{k}_A}(\vec{r}) \exp[i\vec{k}_A \cdot \vec{r}] \tag{4.1}$$

where $u_{n\vec{k}_A}$ is a periodic function (Bloch envelope) and $\vec{k}_A$ is a real wave vector that can be restricted to the first Brillouin zone of the material A. An expression for the material B is similar to Eq. (4.1).

The envelope function scheme takes advantage of two considerations.

a) Most of the materials in one structure display similar band structures. Moreover, the periodic parts of the Bloch functions of the relevant band edges do not differ very much from one material to the other.

b) The relevant electronic states of the actual heterostructures are often close from the band extrema of the materials in the structure. Thus, only a small fraction of the Brillouin zone (of layer A or B) participates in the building of the heterostructure states.

In addition, we shall assume that the materials are lattice-matched. The case of strained layer materials is more complicated and will not be discussed here.

For a perfect heterostructure under flat band conditions, the wave function

$\psi^{A,B}(\vec{r})$ in the A and B layers can be expanded as

$$\psi^{A,B}(\vec{r}) = \sum c_n^{(A,B)}(\vec{k}_\perp, k_z^{(A,B)}) u_{n0}^{(A,B)}(\vec{r}) \cdot \exp[i\vec{k}_\perp \cdot \vec{r}_\perp + ik_z^{(A,B)} z]. \quad (4.2)$$

In Eq. (4.2) $\vec{k}_\perp = (k_x, k_y)$ and $\vec{r}_\perp = (x, y)$ are bi-dimensional wave and position vectors, respectively, and n is a bulk band index which runs over the layer material band edges that one decides to retain in the expansion. The wave function $\psi^{(A,B)}(\vec{r})$ is the sum of products of the slowly varying band edge periodic functions (the $u_{n0}(\vec{r})$ in Eq. (4.2)), by the plane waves (the exponential part $\exp[i\vec{k}_\perp \cdot \vec{r}_\perp + ik_z^{(A,B)} z$ in Eq. (4.2)).

The energy $\boldsymbol{\epsilon}$ of the electronic state under consideration is related to $\vec{k}_\perp$, $k_z^{(A)}$, $k_z^{(B)}$ by the two relations

$$\varepsilon = \varepsilon(\vec{k}_\perp, k_Z^{(A)}); \qquad \varepsilon = \varepsilon(\vec{k}_\perp, k_Z^{(B)}). \quad (4.3)$$

Let us take the A material as a reference for the energy scale. Then, $\boldsymbol{\epsilon}$ and $\vec{k}_\perp$, $k_Z^{(A)}$ are related by means of the dispersion relations of the bulk A layer. A crucial point in evaluating $k_Z^{(B)}$ is the band lineups of the A and B materials at the heterointerface. Since the bandgaps of materials A and B are known, a single band offset remains undetermined, i.e., the conduction band offset ΔE_C. The band lineups sensitively influence the energy level pattern in the heterostructure. This, in turn, may drastically affect device performance. Thus, one of the first experimental tasks when studying a heterostructure is to determine the band lineups. Studies have been performed on the zinc-blende heterostructure $Zn_xCd_{1-x}Se/Zn_{x'}Cd_{y'}Mg_{1-x'-y'}Se$ and a type I alignment has been proven as shown in Fig.

4.1.

The envelope functions are the eigenfunctions of matrix-valued $k \cdot p$ Schrödinger operators with discontinuous coefficients. Usually $k \cdot p$ Schrödinger operators are constructed by a physical transfer of the $k \cdot p$ theory for bulk materials to nanostructures. Considering the nonparabolicity of the bands and neglecting inversion-asymmetry splitting, the bulk Hamiltonian in each layer can be written in the form of an 8 X 8 matrix[65]

$$\sum_{\alpha,\beta} k_\alpha D_{jj'}^{\alpha\beta} k_\beta + \sum_\alpha \frac{\hbar k_\alpha}{m_0} \langle j | p_\alpha | j' \rangle \tag{4.4}$$

where 1 ≤ j, j' ≤ 8, α, β = x, y, z and

$$D_{jj'}^{\alpha\beta} = \frac{\hbar^2}{2m_0} \delta_{jj'} \delta_{\alpha\beta} . \tag{4.5}$$

In Eq. (4.4) and (4.5), m_0 is the free electron mass. $\langle j | \vec{p} | j' \rangle$ is the $\vec{p}$ matrix element between the band edge (k = 0) Bloch functions of the jth and j'th edge. The Hamiltonian of the heterostructure can be simply obtained from the bulk Hamiltonian (Eq. (4.4)) by neglecting possible band bending:

$$\left\{ D\left[\gamma_i(z), -i\frac{\partial}{\partial z}, \vec{k}_\perp \right] \right\} \vec{f}(z) = \varepsilon \vec{f}(z) \tag{4.6}$$

where D is the 8 X 8 differential system involving the bulk constants $\gamma_i(z)$ (γ_i is a shorthand notation for all the effective parameters appearing in Eq. (4.4)). $\vec{f}(z)$ is the eigenfuction (envelope function) and the eigenvalues obtained from Eq. (4.6) are the electronic energy levels in the heterostructure.

4.1.2 Energy levels in type I quantum wells ($k_\perp$ = 0)

Type I systems are defined as heterostructures in which conduction and valence electrons are (essentially) confined within the same kind of layers (A layers). Many heterostructures display the type I configuration: GaAs/$Ga_{1-x}Al_xAs$, $Ga_{1-x}In_xAs/Al_{1-x}In_xAs$, GaSb/AlSb, $Zn_xCd_{1-x}Se/Zn_{x'}Cd_{y'}Mg_{1-x'-y'}Se$, etc.

Since we assume $\vec{k}_\perp = \vec{0}$ and neglect the inversion asymmetry splitting, the heavy hole and light hole spectra decouple. The heavy hole levels are the solutions of a Ben Daniel-Duke Hamiltonian[45] whereas the light hole levels are obtained by solving a Kane-type [46] Hamiltonian suitably generalized to heterostructures. The latter reduces to the former when the band nonparabolicity is small enough.

1) Heavy hole levels ($\vec{k}_\perp = \vec{0}$)

For hole levels we have to solve a Ben Daniel-Duke Hamiltonian, which is of the form

$$\left\{-\frac{h^2}{2}\frac{\partial}{\partial z}\frac{1}{M_{hh}(z)}\frac{\partial}{\partial z} - V_p(z)\right\} f_{hh}(z) = \varepsilon f_{hh}(z) \tag{4.7}$$

where $V_p(z)$ is the valence band offset.

The boundary conditions are that $f_{hh}(z)$ and $M_{hh}^{-1}(z)$ (df_{hh}/dz) are both continuous at the interfaces ($z = \pm L/2$, where L is the quantum well thickness). The f_{hh}'s can be chosen either odd or even in z. For even (odd) states, the bound states equations are, respectively,

$$\frac{k_w}{M_{hh}^{(A)}}\tan\left(k_w\frac{L}{2}\right)=\frac{k_b}{M_{hh}^{(B)}};\qquad \frac{k_w}{M_{hh}^{(A)}}\cot\left(k_w\frac{L}{2}\right)=-\frac{k_b}{M_{hh}^{(B)}} \tag{4.8}$$

where k_w and k_b are the Bloch wave vector of QW and barrier

$$k_w=\sqrt{\frac{2M_{hh}^{(A)}\varepsilon}{h^2}};\qquad k_b=\sqrt{\frac{2M_{hh}^{(B)}(-V_p-\varepsilon)}{h^2}}. \tag{4.9}$$

A one-dimensional quantum well always admits one bound state. Moreover, the nth bound state (n = 1, 2, …) pops out of the well (ε = -V_p) when

$$k_w(\varepsilon_n=-V_p)=(n-1)\pi/L. \tag{4.10}$$

2) Light hole levels ($\vec{k}_\perp=\vec{0}$)

The Kane[46] dispersion relations on bulk materials can be written as:

$$\varepsilon(k_A)=\frac{h^2k_A^2}{2m_A(\varepsilon)}. \tag{4.11}$$

The carrier effective mass increases when its energy departs from the band edges, a phenomenon referred to as band nonparabolicity, which is considered for the wide bandgap II-VI materials.

The quantum well with band nonparabolicity is solved as

$$\tan(\frac{1}{2}k_AL)=\xi^{-1};\qquad \cot(\frac{1}{2}k_AL)=-\xi^{-1} \tag{4.12}$$

where

$$\xi=\frac{k_A(\varepsilon)}{k_B(\varepsilon)}\times\frac{m_B(\varepsilon)}{m_A(\varepsilon)} \tag{4.13}$$

Interestingly, Eq. (4.12), (4.13) have exactly the same form as (4.8). Indeed, when the nonparabolicity becomes weak (i.e., $\varepsilon<<\varepsilon_g^{(A)},\varepsilon_g^{(B)}$) the Kane dispersion relations includes the Ben Daniel-Duke Hamiltonian as a limiting case.

4.1.3. Common anion rule

It is known[47] that the zone-center valence band maximum (VBM) in a binary zinc-blende semiconductor consists almost exclusively of anion valence *p* orbits while the conduction band minimum (CBM) consists almost exclusively of cation valence *s* orbits. It was therefore initially expected[48,49,50] that the VBM energies of two common anion semiconductors which share the same crystal structure and lattice constant would be nearly equal. Then the “common anion rule” was formulated based on these expectations. The “common anion rule” states that the offset ΔE_{VBM} between the VBM energies of two covalent semiconductors reflects primarily different anion energies, and hence would nearly vanish for semiconductors sharing a common anion. (While “common-cation rule” states that the offset ΔE_{CBM} between the CBM energies of two covalent semiconductors reflects primarily different cation energies, and hence would nearly vanish for semiconductors sharing a common cation.) Therefore, the most band discontinuity in the heterostructure made of these two semiconductors will appear in the conduction band, while it should be relatively small in the valence band.

In the following, the experimental part of the study on a single quantum well structure of $Zn_{0.53}Cd_{0.47}Se$/ $Zn_{0.29}Cd_{0.24}Mg_{0.47}Se$ will be discussed.

4.2 MBE growth

The sample was prepared by molecular beam epitaxy (MBE) using the

optimized growth procedure and conditions described in Chapter 2. An InGaAs buffer layer (~0.1μm), lattice matched to InP, was grown with an As-terminated surface having a (2×4) surface reconstruction. The substrate was transferred to the II–VI chamber to perform Zn-irradiation for 40 seconds before II–VI material deposition. Then a ZnCdSe interfacial layer (~70 Å) was grown at low temperature (170 °C) during approximately 1 min. Growth was interrupted for about 4 min to smooth the growth front and to adjust the temperature to the optimum growth temperature of 270°C, at which point the desired $Zn_xCd_{1-x}Se/Zn_{x'}Cd_{y'}Mg_{1-x'-y'}Se$ single quantum well structure was grown. A 0.5 μm thick $Zn_{0.29}Cd_{0.24}Mg_{0.47}Se$ (E_0 = 2.8 eV at room temperature) barrier layer was grown, followed by the $Zn_{0.53}Cd_{0.47}Se$ QW layer, with a nominal thickness of 50 Å. Then, a 0.1 μm thick $Zn_{0.29}Cd_{0.24}Mg_{0.47}Se$ top barrier layer was grown. The structure was capped by a 70 Å thick pseudomorphic ZnCdSe cap layer to protect the $Zn_{0.29}Cd_{0.24}Mg_{0.47}Se$ from oxidation by atmospheric oxygen. The growth rate of the quaternary and ternary layers was 0.9 μm and 0.4 μm per hour, respectively. The beam equivalent pressure ratio VI/II was about 3. These nominal thicknesses were calculated using thick-calibration samples grown during the same run.

4.3 Sample quality

X-ray diffraction (XRD) and Photoluminescence (PL) measurements were used to characterize the sample quality. Shown in Fig. 4.2 is the double crystal

XRD rocking curve of the sample. A clear ZnCdMgSe peak with the FWHM of 50 arcsec is observed, indicating the quaternary alloy is almost lattice matched ($\Delta a/a$ = 0.05%) to the substrate with excellent material quality. The QW layer was also nearly lattice matched to InP, with $\Delta a/a$ = 0.1%, determined on a thick ZnCdSe sample grown during the same run.

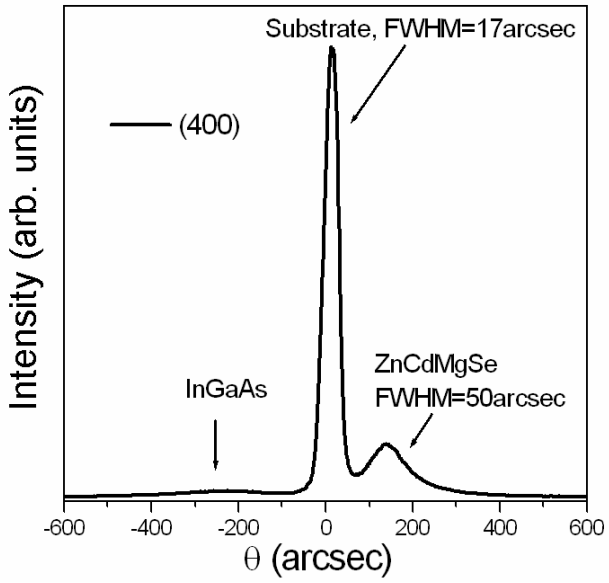

Figure 4.2 Double crystal X-ray diffraction rocking curve of the single QW structure. The FWHMs are 17 arcsec and 50 arcsec for InP substrate and ZnCdMgSe layer, respectively.

The QW structure was characterized by PL measurements using the 325 nm line of a He-Cd laser for excitation. Strong and sharp PL emission was observed as shown in Fig. 4.3. The QW luminescence peaks were observed at 2.24 eV (FWHM = 26 meV) and 2.16 eV (FWHM = 45 meV) at 77 and room temperature, respectively, while the luminescence peak for the barrier was at

2.87 eV (FWHM = 73 meV) at 77K. At RT the barrier signal was quenched and we were not able to observe its PL signal.

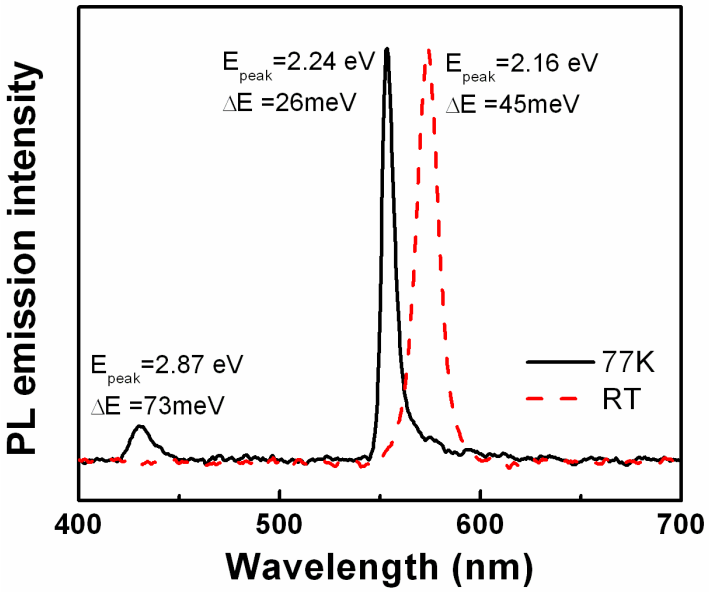

Figure 4.3 PL spectra of the single QW measured at 77K (solid line) and room temperature (dashed line). The FWHMs are 26 meV and 45 meV for 77K and RT, respectively.

4.4 Conduction band offset determination

4.4.1 Contactless electroreflectance measurement

To determine the CBO of the sample, CER is used together with a theoretical calculation based on the EFA. The interband transitions in this structure were determined using CER, which is a modulated technique[51, 52] that measures the changes in the optical reflectance of the material with respect to a

modulating electric field. This procedure gives rise to sharp, differential-like spectra in the region of the transitions. CER utilizes a condenser-like system[53] consisting of a front wire grid electrode with a second metal electrode separated from the first electrode by insulating spacers. The dimensions of the spacer are such that there is a very thin layer (~ 0.1 mm) of air (or vacuum) between the front surface of the sample and the wire grid of the first electrode. Thus, there is nothing in direct contact with the front surface of the sample. The sample was placed between these two capacitor plates and the electromodulation was achieved by applying an *ac* voltage of 1.2kV (peak-to-peak), 200 Hz across the electrodes.

The CER measurements were taken from 2.0 eV to 3.0 eV at room temperature using the light from a 150 W Xenon-arc lamp. The solid line in Fig. 4.4 is the measured RT CER spectrum. The energies corresponding to the transitions observed were obtained using a fit, shown by the dashed line, based on the first derivative of a Gaussian lineshape[51,54]. The values obtained from this fit are indicated by arrows in the figure and presented in Table I. The notation EnH(L)m in Fig. 4.4 indicates that the transitions are from the nth conduction subband to the mth valence subband of heavy (H) or light (L) hole character, respectively. All the interband transitions obtained from the CER measurement are presented in the band structure shown in Fig. 4.5.

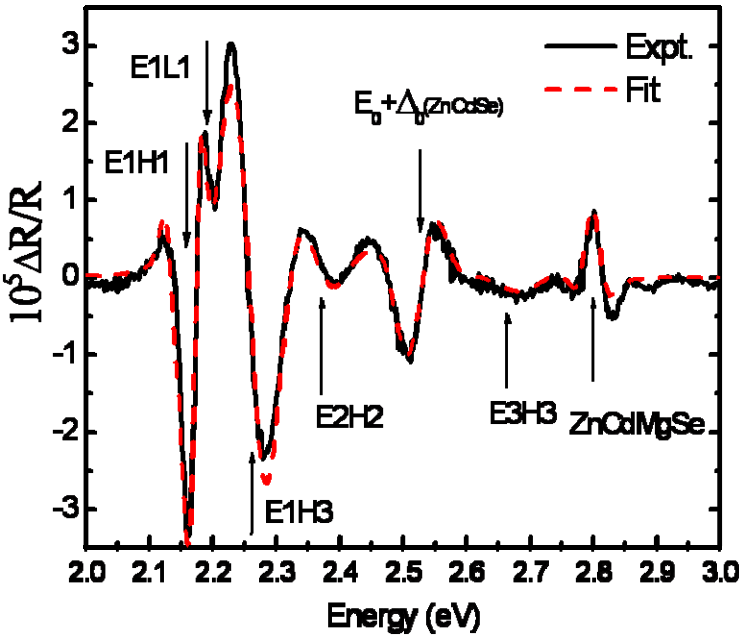

Figure 4.4 The solid line represents the experimental ΔR/R spectra. The dashed line is a fit yielding the energies indicated by the arrows.

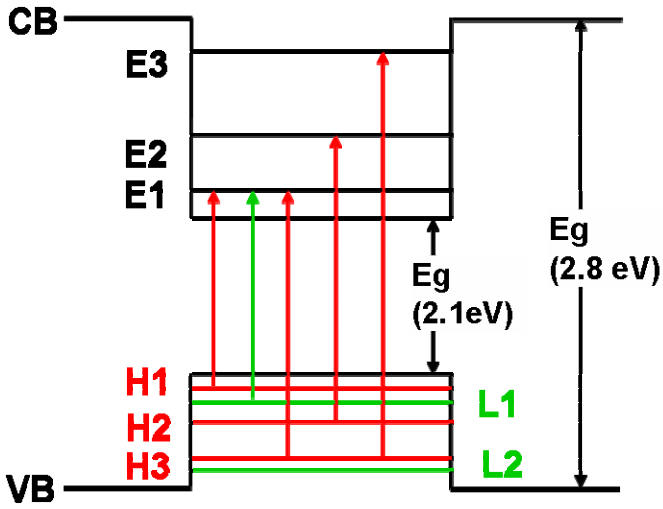

Figure 4.5 Band structure of the studied single QW with all the interband transitions obtained from CER indicated.

Table I. Experimental and calculated interband energies.

Transition	Experiment (eV)	Calculated (eV)
E1H1	2.159±0.005	2.158
E1L1	2.192±0.005	2.180[a]
		2.185[b]
E1H3	2.259±0.005	2.261
E2H2	2.369±0.005	2.371
E3H3	2.660±0.005	2.664
$E_0 + \Delta_0$	2.525±0.005	2.522[c]
E_0 (Barrier)	2.800±0.005	

[a] Calculation without considering the compressive strain.

[b] Calculation considering the compressive strain.

[c] Calculated using Δ_0 of Ref. 55 and our value of E_0.

Assignment of the transitions was done according to following considerations. The identification of the signal from the barrier at 2.8 eV was straightforward when we considered the 77K PL signal at 2.87 eV and its thermal energy shift. The intensities of the transitions at 2.159 eV and 2.192 eV exhibit a ratio close to three suggesting that they are associated with the heavy and light hole transitions, respectively[51,54]. The band gap of the $Zn_{0.53}Cd_{0.47}Se$ was

determined by CER measurements on a thick sample grown during the same run. The value that we found was E_0 = 2.080±0.005eV, in good agreement with reference [55], which reported E_0 = 2.078±0.002 and spin-orbit splitting Δ_0 = 0.442±0.02eV. Using our value for the band gap and this value for Δ_0 we obtain $E_0+\Delta_0$ = 2.522eV, which agrees well with the experimental value of Table I.

4.4.2 Effective masses

In order to calculate the energies corresponding to the observed transitions we have performed a calculation based on the envelope function approximation (EFA), which considers the nonparabolicity of the bands. In these calculations it is necessary to know the values of the effective masses as well as Δ_0. However there are no reports for the effective masses of these compounds. In order to approximate the required masses we followed two steps: first, for ZnSe, we took the average value between the maximum and minimum reported values, shown in Table II, while for MgSe and CdSe the data was taken from refs. 56 and 57, respectively. We did not find any report for the value of the effective mass of the light hole of CdSe, so observing that the electron and heavy hole masses for CdSe are approximately two thirds of those corresponding to ZnSe we assumed that this proportion is valid for the light hole masses, too. Then we set m_{lh}(CdSe)=2/3 m_{lh}(ZnSe). Secondly, using these values for the binaries and a weighted composition average we obtained the corresponding values for our

compounds, also shown in Table II.

Table II. Values of the parameters used in the calculation.

Parameter	ZnSe	CdSe	MgSe	$Zn_{0.27}Cd_{0.23}Mg_{0.50}Se$	$Zn_{0.53}Cd_{0.47}Se$
E_0 (eV)				2.800[a]	2.080[a]
m_e	0.15[b]	0.11[c]	0.23[d]	0.18	0.13
m_{hh}	0.66[b]	0.44[c]	0.78[d]	0.67	0.56
m_{lh}	0.145	0.09	0.33[d]	0.22	0.11
Δ_0 (eV)	0.43[e]	0.42[e]	0.40[d]	0.414[f]	0.442[a]
QW width (Å)	50 (Experimental)			51.9 (Calculated)	
$Q_c = \Delta E_c / \Delta E_0$	0.82±0.002				

[a] Experimental value.

[b] Average of the maximum and minimum values obtained from Ref. [57].

[c] Reference 57.

[d] Reference 56.

[e] Reference [58].

[f] Interpolated value using the binary values.

4.4.3 Conduction band offset (Q_C)

With the effective masses listed in Table II, we calculated the energies of the different transitions as a function of the parameter $Q_C = \Delta E_C / \Delta E_0$. Figure 4.6 shows the results of this strain-free calculation in solid lines for the transitions that fit better the experimental values of the transitions, represented by the horizontal dashed lines. These transitions correspond to the symmetry allowed ($n = m$) and symmetry forbidden but parity allowed ($n = m \pm 2,4,\ldots$) transitions. As indicated in Fig. 4.6 by the dotted vertical line, the best agreement between the calculated and the experimental values for all the observed transitions was found for $Q_c = 0.82 \pm 0.02$ ($\Delta E_c = 590$meV). As shown from Figs. 4.4 and 4.6, and Table I, there is very good overall agreement. There is only a small discrepancy in the E1L1 transition, which we attribute to the facts that the light hole mass of CdSe estimation may not be very accurate and that the small strain present in this structure shifts the calculated E1L1 transition. In order to estimate the band gap changes in ZnCdSe due to the strain present in this structure we followed reference 59, which provides the expressions that describe the bandgap changes as a function of the elastic constants C_{11}, C_{12} and deformation potentials a and b. The required constants and deformation potentials for this calculation were obtained from references 59-61. This calculations show that the heavy and light hole band gaps are changed by 2 meV, and 5 meV. The change for the heavy

hole band gap is smaller than the experimental error and therefore can be disregarded. However the change for the light hole gap is equal to the experimental error and must be added (since the QW is under compressive strain) to the energy of the transition E1L1 previously calculated, obtaining a better agreement with the experimental results.

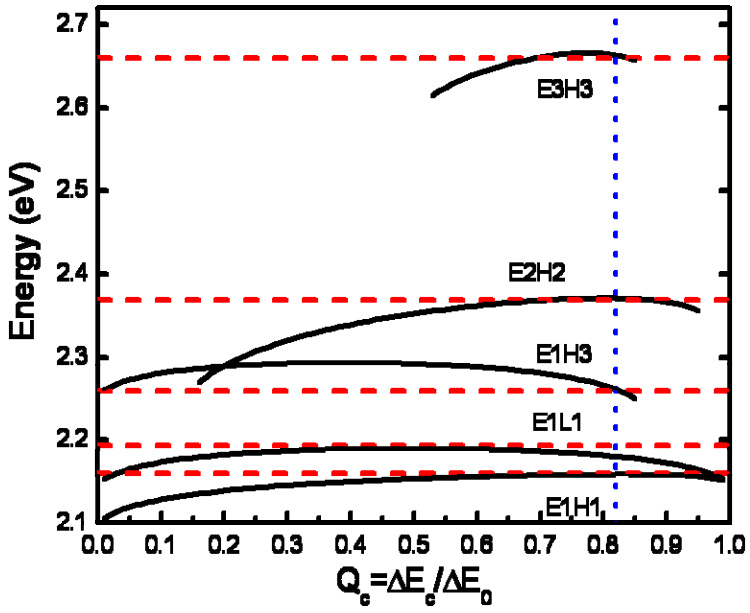

Figure 4.6 Energy of the transitions determined by the envelope function approximation vs. Qc ($\Delta E_c / \Delta E_0$).

The result is in agreement with the common anion rule,[38,48] which states that two semiconductors with a common anion and lattice matched should have most of the band discontinuity in the conduction band.

Conclusion

As stated previously, the shortest wavelength that a QCL can emit for a given material system is inversely proportional to the electron confinement (i.e., the band offset in the conduction band). To approach shorter wavelength ISB device applications, semiconductor systems with a large conduction band discontinuity are required. The identification of other near lattice-matched systems with large CBO, such as the one presented here, may yield practical alternatives for the design of these complex device structures.

Using CER and EFA we have determined that the CBO of a representative $Zn_{0.53}Cd_{0.47}Se/Zn_{0.27}Cd_{0.23}Mg_{0.50}Se$ single QW structure lattice-matched to InP is given by Q_c=0.82±0.02, yielding a value of ΔE_c of 590 meV. This large band offset suggests that this system may be a good candidate for mid-infrared ISB device applications. This method for determining CBO is a reliable non-destructive technique, very useful for further ISB device structure design and study.

Chapter 5

$Zn_xCd_{1-x}Se/Zn_{x'}Cd_{y'}Mg_{1-x'-y'}Se$ based quantum well infrared photodetector structures

The wide band gap II-VI material system ZnCdSe/ZnCdMgSe has been proposed to be a promising candidate to fabricate quantum well infrared photodetectors (QWIPs)[62] working in the shorter wavelength range due to its large and tunable conduction band offset (CBO).[63] According to our contactless electroreflectance (CER) studies, the CBO of $Zn_xCd_{1-x}Se/Zn_{x'}Cd_{y'}Mg_{1-x'-y'}Se$ system has been determined to be as large as 1.12 eV[64] (when y' = 0), which satisfies the requirement for QWIPs working at mid-IR and near IR ranges. For our range of interest, 3~5 μm, chlorine-doped $Zn_xCd_{1-x}Se/Zn_{x'}Cd_{y'}Mg_{1-x'-y'}Se$ QWIP structures with different quantum well (QW) widths were grown by MBE lattice-matched to InP substrates. A series of characterization techniques were employed to study the samples' optical properties and to evaluate their quality. The carrier recombination process, involving both radiative and non-radiative processes, was studied by temperature-dependent photoluminescence (PL) and time-resolved PL measurements. These optical investigations can greatly help to understand device performance. For instance, the quantum efficiency and operating lifetime of the devices are mainly determined by the non-radiative recombination process in the $Zn_xCd_{1-x}Se/Zn_{x'}Cd_{y'}Mg_{1-x'-y'}Se$ QWs.

5.1 QWIP structure design and growth by MBE

5.1.1 QWIP structure design

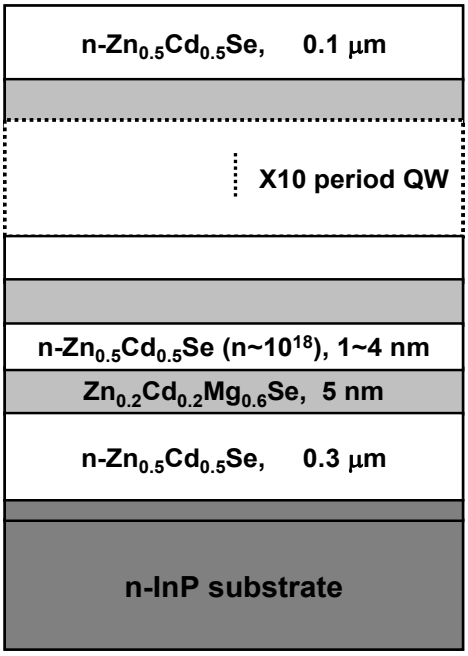

Figure 5.1 Scheme of a typical QWIP structure.

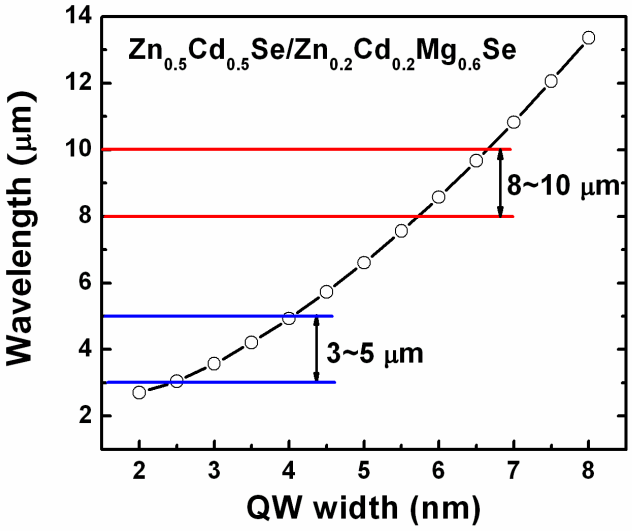

Figure 5.2 Theoretical calculation of E1-E2 ISB transition wavelength as a function of QW width based on EFA.

The QWIP structure is designed based on a theoretical calculation using the envelope function approximation (EFA),[65,66] considering that the QWs are doped. Shown in Fig. 5.1 is the scheme of a typical QWIP structure, consisting of a 10-period MQWs region sandwiched between two n-type ZnCdSe contact layers. In the designed structure, ternary alloy $Zn_{0.5}Cd_{0.5}Se$ is used as the QW material and quaternary alloy $Zn_{0.2}Cd_{0.2}Mg_{0.6}Se$ with a bandgap of ~3.0 eV (at room temperature) is used as the barrier material. The whole structure is lattice-

matched to the InP substrate and the QWs have a CBO of ~720 meV (based on previous studies). An n-type substrate was chosen for the purpose of making bottom contacts on the substrate directly. Note that due to the strong free carrier absorption from the substrate, the ISB absorption from the MQWs region was difficult to observe.

Figure 5.2 shows the theoretical calculation of the absorption wavelength according to the E_1 to E_2 ISB transition energy, plotted as a function of QW width. The parameters required for calculations, such as effective masses and spin-orbit splitting, can be obtained from a linear interpolation of the binary values using the method described in Chapter 4. The bandgaps of the QW and the barrier used in the calculation are 2.1 eV and 3.0 eV, respectively. The CBO value (Q_C) is considered to be 80% of the bandgap difference between the QW and the barrier, based on previously reported values in Ref. 2 and 3 and discussed in Chapter 4. With these parameters, a calculation is done and shows that the second electronic energy level (E_2) can be confined in the well when the QW width is wider than 2 nm. If the QW width is too thin to confine E_2, the ISB transition still can occur but through an E1-to-continuum mechanism.

Since our interest is in the 3 ~ 5 μm wavelength range, a series of QWIP structures with QW width from 1 nm to 4 nm were grown. It is important to note that unlike the usual devices based on interband transitions, the QW layers in

QWIP structures must be doped n-type to have enough ISB absorption. A doping level of $10^{+18}/cm^3$ is desired for this study.

5.1.2 MBE Growth

The MBE system used for the QWIP structure growth was described in Chapter 2. The QWIP structures were grown on n-type InP (001) substrates and consisted of a lattice-matched silicon-doped (n-type) InGaAs buffer layer (~0.1 μm), a ZnCdSe interfacial layer (~100 Å) and the remaining II-VI MQW structure illustrated in Fig. 5.1. To ensure the lattice-matching of both the $Zn_{0.5}Cd_{0.5}Se$ wells and the $Zn_{0.2}Cd_{0.2}Mg_{0.6}Se$ barriers to the InP substrate, two Zn cells were employed. The VI/II beam equivalent pressure ratio was about 3.5. The 10 periods MQW structures, with different QW widths, were sandwiched between a 3000 Å (bottom) and a 1000 Å (top) n-type $Zn_{0.5}Cd_{0.5}Se$ contact layers. The nominal thickness of the $Zn_{0.2}Cd_{0.2}Mg_{0.6}Se$ barrier is 5 nm. The $Zn_{0.5}Cd_{0.5}Se$ well widths are 4 nm, 3 nm, 2 nm and 1 nm, for samples A, B, C and D, respectively. All the QW layers and the contact layers were doped by chlorine (Cl), obtained with a $ZnCl_2$ source, which is the typical n-type dopant for wide bandgap II-VI materials. Reference samples were grown during the same run for calibrating the growth rates and doping levels. The growth rates of the quaternary and ternary layers were 1.0 μm/hr and 0.55 μm/hr, respectively. Hall Effect measurements on the reference samples gave a doping level of $1.3 \times 10^{+18}/cm^3$.

5.2 Characterization of QWIP structures

5.2.1 Electrochemical capacitance voltage profile

Electrochemical capacitance voltage (ECV) was used to characterize the doping in the QWIP structures. The ECV profile of sample A, seen in Fig. 5.3, shows that the net carrier (N_D-N_A) concentration in QWs region is 4 ~ 5 x $10^{+18}/cm^3$, which meets the requirement of device design. The result also agrees with the Hall Effect measurements on reference samples, which gave a free carrier concentration on the order of $10^{+18}/cm^3$. The discontinuity at ~0.555 μm in the ECV profile indicates the interface between the II-VI structure and the substrate.

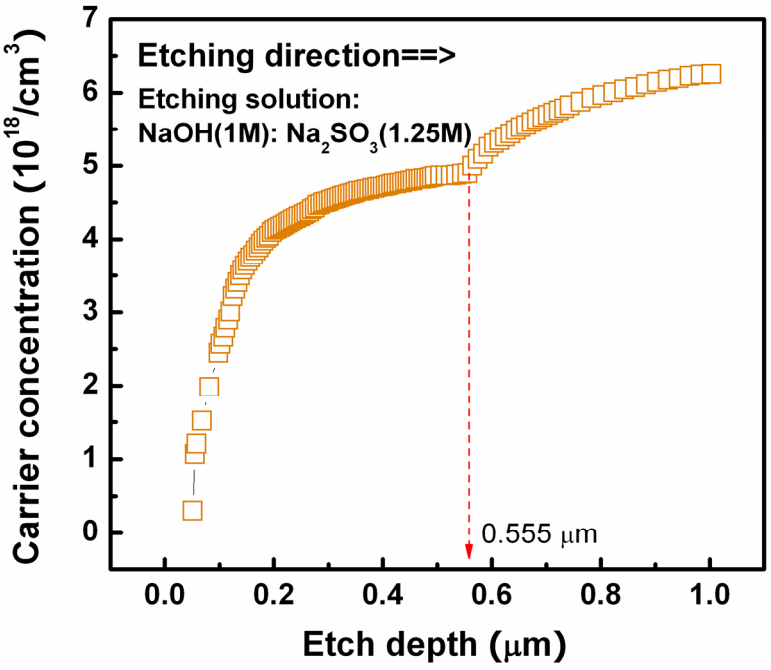

Figure 5.3 Electrochemical capacitance voltage profile of sample A.

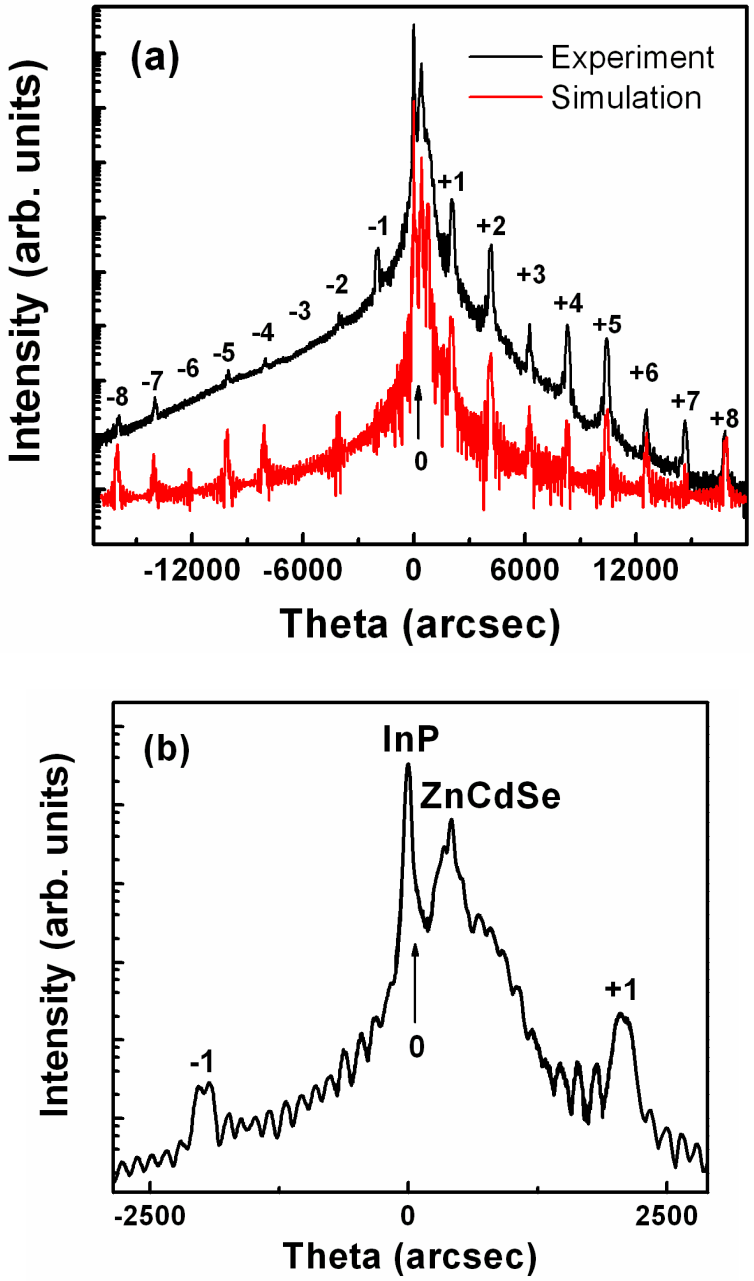

Figure 5.4 High resolution X-ray diffraction curve (black line) of sample A and the simulation curve (red line) based on the designed values. Many satellite peaks are observed in (a), as well as thickness fringes, shown in the expanded figure (b).

5.2.2 X-ray diffraction

For the purpose of device fabrication it is essential to establish the material quality. X-ray diffraction (XRD) measurements were used to characterize the structural properties of the samples. The ZnCdMgSe barrier and the QW layers were almost lattice-matched to the InP substrate, with $\Delta a/a$ = 0.2% and $\Delta a/a$ = -0.2%, respectively. The mismatch of the barrier layer was calculated from the X-ray data of a thick layer of ZnCdMgSe. The composition of the QW layer was the same as the two thick ZnCdSe contact layers. Thus, the mismatch of the QW layer can be obtained from the X-ray data of the ZnCdSe layers, the second dominant peak in the high resolution XRD (HRXRD) curve shown in Fig. 5.4.

Clear satellite peaks were observed for all the samples. From the spacing of the satellite peaks, the periodicity P of the MQWs can be accurately determined by:

$$P = \frac{\lambda}{2\cos\theta_0 \cdot \Delta\theta} \tag{5.1}$$

where λ is the wavelength of the X-ray source, θ_0 is the position of the zero-order peak from the MQWs, and $\Delta\theta$ is the difference in the angle between satellite peaks. Figure 5.4 (a) shows a HRXRD curve of one QWIP structure (sample A) and the simulation curve based on a calculation of the designed structure parameters. Excellent agreement is achieved between the two curves with many satellite peaks, up to the 8th order, observed. A periodicity of 90 Å calculated from

the XRD data agrees well with the designed value of sample A, indicating very good control of the growth. The QW widths of the four samples, therefore, were estimated from the XRD data, which were 36 Å, 27 Å, 17 Å and 12 Å, respectively. The appearance of clear thickness fringes, evident in Fig. 5.4 (b), is an indication of excellent crystalline quality of the sample.

5.2.3 Photoluminescence

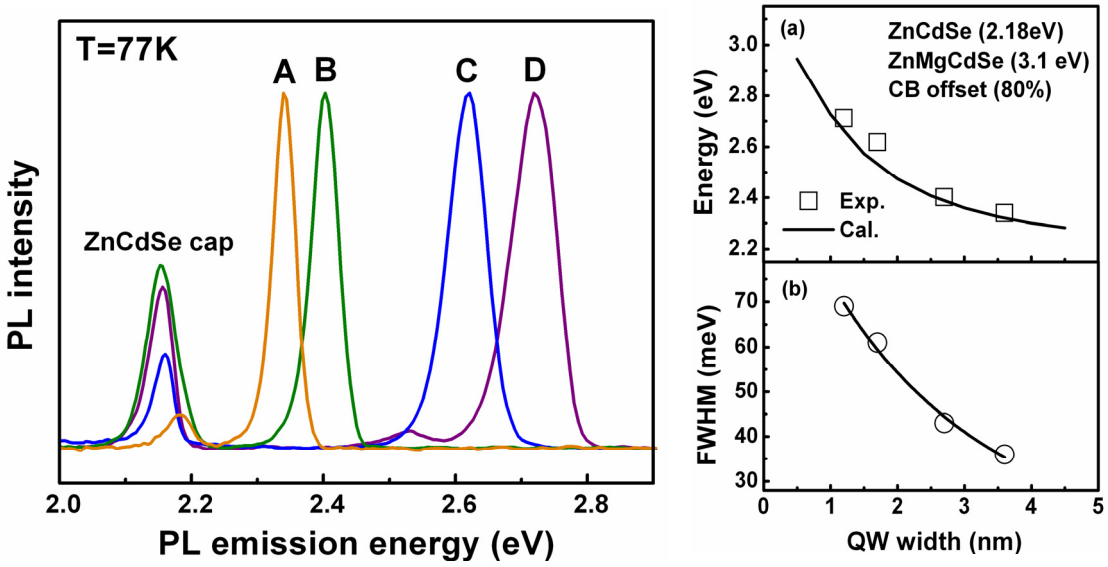

Figure 5.5 PL emission of four ZnCdSe/ZnCdMgSe QWIP structure samples. The solid line in fig. (a) is the plot of PL emission energy as a function of QW widths. The experimental data are presented by the square dots. (b) shows that the FWHM of PL emission decreases as the QW width increase. The solid line in (b) is drawn to guide the eyes.

All the QWIP structure samples were characterized by steady state photoluminescence (PL) measurements. The four samples were mounted into a low temperature cryostat where the sample temperature could be varied from liquid-nitrogen temperature (77 K) to room temperature (300 K). Continuous wave (cw) PL was excited at different temperatures by a 325 nm He–Cd laser and measured using a 0.22 m SPEX 1680-B double spectrometer connected to a photomultiplier.

Strong and sharp interband PL emission was observed for all the samples, as shown in Fig. 5.5. As expected, the PL peak shifted to short wavelength with decreasing QW width due to strong quantum confinement effects. The PL emission from the $Zn_{0.5}Cd_{0.5}Se$ cap layers of the four samples were observed at about 568 nm. No PL signal from the barrier layers was observed owing to efficient carrier transfer from the barriers to the wells. The inset (a) of Fig. 5.5 shows the PL emission peak energy as a function of QW width. According to the PL spectrum measured on a single $Zn_{0.2}Cd_{0.2}Mg_{0.6}Se$ epi-layer grown on InP substrate, the bandgap of the $Zn_{0.2}Cd_{0.2}Mg_{0.6}Se$ materials is 3.1 eV at 77K. By taking a CBO ratio Qc of 0.80,[63] the CBO of the investigated samples is calculated to be 736 meV while the valence band offset (VBO) is 184 meV. The quantization energies of the ground states of electrons (E1) and holes (H1) in the $Zn_{0.5}Cd_{0.5}Se/Zn_{0.2}Cd_{0.2}Mg_{0.6}Se$ MQWs were obtained by using the envelope function approximation (EFA),[65,**66**] and shown by the solid line. The measured PL

peak energies of the four samples as functions of the well width are shown by the square dots in fig. (a) and agree well with the calculated results. This indicates that the element compositions and the layer thicknesses were well controlled during the material growth.

The FWHM of the PL emission decreases with increasing well width (fig. (b) of Fig. 5.5), which is expected since PL signals from thicker wells are less sensitive to broadening due to the interface roughness. For our samples, even the one with the thinnest well has a FWHM less than 70 meV.

The temperature-dependent PL spectra are shown in Fig. 5.6 (a), (b), (c), and (d) for samples A, B, C and D, respectively. Since the luminescence efficiencies of these samples are different, different laser powers were used for excitation in order to obtain sufficient luminescence signal at temperatures up to room temperature, which are 0.3 mW for sample A and B, 1.5 mW for sample C and 0.7 mW for sample D.

It is clearly seen that with increasing temperature, the PL emission intensity decreases due to a lower quantum efficiency at high temperature. A thermal energy shift is also observed for the PL emission peaks from all the samples. The luminescence of sample A and B quenches very slowly and remains strong at room temperature while the luminescence of samples C and D quenches rapidly to near zero intensity, indicating a better material quality of samples A and B. The PL intensity of sample C dropped quickly and almost

disappeared when temperature reached 200 °C. This may due to a few shutter failures during the growth, which introduced more defects into the sample structure, especially the interfaces.

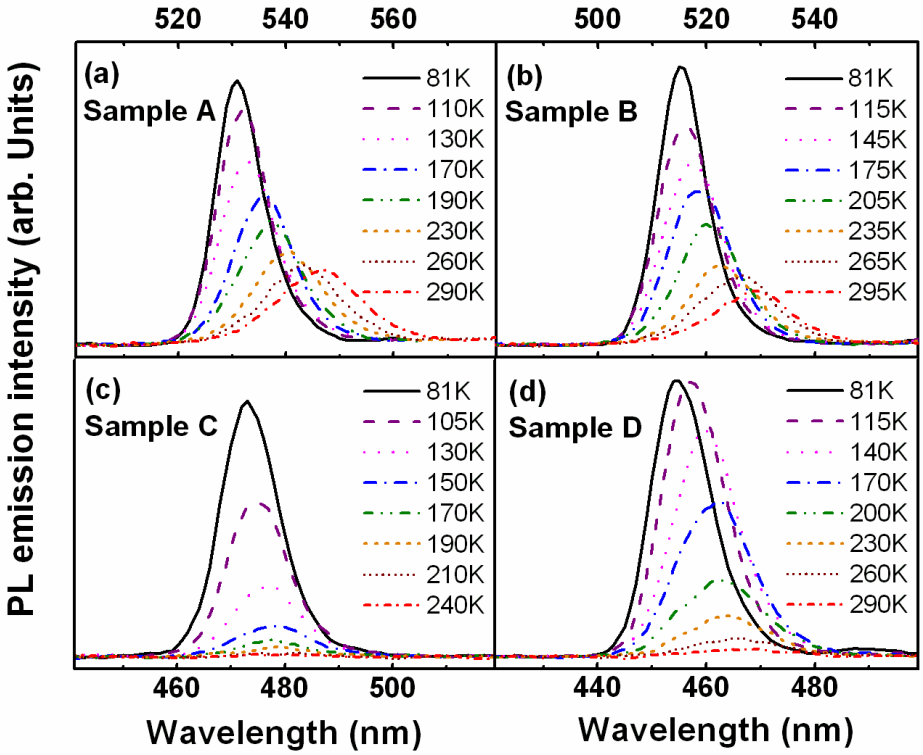

Figure 5.6 Temperature-dependent PL spectra of four QWIP structures. The temperature varies from low (liquid-nitrogen) temperature to room temperature while the other conditions remain the same for the measurements.

5.2.4 Time-resolved photoluminescence

Temperature-dependent time-resolved PL spectroscopy was used to characterize the carrier recombination processes in these samples. In the experimental setup, the second harmonic radiation at 400 nm obtained from a

mode-locked tunable Ti-Sapphire laser (Spectra Physics Tsunami) was used as excitation source. The laser pulses have a pulse width of 100-fs and a repetition rate of 82 MHz. The power of the 400 nm second harmonic radiation was measured to be 3 mW with 5% fluctuation. The time evolution of the luminescence was recorded in 2000 picoseconds by a streak camera (Hamamatsu Model C5680) with a typical temporal resolution of 10 ps. A short-wavelength pass filter was used after the second harmonic crystal to block the 800 nm laser beam and a long-wavelength pass filter was used in the front of the streak camera to block the 400 nm laser beam reflected by the samples. A series of band-pass filters, with center wavelengths ranging from 450 nm to 540 nm and a FWHM of 10 nm, were used to select luminescence wavelength range of interest and follow the PL peak signal at various temperatures. The carrier transfer time is in the sub-picosecond regime,[67] considerably shorter than the typical minority carrier lifetime in semiconductors. Therefore carrier transfer time has no influence on the time-resolved PL measurements.

Temperature-dependent PL spectra of these samples were used for selecting proper band-pass filters to follow the peak wavelengths at different temperatures for the t-PL measurements. The wavelength ranges of the MQW PL peaks in 77 K~295 K are listed for each sample in Table III. The corresponding band-pass filters used for the t-PL experiments are also listed in Table III. As shown later, the PL decay time is not sensitive to the center

wavelength of the filters used. Therefore the use of different filters will not distort the measured temperature dependence of the PL decay time. Since the FWHM of these filters is 10 nm, the PL signals were collected in a 10 nm wavelength range with the center wavelengths listed in Table III.

Table III. Parameters for samples A, B, C and D: well widths, PL peak wavelengths, center wavelengths of band pass filters used for t-PL experiments, γ factors, B^{-1} factors and the activation energies (Ea) obtained from best fitting of the whole τ_{PL} ~ T curves defined by Eq. (5.9). The values are less reliable because of the weak non-radiative process in sample A and weak radiative process in sample C.

	Well width (nm)	PL peak in 77 ~ 295 K (nm)	BP Filter λ (nm)	a ($psK^{-\gamma}$)	b (ps)	γ	B^{-1} ($K^{-1/2}ps^{-1}$)	Ea (meV)
A	4.0	530~545	530, 540	0.02	369	1.4	(4×10^{-6})	(11)
B	3.0	516~529	520, 530	0.8	259	1.2	9×10^{-5}	20
C	2.0	473~487	470, 480	(0.6)	(-330)	(1.4)	0.013	28
D	1.0	455~468	450, 460	0.7	300	1.1	0.03	70

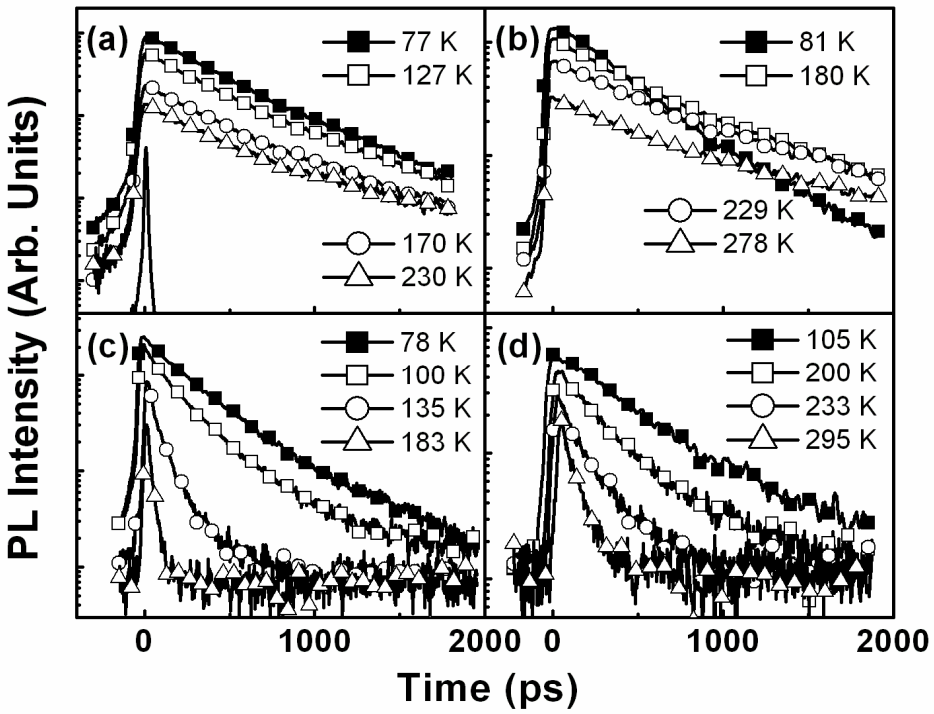

Figure 5.7 Time-resolved PL spectra of samples A (a), B (b), C (c) and D (d) measured at different temperatures. The solid line shown in (a) is the measured laser line.

Time-resolved PL spectra of the four samples were measured at different temperatures in the range of 77 K ~ 295 K. As examples, the temporal profiles of the photoluminescence at four different temperatures for samples A, B, C and D are shown in Fig. 5.7 (a), (b), (c) and (d), respectively. The temporal profile of the laser measured by the system is shown by the solid line in Fig. 5.7 (a). It can be seen that all the PL traces decay exponentially with time and can be well described by a first order exponential equation,

$$I(t) = I_0 e^{-t/\tau_{PL}} + C, \tag{5.2}$$

where I is the PL intensity at time t, I_0 is the maximum PL intensity at t = 0, τ_{PL} is the PL decay time and C represents noise level. Since the investigated QWIP structures were n-type and heavily doped, the PL decay time represents the lifetime of the minority carriers, holes. The time-resolved PL traces of samples C and D decay much faster with increasing temperature while the samples A and B decay slowly.

5.3 Radiative and non-radiative recombination processes

Relaxation processes of excess electrons and holes in semiconductor quantum structures are an important subject both from the basic physics point of view and for their applications in quantum devices. If the recombination process produces photon emission, it is called radiative; otherwise we have non-radiative recombination processes. Radiative processes, which are usually observed in luminescence, involve exciton and free carrier recombination and reflect wavefunction overlap of electrons and holes.[68] Non-radiative processes involve carrier-phonon and carrier-carrier interactions and their mechanisms include carrier capture by defect levels, Auger recombination and carrier escape through thermal emission.[69]

In order to realize practical devices, the investigation of carrier recombination processes in these QWIP structures is of prime importance. The quantum efficiency and operating lifetime of devices depend strongly on the non-

radiative recombination process. Few experiments have been previously done to study carrier recombination in ZnCdSe materials. Radiative recombination of free carriers and excitons in ZnCdSe/ZnSe[70] and ZnCdSe/ZnSSe[71] quantum wells was studied and found to rely on photoinjected density[70] and carrier density,[71] respectively. Carrier recombination processes in ZnCdSe/ZnCdMgSe MQWs have not been studied despite their great potential in device applications for light emitters and photodetectors.

5.3.1 Photoluminescence decay time

A temperature-dependent time-resolved PL study was used to characterize radiative and non-radiative recombination in the QWIP structures. The competition of the radiative and non-radiative processes was clearly illustrated by the temperature dependence of the PL decay time.

By fitting the time-resolved PL traces to Eq. (5.2), the PL decay times at different temperatures were obtained and plotted as a function of temperature for each sample. The results for samples A, B, C and D are shown in Fig. 5.8 by solid squares, hollow squares, circles and triangles, respectively. At some data points, two τ_{PL} values for one sample were plotted at about the same temperatures in Fig. 5.8. They were obtained from the experiments with the two different band-pass filters listed in Table III. The τ_{PL} values remain almost unchanged though the detection wavelength range shifted 10 nm. This indicates

weak dependence of the PL decay time on the photon energy in the 10 nm range.

The PL decay times of samples A and B increase almost linearly with increasing temperature except for a small drop for sample B near room temperature. This behavior is in good agreement with the temperature dependence of radiative recombination in quantum wells.[72] For sample B, the involvement of non-radiative recombination can be observed as a decrease of the decay time at temperatures greater than 230 K. The decay time of sample C decreases rapidly with the increasing temperature and goes down to 14 ps at 295 K, close to the 10 ps resolution of the system. The decay time of sample D increases to a maximum at about 130 K and drops with the increasing temperature. This indicates a larger contribution of non-radiative recombination in samples C and D and explains the low luminescence efficiencies of these two samples.

The PL decay time reflects the competition between radiative and non-radiative recombination processes,

$$\frac{1}{\tau_{PL}} = \frac{1}{\tau_{rad}} + \frac{1}{\tau_{non}}, \tag{5.3}$$

where τ_{rad} and τ_{non} are radiative and non-radiative recombination times, respectively.

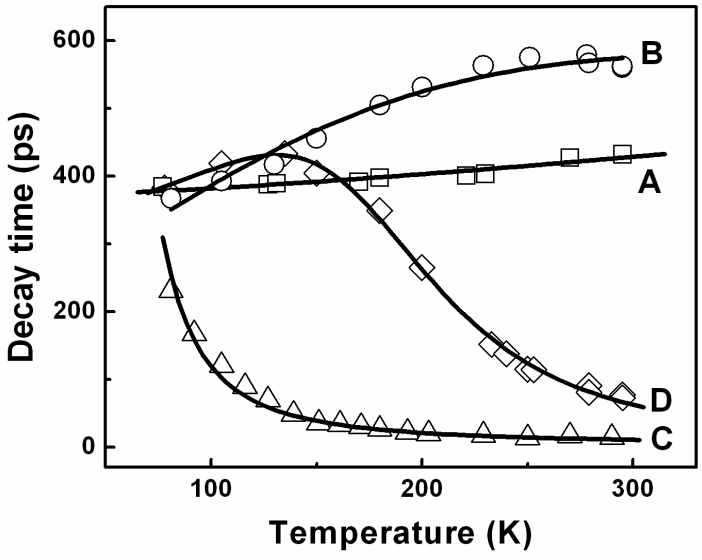

Figure 5.8 Measured (dots) and fitted (solid lines) temperature dependence of the PL decay times of samples A, B, C and D. The fitting curves were calculated according to Eq. (5.9) by considering $\tau_{rad} \propto T^{\gamma}$ for radiative recombination and Eq. (5.7) for non-radiative recombination.

5.3.2 Radiative recombination processes

Free carrier, free exciton, bound and localized exciton recombination are responsible for radiative recombination processes in semiconductors. The lifetimes of bound and localized excitons are independent of temperature and only a decrease of the emission density is expected with increasing temperature because of ionization of the bound or localized excitons.[73,74] Obviously, they are not involved in the radiative recombination processes in the investigated samples. The lifetime of free excitons has a linear relationship with temperature.[73] However, the free excitons could not survive in our samples

because they would be strongly screened by electrons with an area density of about 10^{11} ~ 10^{12} cm^{-2}. [68,72] The area density was estimated by multiplying the measured electron concentrations by the well widths.

Free carrier recombination is the dominant source of radiative recombination processes in the investigated samples. The PL decay time of samples A (for 77 K < T < 300 K) and B (for 77 K < T < 230 K) is found to be proportional to T^{γ}, where γ is 1.4 for sample A and 1.2 for sample B. These values agree very well with the theory of free carrier recombination in quantum wells,[75] where $\tau_{rad} \propto T^{\gamma}$ is expected with the value of γ between 1 and 1.5.

Since the radiative recombination time τ_{rad} is proportional to T^{γ},[75] it is reasonable to express the radiative recombination time as a function of temperature to be:

$$\tau_{rad} = aT^{\gamma} + b \tag{5.4}$$

where a and b are constants. The constant a is related to the density of states of the ground states of electrons and holes, and is proportional to the inverse of electron concentration of the quantum wells.[75] The constant b reflects the background noise and should be zero in the ideal case.

5.3.3 Non-radiative recombination processes

Non-radiative recombination processes in quantum wells include carrier capture by defect levels, Auger recombination and carrier escape through thermal emission.[69] In the Auger process, recombination energy is transferred to

a third carrier. The Auger process becomes important at high temperatures while carrier concentration is high. For example, in p-GaAs with a carrier concentration of $1.2x10^{19}/cm^3$, Auger process was observed for temperature higher than 450 K. [76, 77] Apparently, Auger recombination cannot account for the strong temperature dependence of the PL decay time in the temperature range of 77 K ~ 295 K shown in Fig. 5.8.

Carrier escape through thermal emission is important when the barrier of the quantum wells is low. This type of non-radiative process was observed in $In_yGa_{1-y}P/(Al_xGa_{1-x})_{1-y}In_yP$ and $In_yGa_{1-y}As/GaAs/Al_xGa_{1-x}As$ quantum wells with low barrier heights, where the numbers of electrons and holes escaping from the wells were suggested to be equal.[78,79] If only one type of carrier escaped, an electric field would be built up at the barrier/well interface that would prevent these carriers from further thermal emission. The barrier heights of the $Zn_{0.5}Cd_{0.5}Se/Zn_{0.2}Cd_{0.2}Mg_{0.6}Se$ MQW samples are high: 736 meV (29 kT at 300 K) for electrons and 184 meV (7 kT at 300 K) for holes. Therefore thermal emission can be ignored for the non-radiative processes in these samples.

The observed temperature dependence of the non-radiative recombination time can be well explained by considering hole capture by acceptor-like defect centers through multi-phonon emission (MPE). Multi-phonon emission was first recognized to be a typical non-radiative recombination source by Lang *et. al.*[80] The MPE capture by a deep level originates from lattice thermal vibrations that

cause the crossing of the carrier energy band and the defect energy. The captured carriers will then rapidly relax to their balanced energy position by emitting lattice phonons.

The capture cross section depends strongly on temperature,[80]

$$\sigma(T) = \sigma_0 e^{-\frac{Ea}{kT}}, \tag{5.5}$$

where σ_0 is the cross section at $T \to \infty$ and Ea is the activation energy under the MPE assumption.

For carrier capture by a single deep level, the non-radiative recombination lifetime of carriers is,[81]

$$\tau_{non} = \frac{1}{c(T)N_t}, \tag{5.6}$$

where $c(T)$ is the carrier capture coefficient and N_t is the density of the non-radiative recombination centers. Considering the mean thermal velocity of carriers $v_{th} = (3kT/m^*)^{1/2}$ and $c = \sigma v_{th}$, and combining Eq. (5.5) and (5.6), the carrier lifetime under MPE capture is obtained to be:

$$\tau_{non} = \frac{(m^*)^{1/2}}{(3k)^{1/2}\sigma_0 N_t} T^{-1/2} e^{\frac{Ea}{kT}}, \tag{5.7}$$

where m^* is the effective mass of the carriers. Eq. (5.7) can be simplified as:

$$\tau_{non} = BT^{-1/2} e^{\frac{Ea}{kT}}, \tag{5.8}$$

where $B = \frac{(m^*)^{1/2}}{(3k)^{1/2}\sigma_0 N_t}$. If the effective mass and the cross section at $T \to \infty$ have weak dependences on well width, the value of B^{-1} will represent the density of

defects. Therefore, the non-radiative recombination process observed in our samples can be well-described by hole capture through the MPE mechanism.

5.3.4 Competition of radiative and non-radiative processes

The τ_{PL} ~ T curves of samples A, B, C and D in Fig. 5.8 can now be fitted according to Eq. (5.3) by considering $\tau_{rad} = aT^{\gamma} + b$ for radiative recombination and Eq. (5.7) for non-radiative recombination. The full expression for fitting τ_{PL} *vs* T curves is

$$\frac{1}{\tau_{PL}} = \frac{1}{aT^{\gamma} + b} + \frac{1}{BT^{-1/2} e^{\frac{Ea}{kT}}}, \tag{5.9}$$

where a, b, γ, B and Ea are fitting parameters.

The fitting results are shown by the solid lines in Fig. 5.8 and are in good agreement with the experimental data. To fit sample A's data, only radiative recombination was considered. To fit the data of sample C, only non-radiative recombination was considered. To fit the τ_{PL} ~ T curves of samples B and D, both free carrier recombination and MPE recombination were considered and combined by Eq. (5.9). Three important parameters, the γ factor, the activation energy Ea and the B^{-1} factor, were derived and are listed in Table III for each sample. Note that the Ea values were obtained by fitting the whole τ_{PL} *vs* T curve defined by Eq. (5.9) while both non-radiative and radiative recombination processes were considered. All γ factors are between 1 and 1.5 and are coincident with the character of free carrier recombination.

The portion of the non-radiative recombination processes in the narrow wells (samples C and D) was much larger than that in the wide wells (samples A and B). This was observed in C and D as low luminescence efficiencies and rapid decrease of the PL decay time with the increasing temperature. The acceptor-like defects were probably related to the imperfection of interfaces of the MQWs. The B^{-1} factor is proportional to the defect density N_t and can be used to evaluate material quality. Figure 5.9 shows the B^{-1} factors for different well widths. It is clearly seen that the defect density increases with decreasing of the well width. This strongly supports our conclusion that the defects originate from the interfaces.

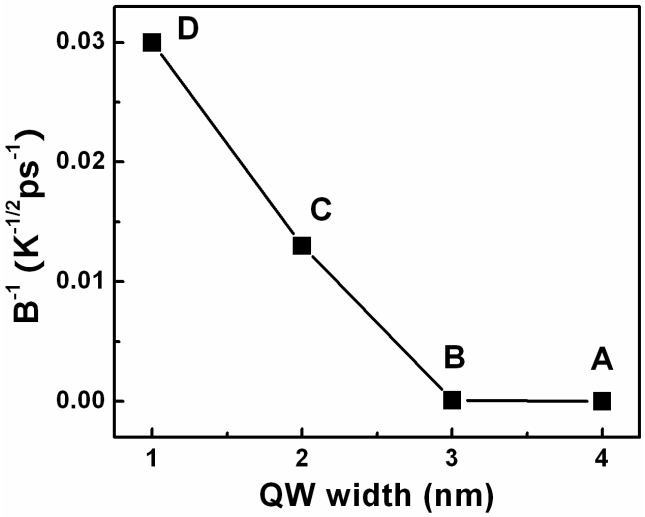

Figure 5.9 The B^{-1} factor as a function of the well width, where B^{-1} is proportional to the defect density N_t.

The competition between radiative and non-radiative recombination processes is directly reflected in the temperature dependence of the PL intensity. The scattered dots in Fig. 5.10 show the integrated PL intensities of the QWs of sample A, B, C and D measured at different temperatures. The integrated PL intensity is expressed as a function of temperature by a phenomena formula,[82,83,84]

$$I(T) = \frac{I_0}{1 + C\exp(-\Delta E / kT)}, \tag{5.10}$$

Where I_0 is the PL intensity at $T \to 0$, C is regarded as a constant, and ΔE is the activation energy responsible for the quenching of PL intensity and is usually used to evaluate material quality.

In the following, we deduce a full expression of $I(T)$ and demonstrate that for our samples the activation energy ΔE originates from MPE and equals the activation energy Ea for hole capture through MPE.

The luminescence efficiency η is determined by the radiative and non-radiative lifetimes of the carriers to be:

$$\eta = \frac{\tau_{PL}}{\tau_{rad}} = \frac{1}{1 + \tau_{rad} / \tau_{non}}, \tag{5.11}$$

where Eq. (5.3) was used in the derivation. Substituting τ_{rad} by $aT^{\gamma} + b$ and τ_{non} by Eq. (5.8) into the above equation, and considering the PL intensity I = I_0 η, the full expression of the PL intensity is obtained

$$I(T) = \frac{I_0}{1 + B^{-1}T^{1/2}(aT^{\gamma} + b)\exp(-E_a / kT)}. \quad (5.12)$$

Comparing Eqs. (5.10) and (5.12), one can obtain ΔE = Ea and C = $B^{-1}T^{1/2}$ ($\tau_{rad} = aT^{\gamma} + b$). Eq. (5.12) gives a clear physical picture of the temperature dependence of the luminescence intensity while the non-radiative recombination mechanism is MPE.

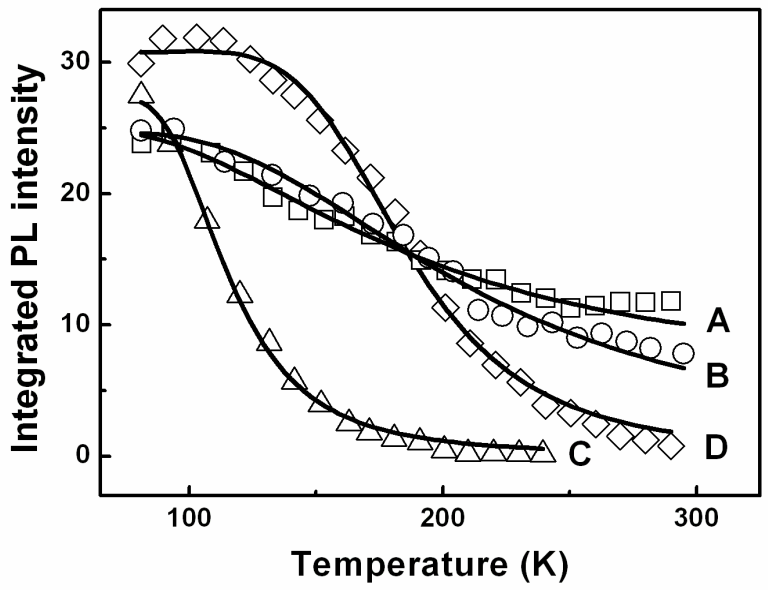

Figure 5.10 Measured (dots) and fitted (solid lines) temperature dependence of the integrated PL intensities of samples A, B, C and D. The solid curves were fitted according to Eq. (5.12) while the parameters in Table III were used.

Since the important parameters such as B, γ and Ea were already known by fitting the temperature dependence of the PL decay time, we are able to fit the temperature dependence of the PL intensities of the four samples using Eq.

(5.12). To do so, the parameters of B^{-1}, γ and Ea in Table III were used for sample B, C and D. For sample A, B^{-1} and Ea are considered as fitting parameters. The fitted I vs. T curves for the four samples are shown in Fig. 5.10 by the solid lines and agree very well with the experimental results. The values of B^{-1} and Ea for sample A were obtained by fitting the data to be 4 X 10^{-6} $K^{-1/2}ps^{-1}$ and 11 meV, respectively.

It is worthwhile to note that the parameters a and b have no direct relationship with the well width. The parameter a is related to the densities of states of electrons and holes, and is proportional to the inverse of the electron concentration.[75] The change of the parameter a at different well widths reflects the change of densities of states and the fluctuation of carrier concentration. This means that the radiative lifetime that is expressed by $\tau_{rad} = aT^{\gamma} + b$ is not directly related to the well width. For instance, the radiative lifetimes for the investigated quantum wells are all about 400 ps at 77 K, but change to 428 ps for sample A (4 nm width), 1010 ps for sample B (3 nm width) and 671 ps for sample D (1 nm width) at 300 K.

The excellent fit to the τ_{PL} vs. T and I vs. T data for samples A, B, C and D is encouraging us to further investigate the well width dependence of the MPE activation energy. For hole capture by the acceptor-like defects, the activation energy depends on the quantization energy of the quantum wells by[85]

$$Ea = \frac{(E_t + E_0 - S\hbar\Omega)^2}{4S\hbar\Omega}, \tag{5.13}$$

where E_t is the energy distance of the defect level from the valence band, E_0 is the quantization energy of the ground state of heavy holes, S is the Huang-Rhys factor and $\hbar\Omega$ is the phonon energy of the emitted phonons.

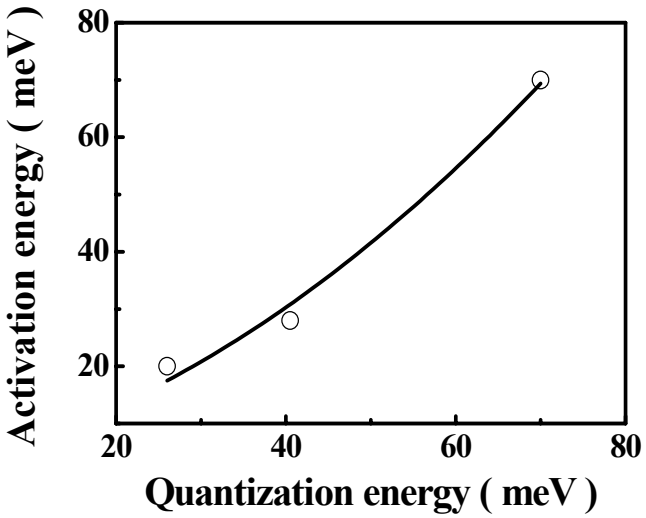

Figure 5.11 Measured MPE activation energies as a function of the quantization energy in the investigated multi-quantum wells (dots) and the fitting result (solid line) according to Eq. (5.13).

The experimentally determined activation energies Ea are shown by the dots in Fig. 5.11 as a function of the quantization energies for samples B, C and D. The data were fitted to Eq. (5.13) and the results are shown by the solid line in Fig. 5.11. The defect level was determined to be 45 meV above the valence band maximum and the $S\hbar\Omega$ value was 28 meV. Taking a LO phonon energy $\hbar\Omega$ of

30 meV for $Zn_{0.5}Cd_{0.5}Se$,[86,87] the Huang-Rhys factor was deduced to be 0.93. This indicates a weak coupling between the defect level and lattice.

Conclusions

In summary, we have grown and investigated the optical properties of highly doped $Zn_xCd_{1-x}Se/Zn_{x'}Cd_{y'}Mg_{1-x'-y'}Se$ QWIP structures. The measured doping level of $10^{+18}/cm^3$ meets the device requirements. Excellent material quality and growth control of multi-layers by the MBE technique has been demonstrated by XRD, PL and time-resolved PL measurements. The calculations' results show that the $Zn_xCd_{1-x}Se/Zn_{x'}Cd_{y'}Mg_{1-x'-y'}Se$ material system can be designed for intersubband device applications, such as QWIPs, operating in the expected wavelength range. The designed $Zn_xCd_{1-x}Se/Zn_{x'}Cd_{y'}Mg_{1-x'-y'}Se$ MQWs can be grown with high quality by the well-controlled MBE method. Thus, the $Zn_xCd_{1-x}Se/Zn_{x'}Cd_{y'}Mg_{1-x'-y'}Se$ material system is a very promising candidate for fabricating mid-IR intersubband devices.

Temperature-dependent time-resolved photoluminescence spectroscopy was used to investigate carrier recombination processes in these QWIP structures. It was found that radiative recombination is dominated by free carrier recombination in $Zn_xCd_{1-x}Se/Zn_{x'}Cd_{y'}Mg_{1-x'-y'}Se$ MQWs with wider well widths and non-radiative recombination arises from hole capture by acceptor-like defects through multi-phonon emission (MPE). Carrier recombination processes in these

samples were attributed to the interplay between free carrier recombination and hole capture through MPE. The expressions for the temperature dependent PL decay time and PL intensity were deduced, and were used to successfully fit the experimental data. Important features of the non-radiative recombination centers, such as the activation energy and the defect density, were obtained. The density of the defects depends strongly on well width, indicating their interfacial feature. A weak coupling with lattice was found for these defects.

Chapter 6

Contactless electroreflectance studies of $Zn_xCd_{1-x}Se/Zn_{x'}Cd_{y'}Mg_{1-x'-y'}Se$ multiple quantum well structures

Using contactless electroreflectance (CER) and the envelope function approximation (EFA) we have determined the conduction band offset (CBO) of the $Zn_xCd_{1-x}Se/Zn_{x'}Cd_{y'}Mg_{1-x'-y'}Se$ material system in a single quantum well structure (SQW).[88,89] In CER, a wide range of the possible optical transitions can be obtained. From these, the intersubband (ISB) transition energies can be predicted. Can CER be applied to study the multiple quantum well (MQW) structures or even the device structures to predict ISB transition energies, a very important information for fabricating ISB devices? How reliable are the estimated values of ISB transition energies? Can the estimation be verified using other techniques? In this chapter, these questions will be answered.

6.1 Introduction

Devices that are based on ISB transitions, such as quantum cascade lasers (QCLs) and quantum well infrared photodetectors (QWIPs), are of great interest due to their potential advantages over devices based on interband (IB) transition in the infrared range.[90,91] Intersubband devices are usually made from MQW structures and need a large band discontinuity to achieve operation at shorter wavelengths and higher temperatures. Multiple quantum well structures

made of the wide bandgap II-VI materials $Zn_xCd_{1-x}Se/Zn_{x'}Cd_{y'}Mg_{1-x'-y'}Se$ are very promising candidates for short-wave mid-infrared ISB device applications due to their large and tunable band discontinuity.[92]

Modulation techniques, such as photoreflectance (PR) and contact-less electroreflectance (CER), have been recognized as useful methods for understanding the physical properties of MQW and superlattice materials.[93, 94, 95, 96] While PR and CER have previously been used to characterize many complex structures, including device structures, such as heterojunction bipolar transistors (HBTs) and high electron mobility transistors (HEMTs),[97] we only found one earlier report using PR[98] to characterize ISB structures.

In the following, two representative $Zn_xCd_{1-x}Se/Zn_{x'}Cd_{y'}Mg_{1-x'-y'}Se$ MQW structures were investigated, for the purpose of studying the E1-E2 transition energies. Sample quality was studied by high resolution X-ray diffraction (HR-XRD) and photoluminescence (PL) measurements. Scanning electron microscope (SEM) images were taken to demonstrate the layer structure and interfaces. The interband transitions in these samples were determined using CER,[99] and the E1-E2 ISB transition energies were estimated. Fourier transform infrared spectroscopy (FTIR) measurement at room temperature (RT) was performed to confirm the estimate.

6.2 $Zn_xCd_{1-x}Se/Zn_{x'}Cd_{y'}Mg_{1-x'-y'}Se$ MQW samples

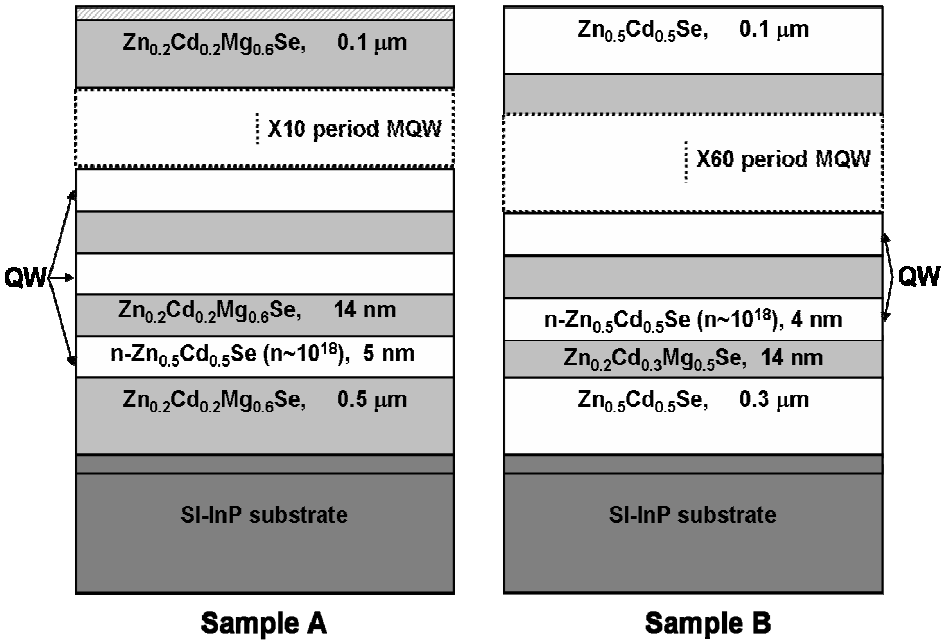

Figure 6.1 Schematic layer structures of samples A and B. For both samples, the III-V buffer layer is InGaAs. Sample A is capped by CdSe to prevent the oxidation of the ZnCdMgSe layer.

6.2.1 Sample structures

The layer structures of the two MQW samples studied are shown in Fig. 6.1. Sample A has 10 periods of $Zn_{0.5}Cd_{0.5}Se/Zn_{0.2}Cd_{0.2}Mg_{0.6}Se$ QWs sandwiched between two quaternary $Zn_{0.2}Cd_{0.2}Mg_{0.6}Se$ layers. Sample B has 60 periods of $Zn_{0.5}Cd_{0.5}Se/Zn_{0.2}Cd_{0.3}Mg_{0.5}Se$ QWs, in this case, sandwiched between two ternary $Zn_{0.5}Cd_{0.5}Se$ layers. The slight differences in the quaternary compositions were not intentional, but are due to the separation in time of the growth of the two structures. The nominal thicknesses of the wells are 50 Å and

40 Å in samples A and B, respectively, while the barriers are nominally 140 Å in both samples. The QW layers are doped n-type for ISB absorption measurements.

6.2.2 Sample growth by MBE

The two MQW samples were grown by MBE on semi-insulating InP (001) substrates following the optimized growth procedure. After the oxide desorption of the substrate was performed in the III-V growth chamber under an As flux, a lattice-matched InGaAs buffer layer (~0.1 μm) was grown, followed by 20-second Zn-irradiation and the growth of a ZnCdSe buffer layer (~100 Å) at 170 °C. The substrate temperature was then raised to 270 °C to grow the II-VI MQW structure. The VI/II beam equivalent pressure ratio was maintained at 3.5 - 4.0 during growth. In both samples, the QW layers are doped n-type using chlorine (Cl) obtained from $ZnCl_2$ as the dopant source. A doping level of $1\sim2x10^{+18}/cm^3$ for the QW layers and the growth rates (~0.6 μm/h for the ternary and ~1.5 μm/h for the quaternary) were determined from calibration layers grown separately. To prevent the oxidation of Mg in the last layer of sample A, the structure was capped by a 90 Å thick CdSe layer.

6.2.3 Sample quality

The sample quality was established by SEM, HR-XRD and PL measurements.

A cross section SEM image of sample A is shown in Fig. 6.2. The abrupt

interfaces throughout the MQW structure is clearly illustrated, indicating the good control of the MBE growth.

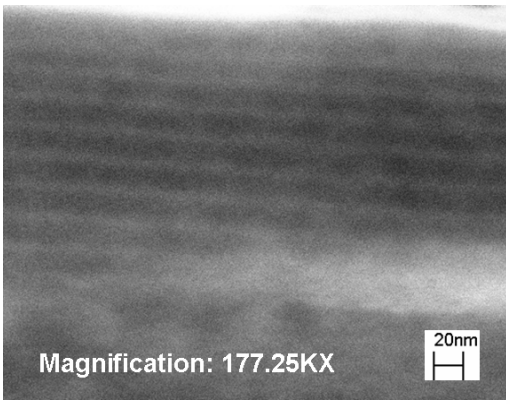

Figure 6.2 Cross section SEM image of sample A.

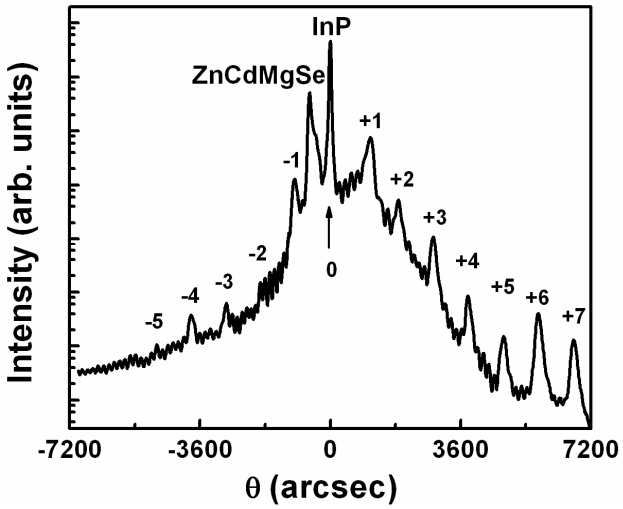

Figure 6.3 High resolution X-ray diffraction curve of sample A.

XRD measurements on the calibration samples showed that for both samples the ZnCdMgSe barrier and the ZnCdSe QW layers were nearly lattice-matched to the InP substrate. The ZnSe content in the $Zn_xCd_{1-x}Se$ QW layer is slightly different in the two samples, which are x = 0.50 for sample A and x = 0.46 for sample B, resulting in a ZnCdSe bandgap of 2.18 eV and 2.17 eV at 77K for sample A and B, respectively. Figure 6.3 is the HR-XRD curve of sample A. The ZnCdMgSe layer is almost lattice-matched to the substrate, with $\Delta a/a = 0.25\%$. The ZnSe and CdSe content in the $Zn_{x'}Cd_{y'}Mg_{1-x'-y'}Se$ were x'=0.20 and y'=0.19, respectively, corresponding to a bandgap of 3.1 eV at 77K, which was further

confirmed by PL measurement (see Fig. 6.4(a)). The thickness of one period (one barrier and one QW) of 197 Å was calculated from the XRD satellite peaks and agrees well with the designed value.

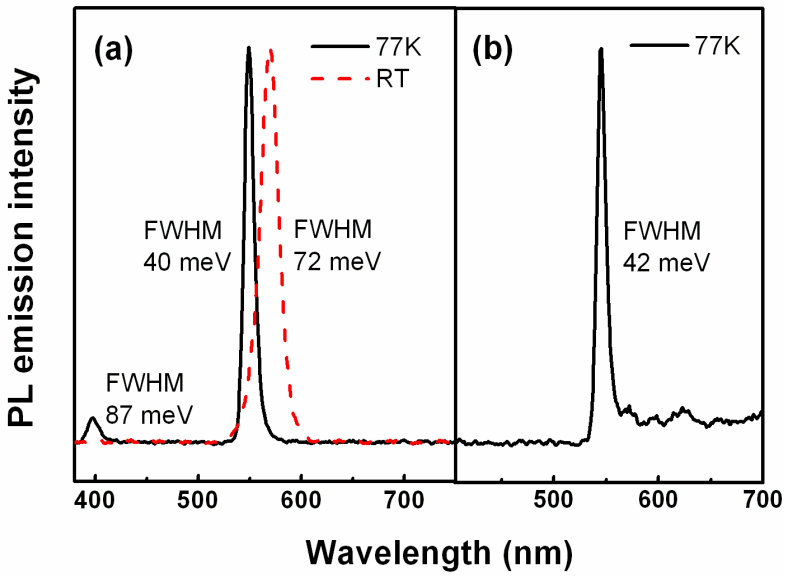

Figure 6.4 PL measurements on sample A (a) and sample B (b). PL spectra of sample A at both 77K and RT are shown in (a), while only 77K PL spectrum of sample B is shown in (b). The FWHMs of 77K PL spectra are 40 meV and 42 meV for sample A and B, respectively.

The PL measurements were performed using the 325 nm line of a He-Cd laser as an excitation source. The PL spectra are shown in Fig. 6.4. Due to the slightly different composition, the bandgaps of the quaternaries in sample A and B are 3.1 eV (see Fig. 6.4(a)) and 3.0 eV (from calibration layer), respectively at 77K. Intense and narrow PL emission peaks from the QWs in sample A were

observed at 549 nm (2.26 eV, 77 K) and 569 nm (2.18 eV, RT), shown by the dashed-dot line in Fig. 6.4(a)], with no trace of any deep level emissions. A thermal energy shift of 80 meV is observed as well as a slight linewidth broadening as the temperature increased from 77K to room temperature. Due to the strong absorption of the two thick ZnCdSe layers, the PL emission from the QWs in sample B is weak and could only be measured at 77K at 545 nm [2.275 eV, shown in Fig. 6.4(b)]. A small bump is observed at a lower energy level, due to the PL emission from the ZnCdSe layers and possibly some deep level emissions. The 77K PL emission peaks are narrow in both samples, with FWHM being 40 meV and 42 meV for each MQW peak.

6.3 Intersubband transition studies by CER

The CER measurements[99] were taken at room temperature using the light from a 150 W Xenon-arc lamp. The light intensity at wavelength λ, $I_0(\lambda)$, is focused onto the sample by means of a lens. The reflected light is collected by a second lens and is focused onto a Si photodetector. The sample was placed in a condenser-like system consisting of a front wire grid electrode with a second metal electrode separated from the first electrode by insulating spacers. The dimensions of the spacer are such that there is a very thin layer (~ 0.1 mm) of air (or vacuum) between the front surface of the sample and the wire grid of the first electrode. Thus, there is nothing in direct contact with the front surface of the sample. The electromodulation was achieved by applying an *ac* voltage of 1 kV

(peak-to-peak), 200 Hz across the electrodes.

The CER spectra of the two MQW samples are shown in Figure 6.5(a) and (b). In both, the solid line is the CER spectrum measured at room temperature. The transition energies were obtained using a fit (shown by the dashed line) based on the first derivative of a Gaussian line shape, which is the appropriate line shape due to the bound origin of the transitions.[94,95] The arrows in Fig. 6.5 indicate all the energy values of the transitions resulting from the fit. These values are also presented in Table IV. The notation EnH(L)m represents the transition from the n-th conduction subband to the m-th valence subband of heavy (H) or light (L) hole character, respectively. Comparing the two CER spectra, the signal from sample B contains more noise than that of sample A. This may be due to roughening of the surface of sample B after etching. (A 70 second chemical etching was performed on sample B using 0.1 M Bromine-methanol solution since the signal (at ~2.1 eV) from the thick ZnCdSe top layer would dominate the CER spectrum.) Furthermore, to avoid the effect of oxidation on the etched surface, only 2 CER scans were done for sample B, while 20 scans were used for the measurement on sample A, improving the signal to noise ratio in sample A. Due to the relatively high noise level of the CER spectrum of sample B, we did not try to fit the EnLm (light hole) transitions which are usually weaker.

The assignments were done according to the following considerations.

First, the signals at 3.00 and 2.96 eV were assigned to the ZnCdMgSe barriers by comparison to the 77 K PL emission from the barriers, which were observed at 3.1 and 3.0 eV, respectively, and considering the thermal energy shift from 77 K to room temperature. The signals at ~2.1 eV in Fig. 6.5(a) and (b) were assigned to the transition of the ZnCdSe grown lattice-matched to the InP substrate according to previous reports.[100] The CER transitions at 2.183 and 2.196 eV were assigned to the E1H1 transitions for sample A and B, by comparing with the PL emission signals, included in Fig. 6.5(a), Fig. 6.5(b) and in Table IV. The QW PL signal for sample B was only measured at 77K, as indicated in the experimental section, and a shift of ~80 meV due to the temperature dependence of band gap was assumed.

In order to assign the remaining transitions calculations were performed based on the envelope function approximation, considering that the QW was doped.[101,102] The values for the effective masses and spin-orbit splitting used in this calculation were obtained from a linear interpolation of the binary values.[88] Following the reported values for the conduction band offset (CBO) in References 1 and 2, we considered that the CBO is 80% of the band gap difference between the barriers and wells. Quantum well thicknesses of 52 Å for sample A and 42 Å for sample B were obtained from these calculations. The identified transitions correspond to the symmetry allowed (n=m) and symmetry forbidden but parity allowed (n=m±2, 4…) transitions. As seen in Table IV, the

calculations agree well with the measured values. The E1-E2 ISB transition energies of the two samples can be estimated to be 178 and 233 meV, which correspond to wavelengths of 6.97 and 5.32 μm.

Table IV. Experimental and calculated transition energies of the MQW structures.

	Sample A (d_{QW} = 52 Å)		Sample B (d_{QW} = 42 Å)	
IB transition	Calculation (eV)	CER (eV) (± 0.005)	Calculation (eV)	CER (eV) (± 0.005)
ZnCdSe	2.105 (RT PL)	2.098	2.183 (77K PL)	2.120
E1H1	2.181	2.183	2.191	2.196
E1L1	2.205	2.205		
E1H3	2.300	2.306	2.333	2.336
E2H2	2.405	2.412	2.487	2.490
E2L2	2.496	2.483		
E3H1	2.606	2.608	2.712	2.724
E3L1	2.630	2.633		
E3H3	2.725	2.726		
Barrier	3.10 (77K PL)	3.000	3.00 (77K PL)	2.958
ISB transition	Estimation (meV)	FTIR (meV)	Estimation (meV)	FTIR (meV)
E1-E2	178	180	233	231

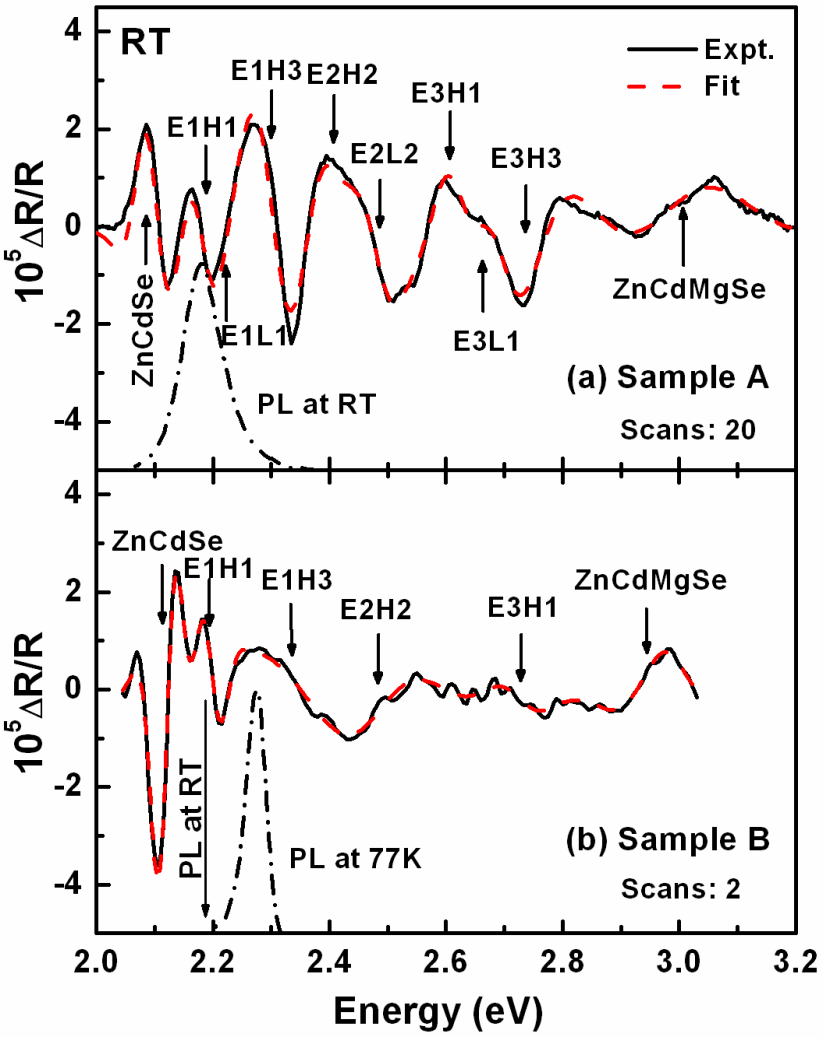

Figure 6.5 CER spectra at room temperature (RT) of (a) sample A and (b) sample B. The solid line represents the experimental data. The dashed line is a fit based on the first derivative of a Gaussian line shape, yielding the transition energies indicated by the arrows. The room temperature PL emission of sample A and the 77K PL emission of sample B, used to identify the E1H1 transition, are shown in (a) and (b), respectively.

6.4 ISB absorption measurements by FTIR

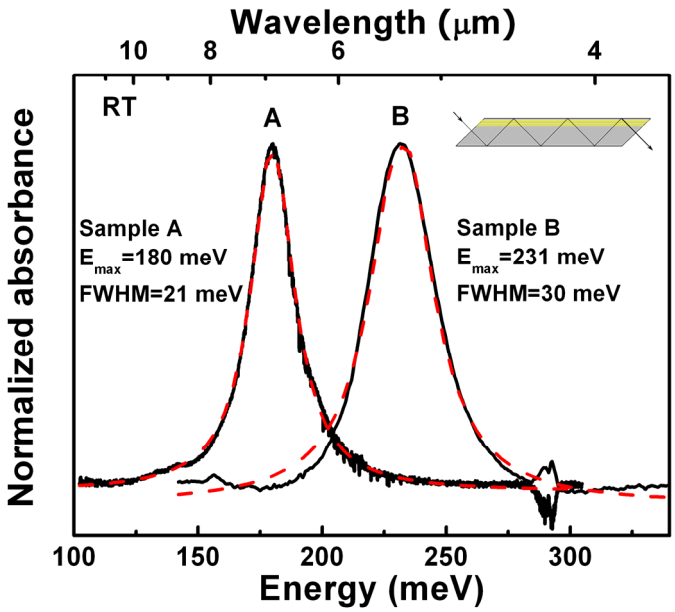

Figure 6.6 Intersubband absorption (solid line) measured by FTIR at RT and Lorentzian fit (dashed line) for samples A and B. The inset indicates the multiple-pass geometry used in the measurements.

The RT intersubband absorption was measured using a FTIR spectrometer equipped with a liquid-nitrogen (LN_2) cooled HgCdTe detector. The sample was polished to obtain a multiple-pass geometry (see inset of Fig. 6.6). Thus, the predicted values of the E1-E2 transition energies were confirmed by the FTIR measurements. The normalized absorbances of the two samples are shown in Fig. 6.6. Absorption peaks at 180 meV (6.89) and 231 meV (5.37 μm) are clearly observed and they are strongly polarization dependent. The FWHMs are 21 and 30 meV, respectively, indicating a ratio of $\Delta E/E_{peak}$ of 10% for both

samples. This suggests that the absorption is due to the bound-to-bound ISB transition E1-E2. Comparison between the FTIR results and the CER predictions indicates that an excellent agreement was achieved. This work also demonstrates the ability to readily tune the absorption wavelength of the ISB transitions in our materials by changing the QW thickness.

Conclusion

We have grown two $Zn_xCd_{1-x}Se/Zn_{x'}Cd_{y'}Mg_{1-x'-y'}Se$ MQW structures having different QW thickness, which allows us to tune the ISB transition energy within the mid-IR region. Excellent material quality, consistent with the requirements of device applications, has been demonstrated. Using CER and EFA calculations, the ground state and higher order transitions were observed and identified. From this, the E1-E2 ISB transition energies of these two structures were estimated to be 178 and 233 meV. Intersubband absorption measurements by FTIR yielded peak values at 180 and 231 meV. The excellent agreement between these two techniques shows that CER is useful to investigate optical and electronic properties of these complex structures, including prediction of the ISB transition energy. These results give further confirmation that MQW of this II-VI material system can be grown in high quality and can be designed to fabricate ISB devices whose operating wavelengths can be readily tuned within the mid-IR range by changing the QW thickness.[103]

Chapter 7

Mid-infrared intersubband absorption in $Zn_xCd_{1-x}Se/Zn_{x'}Cd_{y'}Mg_{1-x'-y'}Se$ multiple quantum well structures

A key to realize good ISB devices is to have strong intersubband (ISB) absorption. Intersubband absorption happens between discrete energy levels in the conduction (or valence) band. The quantum well region, therefore, must be doped to supply sufficient electrons (or holes) to populate the ground state. In this chapter, a series of MQW samples with different QW width were grown for the purpose of studying ISB absorption. All the QWs region were doped n-type with a carrier concentration of $10^{18}/cm^3$ order. X-ray diffraction (XRD) and Photoluminescence (PL) measurements indicate that the samples have excellent material quality. The ISB absorption was first observed in MQW structures based on this II-VI material system and the peak absorption wavelengths measured by Fourier transform infrared (FT-IR) spectroscopy are in the range of 4 ~ 7 μm, which is the region of interest for mid-infrared intersubband devices, such as quantum cascade lasers (QCLs) and quantum well infrared photodetectors (QWIPs). The experimental results fit well with theoretical predictions based on the envelope function approximation (EFA).

7.1 MBE growth of $Zn_xCd_{1-x}Se/Zn_{x'}Cd_{y'}Mg_{1-x'-y'}Se$ MQW structures

Lattice-matched $Zn_xCd_{1-x}Se/Zn_{x'}Cd_{y'}Mg_{1-x'-y'}Se$ MQW samples for ISB

absorption studies were designed for the mid-IR range of interest. Figure 7.1 is a schematic of the layer structure of the samples grown.

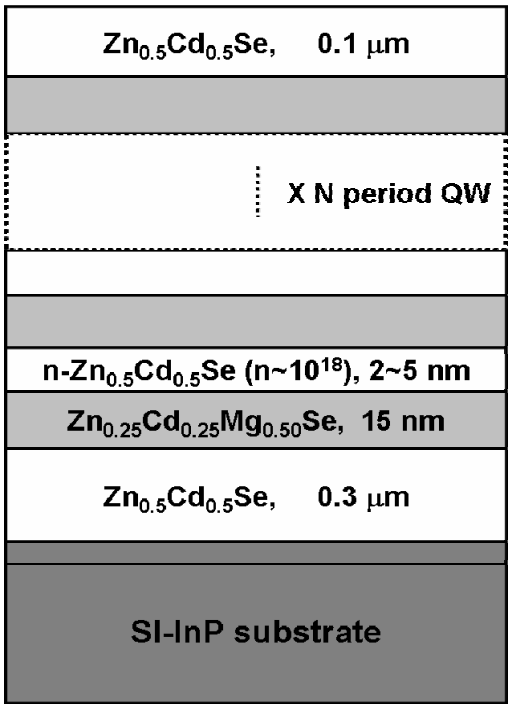

Figure 7.1 Schematic of the MQW samples for ISB absorption studies.

The intensity of ISB absorption is simply proportional to the 2-dimensional electron (hole) density and the number of quantum wells. As a result, to increase the absorption one has to either increase the doping density or increase the number of quantum wells (or both). In the $Zn_xCd_{1-x}Se/Zn_{x'}Cd_{y'}Mg_{1-x'-y'}Se$ material system, the doping density is limited to the low $10^{18}/cm^3$. Increasing doping density has other drawbacks such as increasing the dark current and thus decreasing the detectivity of the detector. Therefore, a better approach to increase the absorption intensity would be to increase the number of quantum

wells. However, in practice, the thicker the total layer thickness the more likely that problems during growth will result in poorer material quality. Thus it is a very challenging task for material scientists to increase the number of quantum wells significantly while maintaining the high material quality.

By optimizing the growth conditions we have been able to grow $Zn_xCd_{1-x}Se/Zn_{x'}Cd_{y'}Mg_{1-x'-y'}Se$ MQWs with large number of repeats (N > 50) and lattice-matched to InP (001) substrates. For desired mid-IR absorption wavelength, the QW width was varied from 2 to 5 nm, which is included in Table V.

After the oxide layer removal process on semi-insulating (SI) InP substrates, the growth of a 0.15 μm InGaAs buffer layer lattice-matched to InP followed in the III-V growth chamber. The samples were transferred through vacuum modules to the II-VI growth chamber to perform the Zn irradiation and LT-ZnCdSe buffer (~ 10 nm) growth at 200^{o}C. The substrate temperature was then raised to 300^{o}C to grow the subsequent layers. The four samples studied here consist of different periods of QWs because they were not grown at the same time. The periods are 10 for sample A (d_{QW} = 5 nm), 60 for sample B (d_{QW} = 4 nm), 80 for sample C (d_{QW} = 3 nm), and 100 for sample D (d_{QW} = 2 nm), respectively. The $Zn_{x'}Cd_{y'}Mg_{1-x'-y'}Se$ barrier thickness was about 150 Å in all the samples. According to the XRD data on the reference samples, the well had the lattice-matched composition, x = 0.46. The barrier was near lattice-matched to InP, with the Zn and Cd contents as x’ = 0.24 and y’ = 0.25, respectively,

corresponding to a bandgap of ~ 2.9 eV at RT. The MQWs region was doped with Cl (using $ZnCl_2$ as dopant source) to 1~2x10^{18}/cm^3, sandwiched between a 0.3 μm bottom and a 0.1 μm cap $Zn_xCd_{1-x}Se$ layers. The growth rate and doping concentration were determined from separate calibration layers. These layers were also grown to optimize the growth conditions.

7.2 Material quality

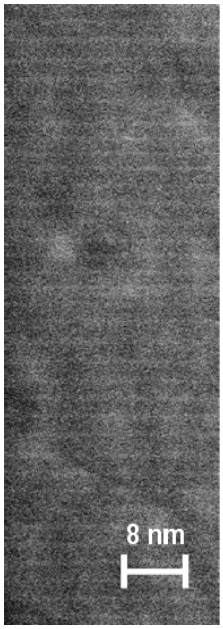

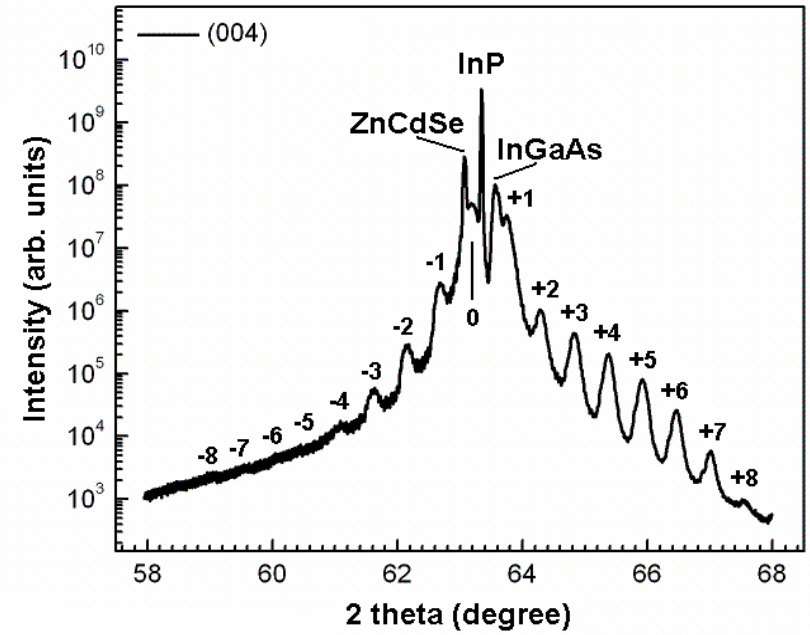

Figure 7.2 Cross-section SEM image of sample C.

Figure 7.3 HR-XRD curve of MQW sample C.

The samples were characterized by SEM, high resolution XRD (HR-XRD), PL measurements. Cross-section SEM images were taken to demonstrate the layer structure and interfacial property. Figure 7.2 is a SEM image taken on the cross-sectional edge of sample C. Clear and abrupt interfaces are observed

indicating the good control of the layered growth.

The XRD results indicate the excellent structural quality of the samples, as shown in Fig. 7.3, the HR-XRD curve of sample C. Up to 8^{th} order satellite peaks were observed due to the superlattice structure.

PL measurements were carried out at 77 K and room-temperature with the UV line (325 nm) of a He-Cd laser as the excitation source. Figure 7.4 shows the PL spectra of the four samples at 77 K. Sharp peaks from the MQWs can be seen from all of them with no traces of any deep level emissions. The full widths at half maximum (FWHM) of the PL emission peaks of these samples are around 40 meV regardless of how many repeats were grown, an evidence of excellent material quality. As shown in Fig. 7.5, a well-behaved quantum shift is observed, as the PL emission moves to higher energy with the decrease of well width. In Fig. 7.5, the solid line is the calculated transition energy as a function of well width, based on the envelope function approximation. Excellent agreement between the calculated transition energies and the experimental results is observed. In the calculations we assumed that Q_C = 0.80 determined in our previous study,[104] where $Q_C = \Delta E_C / \Delta E_g$ is the fraction of the bandgap difference ΔE_g that is in the conduction band. The band gaps of the $Zn_{x'}Cd_{y'}Mg_{1-x'-y'}Se$ barrier and the $Zn_xCd_{1-x}Se$ well were determined from calibration layers. The calculation of the effective masses was carried out in the same way that was described in Ref. 104. The PL data is summarized in Table V.

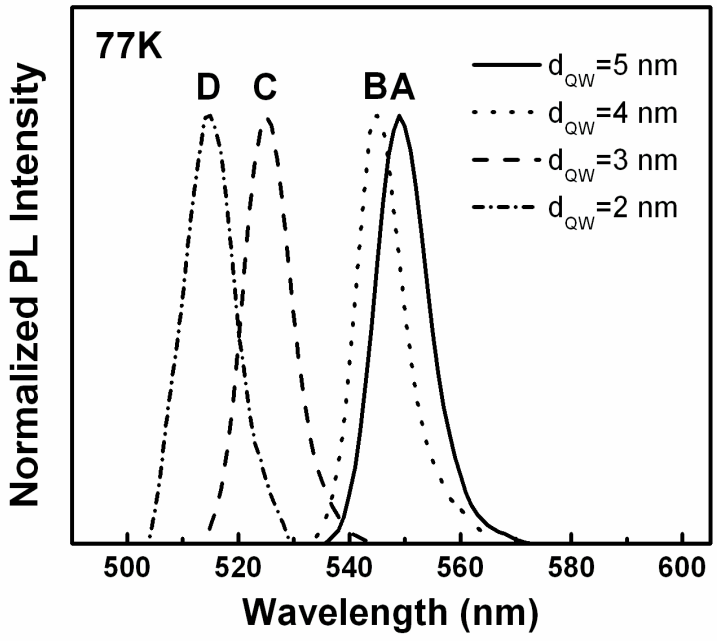

Figure 7.4 PL spectra of the MQW samples at 77K.

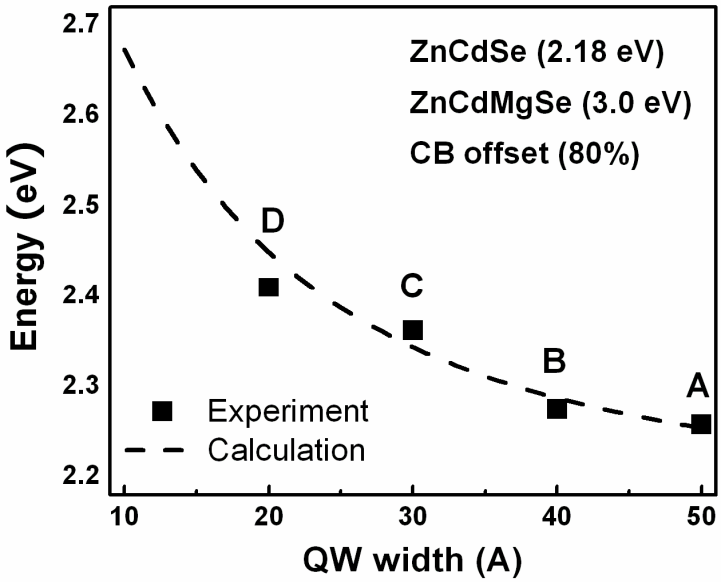

Figure 7.5 Theoretical calculation of band-to-band transition energy as a function of QW width. The bandgaps of ZnCdSe (QW) and ZnCdMgSe (barrier) were obtained from separate PL measurements.

7.3 Intersubband absorption studies

Fourier transform infrared (FT-IR) spectroscopy was used to measure the ISB absorption. Before performing the FTIR measurement on the sample, we must take care of several issues. First of all, the ISB absorption is a relatively weak signal due to the small amount of material (QW layers only) that is doped and thus responds to the incident light. Second, the normal incidence light (with the electric field parallel to the sample surface) does not produce any absorption due to the selection rules, as illustrated in Fig. 7.6 and discussed in the section below.

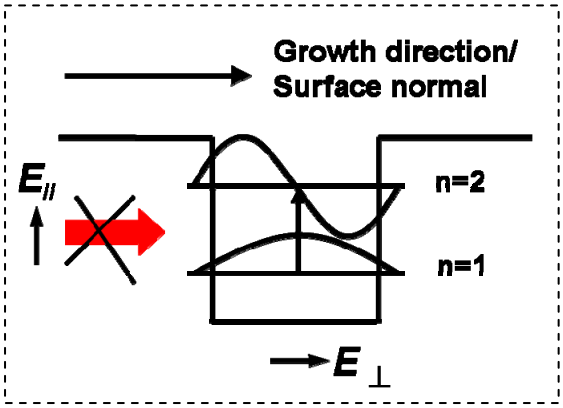

Figure 7.6 Schematic diagram of a QW's conduction band structure. Only the light with a portion of electric field in the surface normal direction will produce ISB absorption.

7.3.1 Intersubband absorption selection rules

Intersubband absorption results from transitions between energy levels within the same conduction or valence band. These levels arise from the spatial

localization introduced in quantum wells. Assuming infinitely high barrier and parabolic bands, the energy levels in the well are simply given by[105]

$$E_j = (\frac{\hbar^2 \pi^2}{2m^* L_w^2}) j^2 , \tag{7.1}$$

where L_w is the width of the quantum well, m^* is the effective mass in the well, and j is an integer. The ISB transition energy between the lowest and first excited state is thus

$$(E_2 - E_1) = (3\hbar^2 \pi^2 / 2m^* L_w^2) . \tag{7.2}$$

Furthermore this transition has a large dipole matrix element $\langle z \rangle = 16L/9\pi^2 \cong 0.18L_w$ and an integrated absorption strength of

$$\int_0^\infty \alpha(\nu) d\nu = (\frac{\rho_c N_w e^2 hf}{4\varepsilon_0 m^* c n_r})(\frac{\sin^2 \theta'}{\cos \theta'}) , \tag{7.3}$$

where $\rho_c = N_D L_w$ is the two-dimensional density of carriers in the well, N_D is the three-dimensional carrier density, N_w is the number of doped wells, n_r is the index of refraction, θ' is the angle between the direction of the optical beam and the surface normal (inside the medium), and f is the oscillator strength. This oscillator strength is very large (near unity) and is given for this quantum well with infinitely high barriers as[105]

$$f \equiv \frac{2m^*}{\hbar^2}(E_2 - E_1)\langle z \rangle^2 = \frac{256}{27\pi^2} \cong 0.96 \tag{7.4}$$

where z is the direction normal to the quantum well. The oscillator strength has the feature of being independent of the quantum well width. The same expression for the oscillator strength can be obtained by using the dipole matrix

element

$$\left|\langle 1|z|2\rangle\right| = \frac{16L}{9\pi^2} \tag{7.5}$$

It is even possible to derive a general expression for all allowed transitions in an infinite quantum well:

$$f_{mn} = \frac{64}{\pi^2}\frac{n^2 m^2}{(n^2 - m^2)^3} \tag{7.6}$$

Only parity changing (odd-even or even-odd) transitions are allowed due to the inversion symmetry of the potential. As further examples, f_{14} = 0.03, f_{23} = 1.87, and so on. Thus, we see that by far the strongest transition is the one with n = m + 1. The higher ones carry a smaller and smaller oscillator strength. We can also see that transitions between excited states are much stronger than transitions from the ground state, a fact well known from atomic physics and necessary to fulfill the oscillator sum rule. For large n, it can actually be shown using Eq. (7.6) that $f_{n,n+1}$ increases linearly with n.

Thus, by changing the quantum well width L_w this ISB transition energy can be varied over a wide range from the short-wave infrared (IR) (λ ~ 2 μm), the mid-wave IR (λ ~ 4 μm), through long-wave IR (λ ~ 10 μm) and into the very long-wave IR spectral regions (λ ~ 14 μm).

It should be noted from Eqs. (7.3) and (7.4) that since the oscillator strength only has a component along z, the optical electric field must also have a component parallel to z in order to induce an ISB absorption; thus, normal

incidence radiation [i.e., θ' = 0 in Eq. (7.3)] will not be absorbed. For this reason, West and Eglash[105] used a Brewster's angle geometry in order to give a large component of the optical electric field along the growth direction. Levine et al.[106] by using a multiple-pass waveguide geometry increased the net ISB absorption, thus permitting accurate measurements of the oscillator strength, the polarization selection rule, and the line shape even for single quantum wells.[107,108,109] The polarization selection rule $\alpha \propto \cos^2 \phi$ (where ϕ is the angle between the electric field and the z direction) was found to approximately hold where the absorption vanishes at ϕ = 90° (i.e., for light polarized in the plane of the quantum wells).

7.3.2 Sample preparation

In our FTIR measurements, the multiple-pass waveguide geometry with parallel 45-degree facets (see Fig. 7.7) was used to ensure enough ISB absorption signal. The sample preparation, which consists of three parts: backside indium (In) removal, backside surface polishing, and 45-degree sides polishing, is critical to have good ISB absorption measurements.

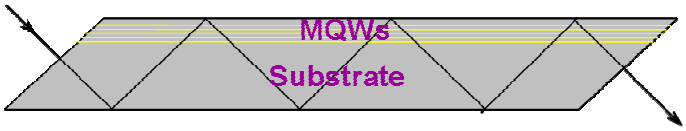

Figure 7.7 Schematic illustration of the multiple-pass waveguide geometry with 45° facets used in FTIR measurement. The MQWs region indicates the epilayers grown on top of the substrate.

The sample surfaces have to be smooth enough to prevent IR light scattering. For the MBE growth, all the samples were bonded to the molybdenum blocks using In, a soft metal, which is hard to remove by polishing. A saturated chemical solution, dissolving mercury chloride ($HgCl_2$) in N, N-dimethylformamide (DMF) solvent, was used to remove the In from the backside of the sample. During the procedure, the front surface (where the MQW structure is) of the sample was covered by Crystalbond 509 (soluble in acetone) to protect it from contamination and damage. The In reacted with $HgCl_2$-DMF solution to form an insoluble precipitate and left a clean surface. Ultrasonic can be used to expedite the procedure.

After the sample was cleaned by acetone and methanol, it was bonded to a metallic block for polishing. Polishing films (with alumina or diamond particles) with different roughness (3 micron, 1 micron, 0.5 micron, etc.) were chosen from the rougher one to the finer one for step-by-step polishing procedure. The size of the finest polishing film used depends on our interest wavelength range for absorption measurements, for the reason that the roughness of the sample surface has to be smaller than the wavelength of the incident light to minimize the loss on the surface. Water or methanol was used as lubricant to moisturize the polishing film surface. The sample surface should look shinny and smooth after polishing.

The same procedure was used for the two 45-degree facets polishing

except for using a different metallic block with a 45-degree angle shape. Finally, the multiple-pass waveguide geometry was achieved on the sample as shown in Fig. 7.7.

7.3.3 Room temperature FTIR measurements

The absorption measurements were performed at RT using a Nicolet Nexus-870 FTIR spectrometer. A liquid-nitrogen (LN_2) cooled HgCdTe detector was used for best detectivity.

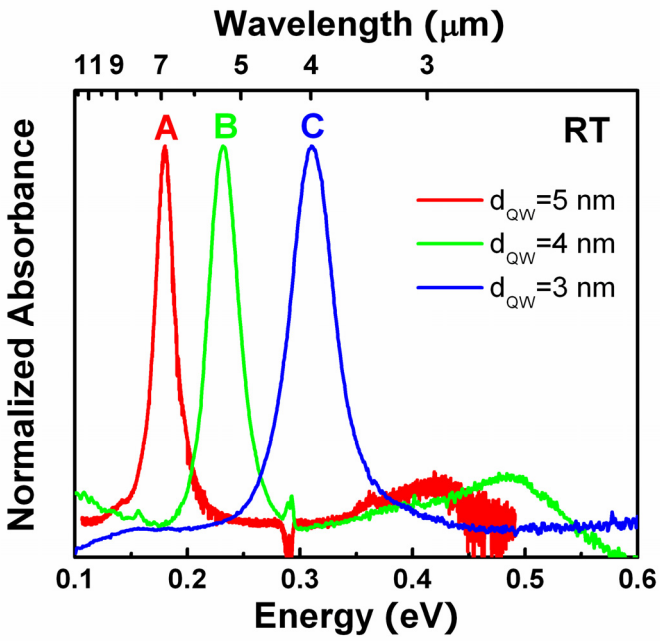

Figure 7.8 Normalized absorbance due to ISB transitions of MQW samples A, B and C measured at RT. The absorbance is obtained by taking the ratio of the P-polarized spectra over the S-polarized spectra.

Figure 7.8 shows the normalized absorbance of the samples at room temperature. The spectra were obtained by taking the ratio of the P-polarized spectrum over the S-polarized spectrum. For samples (A, B and C) with different well widths from 5 to 3 nm, peak absorption λ_p were observed at 6.88 μm (0.18 eV), 5.35 μm (0.23 eV) and 3.99 μm (0.31 eV), respectively. Fitting by a Gaussian line shape gives the FWHM (ΔE) values of 21 meV, 30 meV and 46 meV for the three samples. The value of $\Delta E / E_{peak}$ is of the order 10% to 20%, which is typical for a bound-to-bound transition and comparable to the values obtained for the well-studied III-V semiconductors.[110] For samples A and B, a second, weaker absorption peak is seen at higher energy side. We tentatively attribute this peak to the bound-to-continuum absorption in the well, but additional work is needed to confirm this assignment.

The peak absorption wavelength as a function of QW width was plotted in Fig. 7.9. The lines are the theoretical curves obtained from the envelope function approximation calculation for slightly different values of Qc. The values of the bandgaps of the barrier and the well used in the calculation were obtained from the 77 K PL emission of the calibration layers. A 70 meV correction is made to obtain the room-temperature values. The experimental data are in good agreement with the predicted values within the range of Qc. It is also found that bound-to-bound ISB absorption is weakly dependent on the band offset. Then we expect that sample D with a thinner QW width will push the absorption peak to a

shorter wavelength.

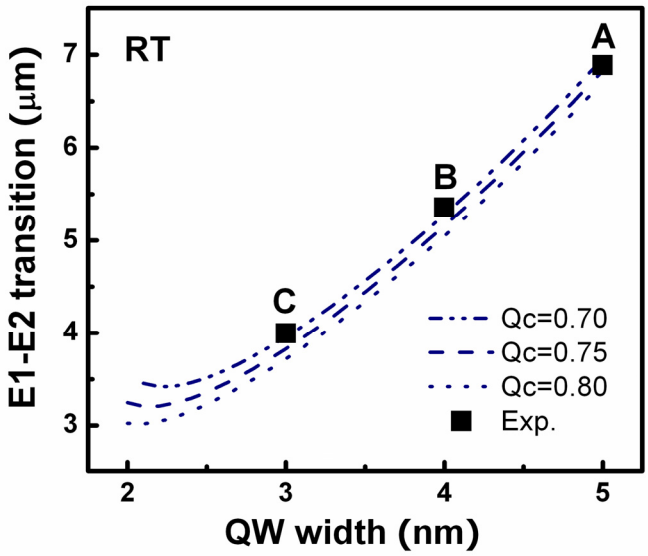

Figure 7.9 The E1-E2 ISB transition in wavelength as a function of QW width. The calculation is done based on three different Q_C ($\Delta E_C/\Delta Eg$) values.

The solid orange line shown in Fig. 7.10 is the absorption of sample D. Instead of moving the absorption peak to a shorter wavelength position, the peak was observed at 4.43 μm (0.28 eV). The absorption peak is much wider ($\Delta E/E_{peak}$ = 32%) than those of the other three samples and has an asymmetric shape with a tail at the higher energy side. With all these characteristics being typical of bound-to-continuum transition, we attribute the unexpected shift to the higher level of the lower energy state within the well, coupled with the limited barrier height. With a bandgap of 2.9 eV, the barrier is not high enough anymore to confine the second level in the QW with a width of 2 nm.

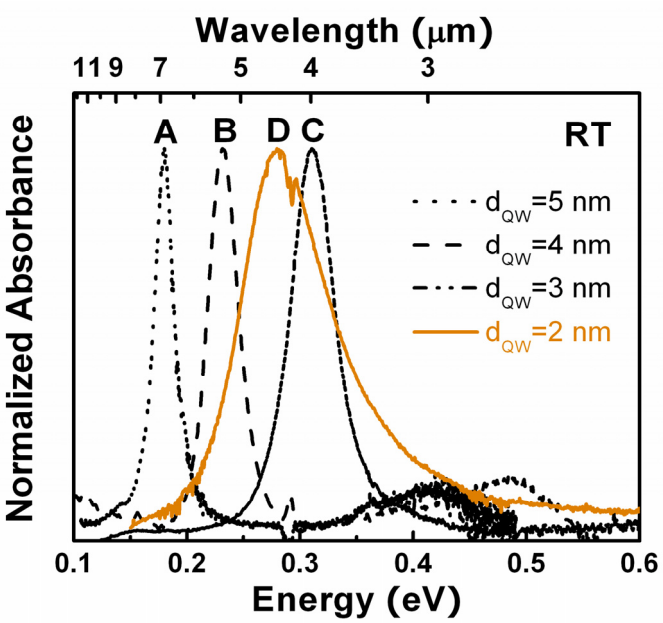

Figure 7.10 The ISB absorption of sample D with a thinner QW width (orange solid line). The ISB absorption of samples A, B and C are also shown for comparison. A different ISB transition mechanism for sample D is demonstrated.

Table V. Interband and intersubband transitions data for samples A, B, C and D.

Sample	A	B	C	D
QW width (nm)	5	4	3	2
PL emission (eV)	2.258	2.275	2.362	2.407
FWHM (meV)	41	42	40	45
ISB absorption λ_{peak}	6.88	5.35	3.99	4.43
(μm) & (meV)	180	231	310	280
FWHM (meV)	21	30	46	89
$\Delta E/E_{peak}$ (%)	12	14	15	32
ISB type	B-B	B-B	B-B	B-C

The results suggest that for the barrier composition used in this study it would be difficult to achieve shorter wavelength by simply reducing the QW width. Further reduction of the absorption wavelength should be possible if a wider bandgap barrier layer is used. A maximum bandgap of 3.6 eV can be obtained with this material system. Also, the use of strain compensated structures may result in even shorter wavelength devices.

7.3.4 Temperature dependent FTIR measurements

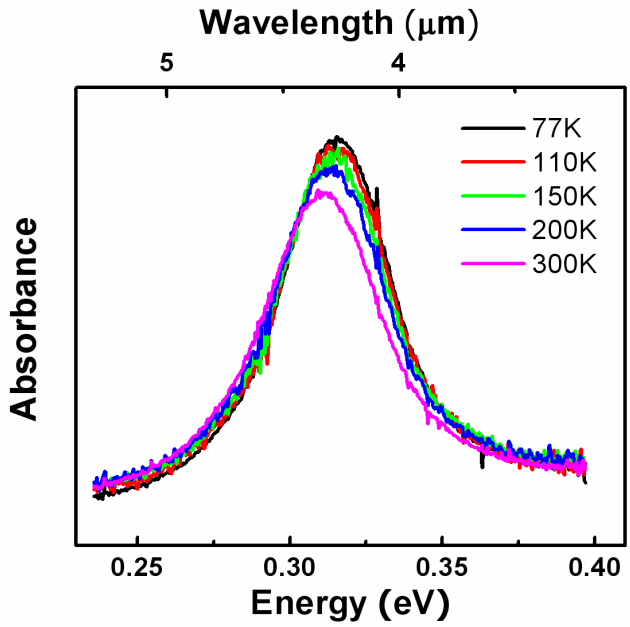

Figure 7.11 Temperature-dependent FTIR measurements of sample C with the temperature varying from 77K to 300K.

Temperature dependent FTIR measurements were performed on sample C. Since the ISB absorption of sample C occurs at ~ 4 μm, a LN_2 cooled InSb detector was used due to its good performance in the wavelength range of 2 ~ 5

μm. As the temperature decreases from room temperature to 77 K, the intensity, position, and FWHM of the absorption peak had observable changes, as shown in Fig. 7.11, Fig. 7.12 (a) and (b).

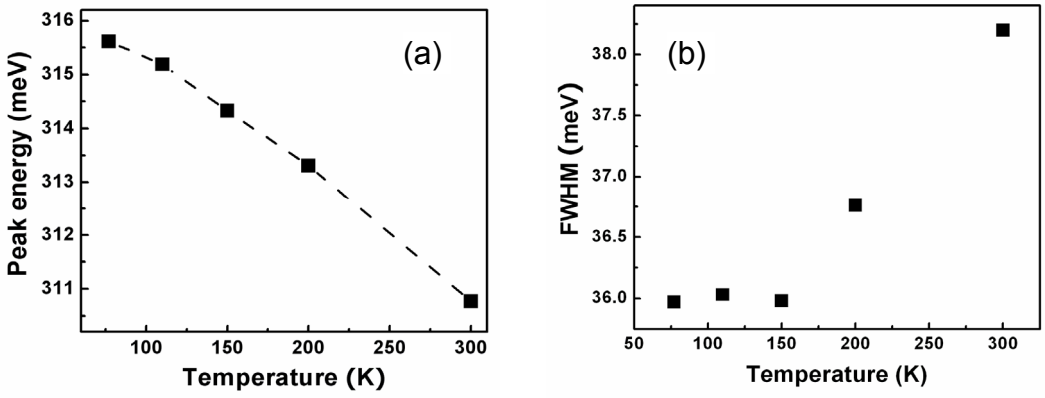

Figure 7.12 Changes of the peak energy (a) and FWHM (b) of ISB absorption from sample C as the temperature varying from 77K to 300K.

According to the similar work of Allenman and Covington et al., there are expected shifts in the peak wavelength and linewidth with temperature.[111,112] As the temperature is lowered from room temperature down to cryogenic temperatures, there is a small ($\Delta\nu$ ~3%) decrease in the peak wavelength and also a decrease in the linewidth $\Delta\nu$. However, the oscillator strength remains constant so that the reduction in $\Delta\nu$ (~ 75% of the room temperature value) is accompanied by an increase in the peak absorption[113] (by a factor ~ 1.3).

The results of sample C exhibit a trend following similar work on III-V materials. A small increase of ~1.6% in the peak energy (reduction in peak

wavelength) and an increase of ~1.23 in the peak intensity are obtained as the temperature decreases. Compared to band-to-band transitions, ISB transitions are less sensitive to the temperature, thus, making devices based on ISB transitions more stable under circumstance of varying temperature.

Conclusion

In conclusion, we report the observation of ISB transitions in wide bandgap $Zn_{0.46}Cd_{0.54}Se/Zn_{0.25}Cd_{0.25}Mg_{0.50}Se$ MQWs grown on InP substrates by MBE. The experimental data are in good agreement with theoretical predictions. By further decreasing the well width and increasing the bandgap of the $Zn_{x'}Cd_{y'}Mg_{1-x'-y'}Se$ barrier layer, ISB transitions at even shorter wavelength are expected. These results indicate that $Zn_xCd_{1-x}Se/Zn_{x'}Cd_{y'}Mg_{1-x'-y'}Se$ is a very promising material system for ISB devices operating in the mid-infrared spectral range between 3 and 5 μm.

Chapter 8

Summary and future directions

8.1 Summary of current work

As we proposed in Chapter 2, we have performed a series of studies on quantum well structures based on the $Zn_xCd_{1-x}Se/Zn_{x'}Cd_{y'}Mg_{1-x'-y'}Se$ material system and successfully demonstrated the potential of this II-VI system for fabricating mid-IR intersubband devices with shorter wavelengths and higher operating temperatures than currently available. The contributions of this work can be summarized as following.

Using contactless electroreflectance (CER) and the envelope function approximation (EFA) we have determined that the CBO of $Zn_xCd_{1-x}Se/Zn_{x'}Cd_{y'}Mg_{1-x'-y'}Se$ based heterostructure is ~80% of the total band offset. The determination of the CBO is essential for guiding the device structure design. In addition, this large band offset confirms that this system may be a good candidate for mid-infrared ISB device applications.

Using the available CBO value, a series of $Zn_xCd_{1-x}Se/Zn_{x'}Cd_{y'}Mg_{1-x'-y'}Se$ QWIP structures for device applications in the mid-IR wavelength range have been designed and grown. Excellent material quality has been achieved. Time-

resolved PL studies indicate that the transitions are dominated by radiative recombination.

The contactless electroreflectance (CER) method has been developed and applied on $Zn_xCd_{1-x}Se/Zn_{x'}Cd_{y'}Mg_{1-x'-y'}Se$ MQW structures for ISB transition studies. Multiple QW transitions could be readily observed and identified by the EFA. The excellent agreement between the CER and FTIR results demonstrates that we can predict the ISB transition wavelength accurately by this non-destructive technique.

Intersubband absorption studies were performed by FTIR measurements. Bound-to-bound and bound-to-continuum transitions in the range of 4~7μm were observed for structures with different QW widths. Shorter wavelength can be realized by introducing a larger confinement, either by increasing the barrier height or introducing strain into the QW layers (thus, reducing the QW bandgap).

8.2 Future directions

As stated previously, the identification of this near lattice-matched II-VI system with large CBO and strong and well-behaved ISB absorption in the mid-IR, may yield practical alternatives for the design of these complex device structures. Future directions for this work involve investigations of device design, optimization and fabrication. Below I will describe some preliminary steps we

have taken to pursue the design and fabrication of quantum cascade lasers from our materials.

8.2.1 QCLs structure design

A QCL structure consists of a repetition of a number of identical stages. Each stage consists of an active region followed by a relaxation-injection region (injector). The design of QCL is performed by quantum engineering of the electronic energy levels, wavefunctions, matrix elements and scattering rates to design population inversion and optimize laser gain and overall performance.

There are three types of transitions typically used in the QCLs: diagonal (interwell) transition[29,36] where the optical transition occurs between different levels in adjacent wells, vertical (intrawell) transition[37,38] where the optical transition occurs between different levels in the same well, and interminiband transition[39,40,41] where the optical transition occurs between different levels formed by miniband in “chirp” superlattices. Figure 8.1 shows the band diagram of an active region that relies on vertical transitions. An electron injected into the level 3 relaxes to level 2 and emits a photon with energy $h\nu = E_3 - E_2$. To ensure the population inversion between level 3 and level 2, the carrier lifetime at level 2 must be smaller than that of level 3 scattering into level 2. This is achieved by designing the structure so that the energy level difference between level 2 and

level 1, $E_2 - E_1$, is in resonance with one LO phonon energy.

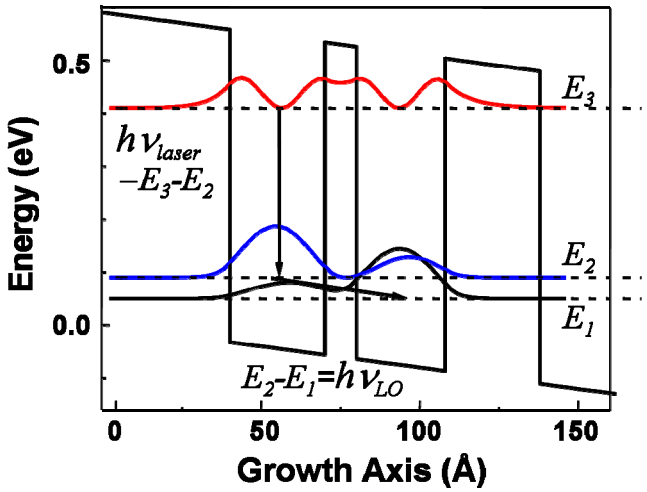

Figure 8.1 Conduction band diagram of the active region of a QCL structure. Three energy levels in a coupled QW structure are used to realize vertical transition and population inversion.

For realizing a QCL, we propose to concentrate on the design and investigation of:

1) Single active region with coupled quantum wells. As shown in Fig. 8.1, the coupled QW active regions provide the desired 3-level systems for efficient ISB emission. The materials will be investigated by PL, CER, and FTIR. The structures will be used to study the effect of barrier thickness on the coupling between adjacent wells.

2) Injectors. The injector region is the section where the electrons cool down and are re-injected into the next active region. This region must be doped

to prevent the strong space charge buildup. The doping is usually restricted to the center of the injector to separate electrons in the ground state from the parent donors. This helps to reduce electron scattering and thus increases injection efficiency. The injectors will be designed to minimize the carrier thermal backfilling so as to ensure the high temperature operation of the device. Doping and transport properties of the injector layers will be investigated and optimized. Simulations and modeling will be used to assist with the experimental work.

3) Proto-type QCL structure. Our first step to observe the cascade carrier transport and intersubband photon emission in a QCL structure is to measure the intersubband electroluminescence (EL). A first attempt to design a sample for EL measurements was made by our collaborators at Princeton (ERC-MIRTHE), applying their modeling techniques to these novel materials. The anticipated EL emission for this structure is about 4.5 μm. Using the proposed band structure of this EL sample, shown in Fig. 8.2, they also modeled the absorption structures that had already been grown and measured. The agreement between experiment and theory was excellent, indicating that the program is good for modeling the II-VI materials.

We propose to grow this EL structure, the core of a QCL, to demonstrate the feasibility of the proposed device. Electroluminescence will be studied. The study may lead the way towards the final success of a practical working QCL device.

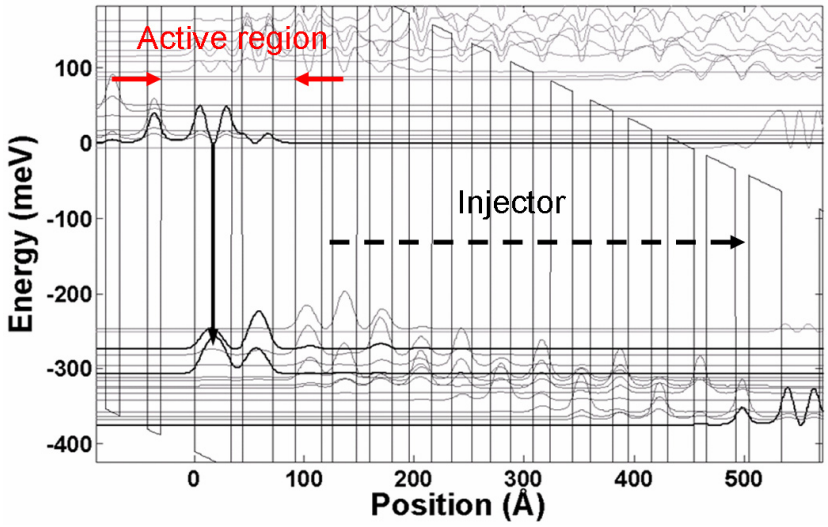

Figure 8.2 Band structure of a quantum cascade electroluminescence structure.

8.2.2 Device processing

To achieve real devices the device fabrication process must also be investigated. Some preliminary work on device processing has been done at the nanofabrication of Pennsylvania State University. The entire processing procedure can be divided into five parts, as illustrated in Fig. 8.3. A cycle of a typical silicon lithography procedure would begin by depositing a layer of conductive metal several nanometers thick on the substrate.

A. Sample and shadow mask preparation

The sample, which is the device structure grown by MBE, must be cleaned with acetone and methanol to obtain an organic-free surface. The shadow mask is designed according to our study of interest, and made by techniques such as E-beam or laser printing.

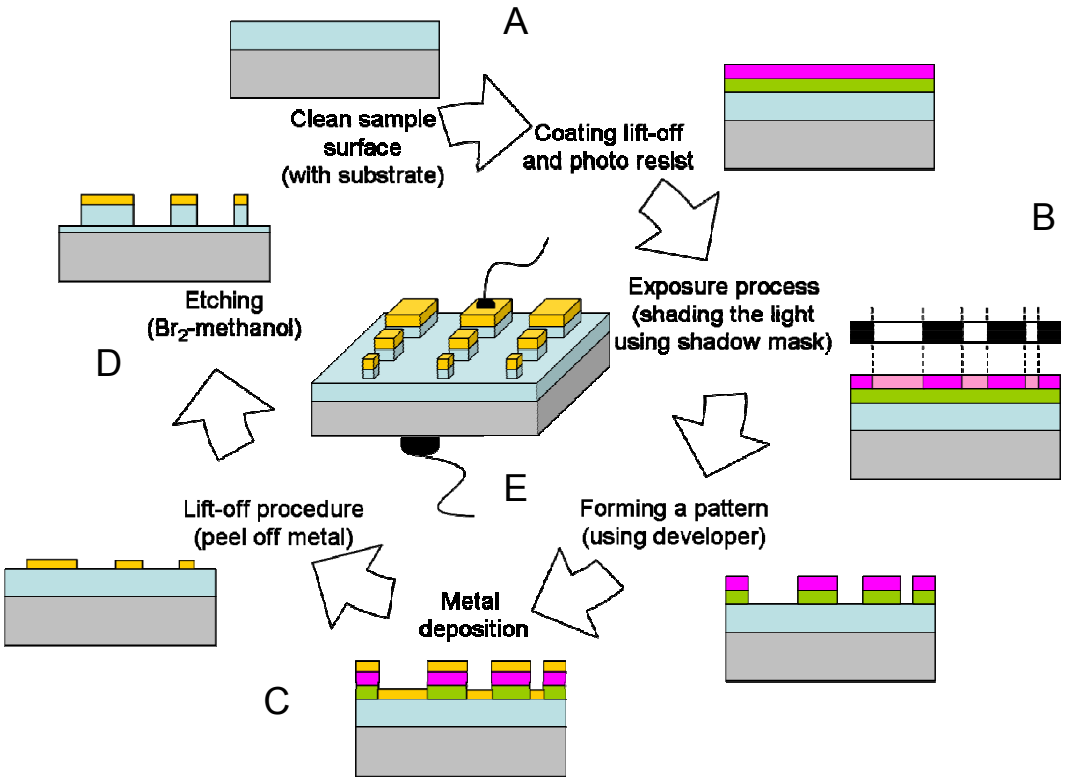

Figure 8.3 Illustration of device processing procedure.

B. Photolithography

Photolithography is a process used in semiconductor device fabrication to transfer a pattern from a shadow mask to the surface of a substrate. Photolithography bears a similarity to the conventional lithography used in printing and shares some of the fundamental principles of photographic processes. Photolithography involves a combination of: i) Coating liftoff and photoresist deposition; ii) Exposure; iii) Developing.

There are two types of photoresist, termed positive and negative. Where the ultraviolet light strikes the positive resist it weakens the resist, so that when the image is developed the resist is washed away where the light struck it transferring a positive image of the mask to the resist layer. The opposite occurs with negative resist, the resist that was not exposed to ultraviolet light is washed away, and a negative image of the mask is transferred to the resist. A layer liftoff is used for peeling off the metal layer efficiently in future steps.

In our trials, a positive photoresist was used and the surface was exposed to the 365nm line of a UV light source for a few seconds. Then the pattern was formed after washing the weakened photoresist away using a developer.

C. Metal layer deposition

The sample surface was cleaned with oxygen plasma for 1-2 minutes before depositing a metal layer. A layer (150 Å) of Chromium was deposited first to improve the adhesion of metal layer to the sample surface. Then a thick layer (~2000 Å) of gold was deposited as the metal contact layer for further measurements. The undesired metal layer was peeled off through a lift-off procedure. Our desired pattern with a layer of metal contact was obtained.

D. Etching

For this II-VI system, we used Bromine-methanol solution (< 0.1%) to etch off the material, therefore forming individual microchips. A profilometer was used to measure the actual depth after etching.

Good control of all the above steps can be demonstrated by images taken by optical microscope and SEM, shown in Fig. 8.4.

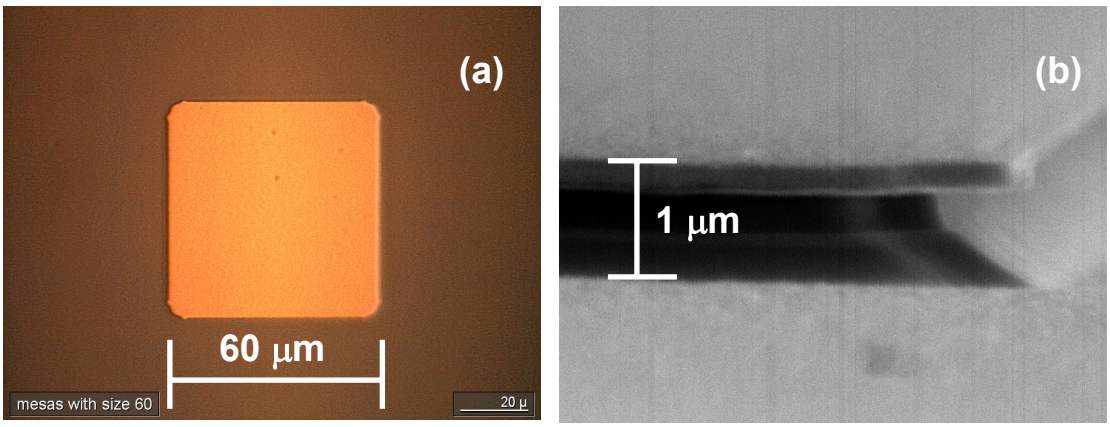

Figure 8.4 Images of device microchips. (a) Top view by optical microscope. (b) Side view by cross-section SEM image.

E. Wire bonding

Wire bonding is a method of making interconnections between a microchip and the outside world as part of semiconductor device fabrication. Then the desired measurements on these microchips (a 3D image is shown in the center of Fig. 8.3 as the final product) are ready to proceed.

Publications

Journal Papers

- Study of intersubband transitions in $Zn_xCd_{1-x}Se/Zn_{x'}Cd_{y'}Mg_{1-x'-y'}Se$ multiple quantum wells grown by molecular beam epitaxy for mid-infrared device applications, submitted to *J. Vac. Sci. Technol.*

  H. Lu, A. Shen, M. C. Tamargo, M. Muñoz et al.

- Intersubband transitions in MBE-grown wide bandgap II-VI semiconductors, submitted to *J. Vac. Sci. Technol.*

  A. Shen, **H. Lu**, M. C. Tamargo, W. Charles, I. Yokomizo, C. Y. Song, H. C. Liu et al.

- Intersubband absorption in $CdSe/Zn_xCd_yMg_{1-x-y}Se$ self-assembled quantum dots multi-layers, to be published in *Appl. Phys. Lett.*

  A. Shen, **H. Lu,** W. Charles, I. Yokomizo, M. C. Tamargo, K. J. Franz, C. Gmachl, S. K. Zhang, X. Zhou, R. R. Alfano and H. C. Liu.

- Radiative and nonradiative recombination processes in ZnCdSe/ZnCdMgSe multi-quantum wells, *J. Appl. Phys*, 101, January (2007).

  S. K. Zhang, **H. Lu**, W. B. Wang, B. B. Das, N. Okoye, M. C. Tamargo and R. R. Alfano

- Optical characterization of intersubband transitions in $Zn_xCd_{1-x}Se/Zn_{x'}Cd_{y'}Mg_{1-x'-y'}Se$ multiple quantum well structures by contact-less electroreflectance, *Appl. Phys. Lett.*, 89, 241921 (2006).

  H. Lu, A. Shen, W. Charles, I. Yokomizo, M. Muñoz, K. Franz, C. Gmachl and M. C. Tamargo

- Mid-infrared intersubband absorption in $Zn_xCd_{1-x}Se/Zn_{x'}Cd_{y'}Mg_{1-x'-y'}Se$ multiple quantum well structures, *Appl. Phys. Lett.*. 89, 131903 (2006).

  H. Lu, A. Shen, C. Y. Song, H. C. Liu, S. K. Zhang, R. R. Alfano, M. Muñoz and M. C. Tamargo

- $Zn_xCd_{(1-x)}Se/Zn_{x'}Cd_{y'}Mg_{(1-x'-y')}Se$ multi-quantum well structures for intersubband devices grown by MBE, *Phys. Stat. Sol.* (b) 243 (4), 868 (2006).

  H. Lu, A. Shen, M. Muñoz, M. N. Perez-Paz, M. Sohel, S. K. Zhang, R. R. Alfano and M. C. Tamargo

- Formation and optical properties of stacked CdSe self-assembled quantum dots on $Zn_xCd_yMg_{1-x-y}Se$ barriers, *J. Vac. Sci. Technol.* B 24 (3), 1649 (2006).

  M. Noemi Perez-Paz, **Hong Lu**, Aidong Shen and Maria C. Tamargo

- Magnesium effects on CdSe self-assembled quantum dot formation on $Zn_xCd_yMg_{(1-x-y)}Se$ layers, *J. Crystal Growth.* 294, 296 (2006).

M. Noemi Perez-Paz, **Hong Lu**, Aidong Shen, F. Jean Mary, Daniel Akins and Maria C. Tamargo

- Hanle effect measurements of spin lifetime in $Zn_{0.4}Cd_{0.6}Se$ epilayers grown on InP, *J. Superconductivity: Incoporation Novel Magnetism***,** 18, 195 (2005).

  O. Maksimov, **H. Lu**, M. Muñoz, M. C. Tamargo and N. Samarth

- Optical characterization and evaluation of the conduction band offset for ZnCdSe/ZnMgSe quantum wells grown on InP(001) by Molecular Beam Epitaxy, *J. Vac. Sci. Technol.* B 23(3), 1209 (2005).

  Mohammad Sohel, Xuecong Zhou, **Hong Lu**, M. Noemi Perez-Paz, Maria C. Tamargo and Martin Muñoz

- Single layer and stacked CdSe self-assembled quantum dots with ZnCdMgSe barriers for visible and white light emitters, *J. Vac. Sci. Technol.* B 23(3), 1236 (2005).

  M. Noemi Perez Paz, Xuecong Zhou, Martin Muñoz, Mohammad Sohel, **Hong Lu**, Francisco Fernandez and Maria C. Tamargo

- Contactless electroreflectance studies of II-VI nanostructures grown by Molecular Beam Epitaxy, *Phys. Stat. Sol. (b)* 241, 546 (2004).

  Martin Muñoz, **Hong Lu**, Shiping Guo, Xuecong Zhou, Maria C. Tamargo, Fred H. Pollak, Y. S. Huang, C. Trallero-Giner and A. H. Rodriguez

- Efficient free exciton emission at room temperature in $Zn_{0.5}Cd_{0.5}Se/Mg_xZn_yCd_{1-x-y}Se$ quantum wells, *Solid State Communications,* 132, 1 (2004).

  O, Maksimov, N. Samarth, **H. Lu**, M. Muñoz and M. C. Tamargo

- CdSe self-assembled quantum dots with ZnCdMgSe barriers emitting throughout the visible spectrum, *Appl. Phys. Lett.,* 85, 6395 (2004).

  M. Noemi Perez-Paz, Xuecong Zhou, Martin Muñoz, **Hong Lu**, Mohammad Sohel and Maria C. Tamargo

- Band offset determination of $Zn_{0.53}Cd_{0.47}Se/Zn_{0.29}Cd_{0.24}Mg_{0.47}Se$, *Appl. Phys. Lett.*, 83, 1995 (2003).

  Martin Muñoz, **Hong Lu**, Xuecong Zhou and Maria C. Tamargo

Conference Presentations

- "Contact-less electroreflectance study of intersubband transitions in ZnCdSe/ZnCdMgSe multiple quantum wells grown by MBE", *24th North American Conference on Molecular Beam Epitaxy*, Durham, NC, 2006

  H. Lu, A. Shen, M. C. Tamargo, M. Muñoz et al.

- "Intersubband transitions in MBE-grown wide bandgap II-VI semiconductors", *24th North American Conference on Molecular Beam Epitaxy*, Durham, NC, 2006

Shen, **H. Lu**, M. C. Tamargo, W. Charles, I. Yokomizo, C. Y. Song, H. C. Liu et al.

- "MBE-grown wide bandgap II-VI nanostructures for intersubband devices", *14th International Conference on Molecular Beam Epitaxy,* Tokyo, Japan, September 3-8, 2006

  Maria C. Tamargo, **H. Lu**, A. Shen et al.

- "MBE-grown $Zn_xCd_{(1-x)}Se/Zn_{x'}Cd_{y'}Mg_{(1-x'-y')}Se$ multi-quantum wells for intersubband devices", *48th Electronic Materials Conference*, University Park, PA, June 28-30, 2006

  H. Lu, A. Shen, S. K. Zhang, R. R. Alfano, C. Y. Song, H. C. Liu and M. C. Tamargo

- "MBE-grown $Zn_xCd_{1-x}Se/Zn_{x'}Cd_{y'}Mg_{1-x'-y'}Se$ multi-quantum wells for mid-infrared intersubband devices", *Junior Scientist Conference 2006*, Vienna University of Technology, Austria, April 19-21, 2006

  Hong Lu and Maria C. Tamargo

- "Study of intersubband transitions in ZnCdSe/ZnCdMgSe quantum well structures by Molecular Beam Epitaxy", *23rd North American Conference on Molecular Beam Epitaxy*, Santa Barbara, CA, 2005

  H. Lu, M. N. Perez-Paz, A. Shen, M. Sohel, S. K. Zhang, R. R. Alfano, M. C. Tamargo

- "Single and stacked CdSe self-assembled quantum dots on ZnCdMgSe barriers: formation and optical properties", *23nd North American Conference on Molecular Beam Epitaxy*, Santa Barbara, CA, 2005

  M. N. Perez-Paz, **H.Lu**, M. Sohel, A. Shen, M. C. Tamargo

- "Study of ZnCdSe/ZnCdMgSe multi-quantum well structures prepared by Molecular Beam Epitaxy", *12th International Conference on II-VI Compounds*, Warsaw, Poland, 2005

  H. Lu, M. N. Perez-Paz, M. Sohel, A. Shen, X. Zhou, M. C. Tamargo, S. K. Zhang and R. R. Alfano.

- "Growth and vertical correlation of CdSe stacked quantum dots on ZnCdMgSe barriers varying spacer thickness and Mg content", *12th International Conference on II-VI Compounds*, Warsaw, Poland, 2005

  M. N. Perez-Paz, **H. Lu**, X. Zhou, M. Sohel, A. Shen and M. C. Tamargo

- "Wide bandgap ZnMgSe alloys and ZnCdSe/ZnMgSe quantum wells for intersubband devices", *12th International Conference on II-VI Compounds*, Warsaw, Poland, 2005

  M. Sohel, M. N. Perez-Paz, **H. Lu**, X. Zhou, M. Muñoz and M. C. Tamargo

- "Growth and characterization of ZnCdSe/ZnCdMgSe MQWs for infra-red opto-electronic applications", *16th American Conference of Crystal Growth and Epitaxy*, Big Sky, MT, 2005

  H. Lu, A. Shen, M. Sohel, M. N. Perez Paz, X. Zhou, S. K. Zhang, R. R. Alfano, M. C. Tamargo

- "Characterization of quantum well infra-red photodetector structures grown by MBE method", *Conference of "Einsteins in the City"*, New York, NY, 2005

  H. Lu, O. Othman, A. Shen, M. N. Perez-Paz, M. Sohel, X. Zhou and M. C. Tamargo

- "Mg influence in the formation of CdSe self-assembled quantum dots with ZnCdMgSe barriers"*, March meeting of American Physical Society*, Los Angeles, CA, 2005

  M. N. Perez-Paz, **H.Lu**, M. Sohel, X. Zhou and M. C. Tamargo,

- "Band offset determination of $Zn_{0.53}Cd_{0.47}Se/Zn_{0.29}Cd_{0.24}Mg_{0.47}Se$"*, 11th International Conference on II-VI Compounds*, Niagara Falls, NY, 2003

  Martin Muñoz, **Hong Lu**, Xuecong Zhou, Maria C. Tamargo and Fred H. Pollak

- "Band offset determination of $Zn_{0.53}Cd_{0.47}Se/Zn_{0.29}Cd_{0.24}Mg_{0.47}Se$"*, March meeting of American Physical Society*, Austin, TX, 2003

Martin Muñoz, **Hong Lu**, Xuecong Zhou, Maria C. Tamargo and Fred H. Pollak

Bibliography

[1] H. C. Liu and F. Capasso, editors. *Intersubband Transitions in Quantum Wells: Physics and Device Applications I & II*, Semiconductors and Semimetals, volume 62 & 66 (Academic, San Diego, 2000).

[2] M. C. Tamargo, M. J. S. P. Brasil, R. E. Nahory, R. J. Martin, A. L. Weaver, and H. L. Gilchrist, Semicond. Sci. Technol. **6**, A8 (1991).

[3] M. C. Tamargo, A. Cavus, L. Zeng, N. Dai, N. Bambha, A. Gray, F. Semendy, W. Krystek and F. H. Pollak, in *Semiconductor Heteroepitaxy: Growth, Characterization and Device Applications,* edited by B. Gil and R. L. Aulombard, (World Scientific, 1995).

[4] M. C. Tamargo, W. Lin, S. P. Guo, Y. Luo, Y. Guo and Y. C. Chen, J. Crystal Growth **214/215**, 1058 (2000).

[5] Y. Guo, G. Aizin, Y. C. Chen, L. Zeng, A. Cavus, M. C. Tamargo, Appl. Phys. Lett. **70**, 1351 (1997).

[6] L. Zeng, Y. Guo, B. X. Yang, A. Cavus, W. Lin, Y. Y. Luo, Y. C. Chen and M. C. Tamargo, Appl. Phys. Lett. **72**, 3136 (1998).

[7] M. Muñoz, H. Lu, X. Zhou, M. C. Tamargo, and F. Pollak, Appl. Phys. Lett. **83**, 1995 (2003).

[8] M. Sohel, X. Zhou, H. Lu, M. N. Perez-Paz, M. Tamargo, and M. Muñoz, J. Vac.

Sci. Technol. B **23(3)**, 1209 (2005).

[9] A. Y. Cho, J. Vac. Sci. Technol. **8**, S31 (1971).

[10] G. J. Davies, R. Heckingbottom, H. Ohno, C. E. C. Wood, and A. R. Calawa, Appl. Phys. Lett. **37(3)**, 290 (1980).

[11] B.X. Yang, L. He and H. Hasegawa, J. Elect. Mater. **25**, 379 (1996).

[12] C. C. Chu, T. B. Ng, J. Han, G. C. Hua, R. L. Gunshor, E. Ho, E. L. Warlick, and L. A. Kolodziejski, Appl. Phys. Lett. **69(5)**, 602 (1996).

[13] Claire Gmachl, Federico Capasso, Deborah L. Sivco and Alfred Y. Cho, Rep. Prog. Phys. **64**, 1533 (2001).

[14] Jerome Faist, Federico Capasso, Deborah L. Sivco, Albert L. Hutchinson, Sung-Nee G. Chu, and Alfred Y. Cho, Appl. Phys. Lett. **72**, 680 (1998).

[15] Raffaele Colombelli, Federico Capasso, Claire Gmachl, Albert L. Hutchinson, Deborah L. Sivco, Alessandro Tredicucci, Michael C. Wanke, A. Michael Sergent, and Alfred Y. Cho, Appl. Phys. Lett. **78**, 2620 (2001).

[16] Jerome Faist, Federico Capasso, Deborah L. Sivco, Carlo Sirtori, Albert L. Hutchinson, Alfred Y. Cho, Science **264**, 553 (1994).

[17] Federico Capasso, Clarie Gmachl, Deborah L. Sivco, and Alfred Y. Cho, Physics Today May 2002, page 34.

[18] B. F. Levine, J. Appl. Phys. **74**, R1 (1993).

[19] F. Capasso et al., IEEE J. Sel. Top. Quantum Electron. **6**, 931 (2000).

[20] J. Ouellette, Ind. Physicist **7**, 8 (April 2000).

[21] C. Gmachl et al., IEEE Circuits Devices Mag. **16**, 10 (2000).

[22] C. Webster et al., Appl. Opt. **40**, 321 (2001).

[23] S. P. Guo and M. C. Tamargo, in: II-VI Semiconductor Materials and Their Applications, edited by M. C. Tamargo (Taylor and Francis, New York, 2002), pp. 261-286.

[24] D. Keith Bowen and Brian K. Tanner, "High Resolution X-ray Diffractometry and Topography", Taylor & Francis, 1998.

[25] A. Iida and K. Kohra, Phys. Stat. Sol. (a) **51**, 533 (1979).

[26] P. Zaumseil and U. Winter, Phys. Stat. Sol. (a) **70**, 497 (1982).

[27] H. Kim, S. J. Gotoh, T. Takahashi, T. Ishikawa and S. Kikuta, Nucl. Instr. And Meth. **A246**, 810 (1986).

[28] S. M. Sze, "Physics of Semiconductor Devices", 2nd Edition, John Wiley & Sons, New York (1981).

[29] D. L. Schroder, "Semiconductor Material and Device Characterization", John Wiley & Sons, New York (1990); L. J. van der Pauw, Phil. Res. Rep. 13, 1 (1958); L. J. van der Pauw, Phil. Tech. Rev. **20**, 220 (1958).

[30] Sidney Perkowitz, "Optical Characterization of Semiconductors: Infrared, Raman, and Photoluminescence Spectroscopy", Academic Press, (1993).

[31] J. Faist, F. Capasso, D. L. Sivco, C. Sirtori, A. L. Hutchinson, and A. Y. Cho,

Science **264**, 553 (1994).

[32] C. Gmachl, H. M. Ng, and A. Y. Cho, App. Phys. Lett. **79**, 1590 (2001).

[33] C. Gmachl, H. M. Ng, S.-N. G. Chu, and A. Y. Cho, App. Phys. Lett. **77**, 3722 (2000).

[34] R. Akimoto, K. Akita, F. Sasaki, and T. Hasama, Appl. Phys. Lett. **81**, 2998 (2002).

[35] R. Akimoto, K. Akita, F. Sasaki, and S. Kobayashi, Appl. Phys. Lett. **80**, 2433 (2002).

[36] R. Akimoto, Y. Kinpara, K. Akita, F. Sasaki, and S. Kobayashi, Appl. Phys. Lett. **78**, 580 (2001).

[37] M. Göppert, M. Grün, C. Maier, S. Petillon, R. Becker, A. Dinger, A. Storzum, M. Jörger, and C. Klingshirn, Phys. Rev. B **65**, 115334 (2002).

[38] G. Bastard and J. A. Brum, IEEE J. Quantum Electron. QE-**22**, 1625 (1986); G. Bastard, *Wave Mechanics applied to Semiconductor Heterostructures*, (Les editions de Physique, France, 1988); G. Bastard, J. A. Brum and R. Ferreira, *Solid State Physics,* vol. 44, pp. 229, edited by H. Ehrenreich and D. Turnbull (Academic, New York, 1991).

[39] M. BURT, J. Phys. Condens. Matter **11,** R53 (1999).

[40] G. Bastard, Phys. Rev. B **24**, 5693 (1981).

[41] S. White and L. J. Sham, Phys. Rev. Lett. **47**, 879 (1981).

[42] M. F. H. Schuurmans and G. W.'t Hooft, Phys. Rev. B **31**, 8041 (1985).

[43] Y.-C. Chang and J. N. Schulman, J. Vac. Sci. Technol. **21**, 540 (1982).

[44] J. N. Schulman and Y.-C. Chang, Phys. Rev. B **31**, 2056 (1985).

[45] D. J. Ben Daniel and C. B. Duke, Phys. Rev. **152**, 683 (1966).

[46] E. O. Kane, J. Phys. Chem. Solids **1**, 249 (1957); E. O. Kane, *Semiconductors and Semimetals,* vol. 1, pp. 75 (Academic, New York, 1975).

[47] W. A. Harrison, *Electronic Structure and Properties of Solids* (Freeman, San Francisco, 1980), pp. 74-80; A. A. Levin, *Solid State Quantum Chemistry* (McGraw Hill, New York, 1977).

[48] W. Harrison, J. Vac. Sci. Technol. **14**, 1016 (1977); J. Vac. Sci. Technol. B **3**, 1231 (1985).

[49] W. A. Harrison and J. Tersoff, J. Vac. Sci. Technol. B **4**, 1068 (1986)

[50] See review by R. Bauer and G. Margaritondo, Phys. Today **41**, No. 1, 26 (1987).

[51] F. H. Pollak and H. Shen, Mater. Sci. Eng. R. **10**, 275 (1993).

[52] M. Cardona, *Modulation Spectroscopy* (Academic, New York, 1969).

[53] F. H. Pollak, in *Group III Nitride Semiconductor Compounds*, edited by B. Gil (Clarendon, Oxford, 1998) pp. 158.

[54] O. J. Glembocki and B. V. Shanabrook, in *Semiconductors and Semimetals*, edited by R. K. Willardson and A. C. Beer (Academic, New York, 1992) Vol. 36,

pp. 221.

[55] T. Holden, P. Ram, F. H. Pollak, J. L. Freeouf, B. X. Yang, and M. C. Tamargo, Phys. Rev. B **56**, 4037 (1997).

[56] K. L. Teo, Y. P. Feng, M. F. Li, T. C. Chong and J. B. Xia: Semicond. Sci. Technol. **9**, 349 (1994).

[57] *Semiconductors—BasicData*, 2nd ed., edited by O. Madelung (Springer, Berlin, 1996).

[58] P. Lawaetz, Phys. Rev. B **4**, 3460 (1971).

[59] F. H. Pollak, "Effects of Uniaxial Stress on the Optical Properties of Semiconductors and Semiconductor Microstructures", in *Semiconductors and Semimetals*, edited by R. K. Willardson and A. C. Beer (Academic Press, San Diego, 1998) Vol. 55, Chapter 4.

[60] *Numerical Data and Functional Relationships in Science and Technology*, Landolt-Börnstein edited by O. Madelung, M. Schultz, and H. Weiss, (Springer, New York, 1982), Vol. III/11.

[61] A. Blacha, H. Presting, and M. Cardona, Phys. Stat. Sol. (b) **126**, 11 (1984).

[62] B. F. Levine, J. Appl. Phys. **74**, R1 (1993).

[63] M. Muñoz, H. Lu, X. Zhou, M. C. Tamargo, and F. Pollak, Appl. Phys. Lett. **83**, 1995 (2003).

[64] M. Sohel, X. Zhou, H. Lu, N. Perez-Paz, M. Muñoz, M. C. Tamargo, J. Vac. Sci. Technol. B **23** 1209 (2005).

[65] G. Bastard and J. A. Brum, IEEE J. Quantum Electron. QE-**22**, 1625 (1986).

[66] G. Bastard, Wave Mechanics applied to Semiconductor Heterostructures, Les editions de Physique, France 1988.

[67] R. Kersting, R. Schwedler, K. Wolter, K. Leo, and H. Kurz, Phys. Rev. B **46**, 1639 (1992).

[68] B. K. Ridley, Phys. Rev. B **41**, 12190 (1990).

[69] J. Dekker, M. Dumitrescu, A. Tukiainen, S. Orsila, P. Uusimaa, M. Pessa, N. V. Tkachenko, and H. Lemmetyinen, J. Appl. Phys. **92**, 173 (2002).

[70] R. Cingolani, L. Calcagnile, G. Coli, R. Rinaldi, M. Lomoscolo, M. DiDio, A. Franciosi, L. Vanzetti and G. C. LaRocca, J. Opt. Soc. Am. B **13**, 1268 (1996).

[71] C. Jordan, J. F. Donegan, J. Hegarty, B. J. Roycroft, S. Taniguchi, T. Hino, E. Kato, N. Noguchi, and A. Ishibashi, Appl. Phys. Lett. **74**, 3359 (1999).

[72] A. Hangleiter, Phys. Rev. B **48**, 9146 (1993).

[73] T. Takagahara and E. Hanamura, Phys. Rev. Lett. **56**, 2533 (1986).

[74] J. Feldmann, G. Peter, E. O. Göbel, P. Dawson, K. Moore, C. Foxon, and R. J. Elliott, Phys. Rev. Lett. **59**, 2337 (1987).

[75] G. W. ‘t Hooft, M. R. Leys and H. J. Talen-v.d. Mheen, Superlattices and Microstructures 1, 307 (1985).

[76] V. P. Varshni, Phys. Stat. Sol. **19**, 459 (1967).

[77] V. P. Varshni, Phys. Stat. Sol. **20**, 9 (1967).

[78] P. Michler, A. Hangleiter, M. Moser, M. Geiger and F. Scholz, Phys. Rev. B **46**, 7280 (1992).

[79] M. Vening, D. J. Dunstan and K. P. Homewood, Phys. Rev. B **48**, 2412 (1993).

[80] D. V. Lang and C. H. Henry, Phys. Rev. Lett. **35**, 1525 (1975).

[81] G. K. Wertheim, Phys. Rev. **109**, 1086 (1958).

[82] H. Sunamura, Y. Shiraki and S. Fukatsu, Appl. Phys. Lett. **66**, 953 (1994).

[83] J. Li, K. B. Nam, J. Y. Lin and H. X. Jiang, Appl. Phys. Lett. **79**, 3245 (2001).

[84] O. Maksinov, S. P. Guo, M. Muñoz and M. C. Tamargo, J. Appl. Phys. **90**, 5135 (2001).

[85] P. Michler, T. Forner, V. Hofsä, F. Prins, K. Zieger, F. Scholz and A. Hangleiter, Phys. Rev. B **49**, 16632 (1994).

[86] E. A. Vinogradov, B. N. Mavrin, and L. K. Vodop'yanov, JETP **99**, 749 (2004).

[87] N N Melnik, Yu G Sadofyev, T N Zavaritskaya and L K Vodop'yanov, Nanotechnology **11**, 252 (2000).

[88] M. Muñoz , H. Lu, X. Zhou, M. C. Tamargo, and F. H. Pollak, Appl. Phys. Lett. 83, 1995 (2003).

[89] M. Sohel, X. Zhou, H. Lu, M. N. Perez-Paz, M. Tamargo and M. Muñoz, J. Vac. Sci. Technol. B **23(3)**, 1209 (2005).

[90] B. F. Levine, J. Appl. Phys. **74**, R1 (1993).

[91] C. Gmachl, F. Capasso, D. L. Sivco, and A. Y. Cho, Rep. Prog. Phys. **64**, 1533 (2001).

[92] H. Lu, A. Shen, S. Y. Song, H. C. Liu, S. K. Zhang, R. R. Alfano, M. C. Tamargo, and M. Muñoz, Appl. Phys. Lett. **89**, 131903 (2006).

[93] F. H. Pollak and H. Shen, Mater. Sci. Eng. R. **10**, 275 (1993).

[94] O. J. Glembocki and B. V. Shanabrook, in Semiconductors and Semimetals, edited by R. K. Willardson and A. C. Beer, Academic, New York, Vol. 36, p. 221 (1992).

[95] P. A. Dafesh, J. Appl. Phys. **71**, 5154 (1992).

[96] G. Sęk, J. Misiewicz, K. Regi´nski, and J. Muszalski, Vacuum **48**, 283 (1997).

[97] Y. S. Huang and F. H. Pollak, Phys. Stat. Sol. (a) **202**, 1193 (2005).

[98] P. A. Dafesh, J. Appl. Phys. **71**, 5154 (1992).

[99] F. H. Pollak, Group III Nitride Semiconductor Compounds. Clarendon, Oxford, 1998.

[100] T. Holden, P. Ram, F. H. Pollak, J. L. Freeouf, B. X. Yang, and M. C. Tamargo, Phys. Rev. B **56**, 4037 (1997).

[101] G. Bastard and J. A. Brum, IEEE J. Quantum Electron. QE-**22**, 1625 (1986).

[102] G. Bastard, Wave Mechanics applied to Semiconductor Heterostructures. Les Editions de Physique, Paris France, 1988.

[103] H. Lu, A. Shen, M. Muñoz, M. N. Perez-Paz, M. Sohel, S. K. Zhang, R. R. Alfano, and M. C. Tamargo, Phys. Stat. Sol. (b) **243**, 868 (2006).

[104] M. Muñoz, H. Lu, X. Zhou, M. C. Tamargo, and F. H. Pollak, Appl. Phys. Lett. **83**, 1995 (2003).

[105] L. C. West and S. J. Eglash, Appl. Phys. Lett. **46**, 1156 (1985).

[106] B. F. Levine, R. J. Malik, J. Walker, K. K. Choi, C. G. Bethea, D. A. Kleinman, and J. M. Vandenberg, Appl. Phys. Lett. **50**, 273 (1987).

[107] J. Y. Andersson and G. Landgren, J. Appl. Phys. **64**, 4123 (1988).

[108] M. J. Kane, M. T. Emeny, N. Apsley, C. R. Whitehouse, and D. Lee, Semicond, Sci. Technol. **2**, 722 (1988).

[109] M. J. Kane, M. T. Emeny, N. Apsley, and C. R. Whitehouse, Electron. Lett. **25**, 230 (1989).

[110] Intersubband Transitions in Quantum Wells: Physics and Device Applications I & II, Semiconductors and Semimetals, edited by H.C. Liu and F. Capasso (Academic, San Diego, 2000). Vols. 62 and 66.

[111] P. von Allmen, M. Berz, F. K. Reinhart, and G. Harbeke, Superlattices and Microstructures **5**, 259 (1989).

[112] B. C. Covington, C. C. Lee, B. H. Hu, H. F. Taylor, and D. C. Streit, Appl. Phys. Lett. **54**, 2145 (1989).

[113] G. Hasnain, B. F. Levine, C. G. Bethea, R. R. Abbott, and S. J. Hsieh, J. Appl.

Phys. **67**, 4361 (1990).